INFORMATION TO USERS

This manuscript has been reproduced from the microfilm master. UMI films the text directly from the original or copy submitted. Thus, some thesis and dissertation copies are in typewriter face, while others may be from any type of computer printer.

The quality of this reproduction is dependent upon the quality of the copy submitted. Broken or indistinct print, colored or poor quality illustrations and photographs, print bleedthrough, substandard margins, and improper alignment can adversely affect reproduction.

In the unlikely event that the author did not send UMI a complete manuscript and there are missing pages, these will be noted. Also, if unauthorized copyright material had to be removed, a note will indicate the deletion.

Oversize materials (e.g., maps, drawings, charts) are reproduced by sectioning the original, beginning at the upper left-hand corner and continuing from left to right in equal sections with small overlaps.

Photographs included in the original manuscript have been reproduced xerographically in this copy. Higher quality 6" x 9" black and white photographic prints are available for any photographs or illustrations appearing in this copy for an additional charge. Contact UMI directly to order.

ProQuest Information and Learning
300 North Zeeb Road, Ann Arbor, MI 48106-1346 USA
800-521-0600

UMI®

Reproduced with permission of the copyright owner. Further reproduction prohibited without permission.

DISSERTATION

COMPARING THE ROLES OF INDUCTIVE AND CAPACITIVE COUPLING IN A PLANAR INDUCTIVELY COUPLED PLASMA THROUGH BOTH THEORY AND EXPERIMENT

Submitted by

Masahiro Watanabe

Department of Electrical and Computer Engineering

In partial fulfillment of the requirements

For the Degree of Doctor of Philosophy

Colorado State University

Fort Collins, Colorado

Spring 2001

Reproduced with permission of the copyright owner. Further reproduction prohibited without permission.

UMI Number: 3013872

UMI®

UMI Microform 3013872

Copyright 2001 by Bell & Howell Information and Learning Company.
All rights reserved. This microform edition is protected against
unauthorized copying under Title 17, United States Code.

Bell & Howell Information and Learning Company
300 North Zeeb Road
P.O. Box 1346
Ann Arbor, MI 48106-1346

Reproduced with permission of the copyright owner. Further reproduction prohibited without permission.

COLORADO STATE UNIVERSITY

April 10, 2001

WE HEREBY RECOMMEND THAT THE DISSERTATION PREPARED UNDER OUR SUPERVISION BY MASAHIRO WATANABE ENTITLED COMPARING THE ROLES OF INDUCTIVE AND CAPACITIVE COUPLING IN A PLANAR INDUCTIVELY COUPLED PLASMA THROUGH BOTH THEORY AND EXPERIMENT BE ACCEPTED AS FULFILLING IN PART REQUIREMENTS FOR THE DEGREE OF DOCTOR OF PHILOSOPHY.

Committee on Graduate Work

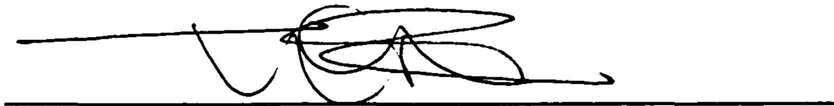

Advisor

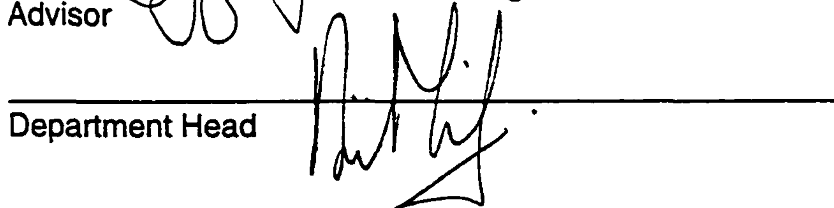

Department Head

Reproduced with permission of the copyright owner. Further reproduction prohibited without permission.

ABSTRACT OF DISSERTATION

COMPARING THE ROLES OF INDUCTIVE AND CAPACITIVE COUPLING IN A PLANAR INDUCTIVELY COUPLED PLASMA THROUGH BOTH THEORY AND EXPERIMENT

The inductive and capacitive excitation coil-plasma interaction in an inductively coupled plasma (ICP) is studied in this dissertation. The inductive coupling transfers power from the excitation coil to the plasma, while the parasitic capacitive coupling gives rise to rf plasma potential and DC self bias on the dielectric window, which causes unwanted dielectric window sputtering. A combined inductive/capacitive model was developed in order to quantify this problem.

Prior to this work, Piejak et al. developed an air core transformer model to describe the power transfer mechanism from the excitation coil to the plasma through an inductive coupling mechanism, in which the plasma is considered the secondary circuit of an air core transformer. The plasma secondary circuit is coupled to the primary circuit through a magnetic coupling coefficient k. The inductive coupling model concludes that the power consumed in the plasma is proportional to k^2 for a given rf current applied to the excitation coil. This is verified experimentally herein to determine the effectiveness of the inductive coupling model.

Reproduced with permission of the copyright owner. Further reproduction prohibited without permission.

The high rf voltage applied to drive the excitation coil creates a parasitic capacitive current pathway through the dielectric window and rf sheath to the plasma. A voltage divider circuit model is developed herein to understand the capacitive coupling from the excitation coil to the plasma, where the dielectric window and the rf sheath are considered as series capacitances. The capacitive coupling model is experimentally verified from measurements of the rf plasma potential.

From both inductive and capacitive coupling models, it is shown that the rf plasma potential is indirectly influenced by inductive coupling as well as directly by capacitive coupling. Finally, a combined inductive/capacitive model is developed in order to describe fully the combined effects of the two coupling mechanisms from the excitation coil to the plasma. The combined model gives a simple relationship between the coupling and the resulting rf plasma potential variation. This combined model enables one to understand the excitation coil-plasma interaction and characterize the electrical parameters in the plasma system.

Masahiro Watanabe
Department of Electrical and Computer Engineering
Colorado State University
Fort Collins, CO 80523
Spring 2001

Reproduced with permission of the copyright owner. Further reproduction prohibited without permission.

Acknowledgments

The author wishes to take note the many people who supported him during his education, both directly and indirectly.

I would like to thank Denis M. Shaw for giving me valuable advice and help on my research. I would also thank Hiroshige Uchiyama for his assistance and useful discussions. In addition, I would like to thank the ERC office staff for assisting me over the duration of my studies at CSU.

I am grateful to my advisor, Dr. George J. Collins, for his valuable suggestions.

Finally, I would like to thank my family for their useful advice and support. I would like to especially thank my mother and father for teaching me to be independent.

Reproduced with permission of the copyright owner. Further reproduction prohibited without permission.

Table of Contents

ABSTRACT iii
ACKNOWLEDGMENTS v
TABLE OF CONTENTS vi
LIST OF FIGURES viii

CHAPTER 1 INTRODUCTION 1

1.1 Background 1
1.2 Research Approach 5
1.3 Outline of Dissertation 7
Chapter 1 References 8

CHAPTER 2 EXPERIMENTAL SETUP 10

2.1 Inductively Coupled Plasma Source 10
2.2 Measurement Tools 16
2.2.1 Langmuir probe 17
2.2.2 B-dot probe 22
2.2.3 Capacitive plasma potential probe 23
Chapter 2 References 27

CHAPTER 3 INDUCTIVE COUPLING IN ICP 28

3.1 Theoretical Description – Air Core Transformer Model 28
3.2 Experiment and Discussion 37
3.2.1 Magnetic coupling coefficient k 38
3.2.2 rf input impedance: Z_{in} 43
Chapter 3 References 50

Reproduced with permission of the copyright owner. Further reproduction prohibited without permission.

CHAPTER 4 CAPACITIVE COUPLING IN ICP 51

4.1 Theoretical Description of the ICP, Including Capacitive Coupling 51
4.1.1 rf sheath theory 52
4.1.2 Capacitive voltage divider circuit model 61
4.1.3 Dielectric window sputtering caused by capacitive coupling 71
4.2 Experimental Results and Discussion 78
4.2.1 Equipotential verification by rf plasma potential measurement 78
4.2.2 Measurement of dielectric window capacitance 79
4.2.3 Measurement of the rf voltage distribution along excitation coil 80
4.2.4 Capacitive probe and RPA methods 82
(a) Retarding potential analyzer (RPA) 82
(b) Comparison of rf plasma potential 83
4.2.5 Measured rf plasma potential results 86
4.2.6 Trend of rf plasma potential 90
Chapter 4 References 93

CHAPTER 5 COMBINED MODEL INCLUDING INDUCTIVE AND CAPACITIVE COUPLING 94

5.1 Combined Model 94
5.2 Effect of Changing the Dielectric Window Thickness 96
5.2.1 Procedure 96
5.2.2 Measured and theoretical rf plasma potential 99
5.2.3 Discussion 107
Chapter 5 References 110

CHAPTER 6 SUMMARY AND FUTURE WORK 111

APPENDIX 114

Symbols and Physical Constants in the Dissertation 114

Reproduced with permission of the copyright owner. Further reproduction prohibited without permission.

List of Figures

Chapter 2

2.1 Schematic drawing of the experimental ICP source setup including the capacitive probe and the RPA.

2.2 Five variables, P_{gen}, P_{mn}, P_{del}, P_{coil}, and P_{abs} to represent various powers. There are Ohmic losses in the matching network and the excitation coil represented by P_{mn} and P_{coil}, respectively.

2.3 Three dielectric windows between the excitation coil and the plasma: (i) quartz window with d_w = 1.9 cm, (ii) quartz window with d_w = 2.2 cm, and (iii) quartz-air hybrid window with d_w = 2.5 cm. Note that quartz has ε_r = 4, μ_r = 1, and air has $\varepsilon_r = \mu_r = 1$.

2.4 Schematic drawing of Langmuir probe and its operation circuit. the ion and electron currents are collected by the probe tip. The probe voltage, V_B, is scanned using a DC voltage source, and the probe current is measured.

2.5 Typical Langmuir probe $I - V_B$ characteristic. Φ_p and Φ_f are the plasma potential and the floating potential, respectively.

2.6 Designs of Langmuir probe tip: (a) planar probe tip, (b) cylindrical probe tip with radius, a_t, and length, d_t. The probes are surrounded by dielectric tubes to eliminate noise coupling from the plasma.

2.7 $I - V_B$ characteristic measured by the cylindrical Langmuir probe, at ICP conditions of P_{del} = 250 W and p = 10 mTorr. Plasma electron density is calculated from the slope of the electron saturation current using Eq. (2.4).

2.8 Geometrical configuration of B-dot probe. Time varying magnetic flux is coupled to the one turn probe tip, and a voltage is induced according to Faraday's law. The probe voltage is measured by an oscilloscope.

2.9 Geometrical configuration of capacitive probe. The rf plasma potential is capacitively coupled to the probe. The probe voltage is measured by an oscilloscope.

2.10 Equivalent circuit of the capacitive probe. The rf plasma potential is capacitively coupled to the probe tip through the three series capacitances, representing the rf sheath, the glass sleeve and the space between the probe tip and the glass sleeve.

Chapter 3

3.1 ICP power transfer mechanism. Applied rf current into the spiral excitation coil creates a rf magnetic flux according to Ampere's law, which induces a rf electric field in the plasma region according to Faraday's law.

Reproduced with permission of the copyright owner. Further reproduction prohibited without permission.

3.2 Air core transformer model of ICP developed by Piejak et al. The plasma is treated as the secondary circuit of an air core transformer, which is coupled to the promary excitation coil by magnetic coupling coefficient k.
3.3 Torroidal plasma ring approximation. a_p is the plasma radius, and r_p is the ring radius.
3.4 Equivalent circuit of the air core transformer (inductive coupling) model. The secondary plasma circuit is transferred to the primary circuit (= $R_p' + jX_p'$). The coil impedance (= $R_{coil} + j\omega L_{coil}$) remains the same.
3.5 Schematic drawing of two coils, c_1 and c_2 to illustrate the magnetic coupling coefficient k between the two coils. k is defined by the portion of the magnetic flux ϕ_2 captured by c_2 when applying rf current I_1 to c_1.
3.6 Schematic drawing of the spatial integration of the local magnetic flux path for the three dielectric window thicknesses: (i) $d_w = 1.9$, (ii) $d_w = 2.2$, and (iii) $d_w = 2.5$, employed to calculate the magnetic flux fp induced in the plasma region by the rf coil current. Note that the scale in the drawing is not accurate.
3.7 Normalized relative magnetic coupling coefficient k_r for d_w = 1.9, 2.2, 2.5 cm measured by the B-dot probe. k_r monotonically decreases as d_w increases.
3.8 Measured plasma resistances transferred to the primary circuit R_p' versus absorbed plasma power P_{abs} for four argon pressures: (a) 1 mTorr, (b) 2 mTorr, (c) 5 mTorr, and (d) 20 mTorr. "exp." indicates the experimental values, and "theo." indicates the theoretical values for d_w = 2.2 and 2.5 cm.
3.9 Measured plasma reactance transferred to the primary circuit $|X_p'|$ versus absorbed plasma power P_{abs} for four argon pressures: (a) 1 mTorr, (b) 2 mTorr, (c) 5 mTorr, and (d) 20 mTorr. Note that the absolute values are shown in the figure. "exp." indicates the experimental values, and "theo." indicates the theoretical values for d_w = 2.2 and 2.5 cm.

Chapter 4

4.1 Structure of the rf sheath as modeled by Godyak et al. ni represents the spatial ion density and $\langle n_e \rangle$ represents the time-averaged electron density distribution in the rf sheath. rf displacement current flows through the sheath as the "electron sheath" edge s(t) moves.
4.2 Preliminary voltage divider circuit to model capacitive coupling from the excitation coil to the plasma body, where three series capacitances, C_w, C_{w-p}, and C_{p-g}, are employed.

Reproduced with permission of the copyright owner. Further reproduction prohibited without permission.

4.3 The spatially distributed capacitive coupling model: (a) basic model with the plasma fixed at an equipotential. Excitation coil, dielectric window and dielectric window-to-bulk plasma sheath capacitances are divided into "n" distributed parts, (b) Simplified circuit model used for the rf plasma potential calculation.

4.4 Theoretical rf plasma potential calculated using the capacitive coupling model for various integral numbers of lateral capacitors n. The calculated rf plasma potential is normalized to data for n = 1.

4.5 Dielectric window surface potential and current at pre-steady state conditions. (a) potential $\Phi_{ds}(t)$, (b) current I(t). Note that when Φ_{ds} is higher than the floating potential Φ_f, large amount of electron current I_e flows, while ion current I_i remains constant.

4.6 Dielectric window surface potential and current at steady state conditions. (a) potential $\Phi_{ds}(t)$, (b) current I(t). Note that the time-averaged potential $<\Phi_{ds}>$ becomes DC self bias Φ_{self}, where the time-averaged electron current $<I_e>$ is equal to I_i.

4.7 Radial spatial distribution of the measured rf plasma potential at two distances z below the dielectric window: z = 4.5 (circle) and 8 cm (triangle). The absorbed plasma power P_{abs} = 100 W, in p = 20 mTorr argon ambient. Note that the rf plasma potential is uniform at entire plasma region.

4.8 Schematic of the measurement technique of the dielectric window capacitance. The dielectric window is considered a capacitor with two electrodes (the excitation coil and the conducting sheet). The voltage measured between the two capacitances is used to calculate the dielectric window capacitance.

4.9 Normalized rf potential distribution measured along the excitation coil as a function of position along the coil length ℓ. The dotted line shows the linear impedance assumption along the excitation coil. The measured $V^*_{coilrf}(\ell)$ indicates non-linear impedance characteristic along the excitation coil.

4.10 Schematic drawing of the RPA. Ions and electrons are both incident into the RPA. Electrons are repelled by V_r = -40 V. V_d is scanned from 0 to 60 V to discriminate ions, and I_c is measured to obtain $I_c - V_d$ characteristics.

4.11 Normalized ion collector current I_c and first derivative versus discriminator voltage V_d as measured by the RPA for the ICP conditions of P_{del} = 125 W and p = 2 mTorr. ΔE is the energy spread of incident argon ions from the bulk plasma to the sheath.

4.12 rf plasma potential as measured separately by both the capacitive probe and the RPA, in 2 mTorr argon. These two independent results are in good agreement.

Reproduced with permission of the copyright owner. Further reproduction prohibited without permission.

4.13 Both measured and calculated rf plasma potential as a function of P_{abs} in the argon pressures of (a) 1, (b) 2, (c) 5, and (d) 20 mTorr. The measured and calculated results are in good agreement.

Chapter 5

5.1 Schematic drawing of the combined inductive/capacitive coupling model. The plasma is coupled to the excitation coil both through the magnetic coupling coefficient k (inductive coupling) and through the three series capacitances (capacitive coupling).

5.2 The measured relative magnetic coupling coefficient k_r and dielectric window capacitance C^*_w normalized to the data for d_w = 1.9 cm (k_r(1.9) = C^*_w(1.9) = 1). Note that k_r(2.2) is close to C^*_w(2.2), while C^*_w(2.5) is smaller than k_r(2.5).

5.3 Theoretical rf plasma potential calculated using the combined inductive/capacitive coupling model for three dielectric window thicknesses d_w = 1.9, 2.2, 2.5 cm in argon pressures of : (a) 1, (b) 2, (c) 5, and (d) 20 mTorr.

5.4 The rf coil voltage measured at the excitation coil input for three dielectric window thicknesses d_w = 1.9, 2.2, 2.5 cm in argon pressures of : (a) 1, (b) 2, (c) 5, and (d) 20 mTorr. Note that V_{coilrf} increases as d_w increases.

5.5 The measured rf plasma potential for three dielectric window thicknesses d_w = 1.9, 2.2, 2.5 cm in argon pressures of : (a) 1, (b) 2, (c) 5, and (d) 20 mTorr. Note that the data for d_w = 1.9 and 2.2 cm are close together, while the data for d_w = 2.5 cm is distinguishably smaller.

Reproduced with permission of the copyright owner. Further reproduction prohibited without permission.

CHAPTER 1 INTRODUCTION

1.1 Background

For integrated circuit (IC) manufacturing, one of the key capabilities is to scale down the physical size of a MOSFET to achieve a higher number density of transistors on an IC chip. This spatial miniaturization results in both lower power consumption and faster operation of the integrated circuit.[1] Presently, IC designers successfully employ 0.15 micron feature-size transistors. It is expected that in near future the transistor size will go down to less than 0.08 micron.[2,3] To satisfy this future requirement, process technology such as etching and photolithography must be further developed beyond their current capabilities.

Historically, wet etching of transistor features was replaced by dry etch processes using Capacitively Coupled Plasmas (CCP).[4-11] This was done because of plasma's unique capability of anisotropic etching (directional etching), where directional ion flux to the etching surface helps to obtain "ideal" vertical sidewall profile in the etch feature. Wet etching was isotropic in its etch profiles and could not be used below 1 micron feature size. The capability of vertical sidewall profiles etching offered by CCP allowed the manufacture of micron-size transistors for the first time. However, as the feature size is decreased below 0.25 micron, the demand for anisotropic ion motion in a CCP becomes

Reproduced with permission of the copyright owner. Further reproduction prohibited without permission.

problematic. The relatively high operating pressure (p ~ 100 mTorr) in a CCP causes many ion-neutral collisions within a plasma sheath, which decreases the directionality of incident ion flux towards the etch feature. Therefore, stable plasma operation in low pressure (p ~ 1 – 20 mTorr) is desired, where ion-neutral collision mean free paths are long compared to the sheath width. Furthermore, a high etch rate is economically desirable for both higher wafer throughput and a lower manufacturing cost. To satisfy these two requirements for the next generation of IC manufacturing, newer plasma sources, which are able to generate a higher plasma density at a lower operating pressure, have been developed.

Inductively Coupled Plasmas (ICP) are one of the advanced plasma sources satisfying the above requirements.[12-24] An advantage in the ICP compared to the other advanced plasma sources such as Electron Cycrotron Resonance (ECR) Plasmas[25,26] and Surface Wave Plasmas (SWP)[27-29] is its simplicity of design. To generate an ICP, rf current (typically 13.56 MHz) is applied through an external excitation coil wound around a dielectric vacuum chamber. A rf magnetic flux is produced following Ampere's law, which passes through the dielectric walls in the plasma chamber. The time-varying rf magnetic flux density, $\dot{B}$, induces a rf electric field according to Faraday's law. This electric field accelerates plasma electrons and sustains the plasma. A stove top type configuration of the coil carrying the rf current, which sits on the dielectric plate separating the chamber region from atmosphere, is widely used.

Reproduced with permission of the copyright owner. Further reproduction prohibited without permission.

It is attractive because of its capability for achieving a higher plasma uniformity in the entire plasma chamber. Cylindrical excitation coils around the chamber are also employed. In both cases, the rf power transfer mechanism is crudely analogous to an electrical current in the primary circuit of an air core transformer magnetically inducing an electrical current in the secondary circuit.[15,16]

Piejak et al. first proposed the inductive power transfer mechanism from the excitation coil to the plasma using a simple air core transformer model.[16] In their inductive coupling model, the plasma is treated as an inductive load representing the secondary circuit of a transformer, which is coupled to the primary circuit of the transformer by the magnetic coupling coefficient k. This coefficient takes into account the portion of the total magnetic flux provided by the excitation coil coupled to the plasma. However, the treatment of the plasma as simply a secondary circuit of an air core transformer might cause significant error because the plasma is not a simple load having a fixed electrical impedance. The plasma impedance might have non-linear characteristics due to its complicated nature. Furthermore, the non-linearity of the plasma load might vary as the plasma condition changes. Therefore, the experimental verification of the inductive coupling model is desired over a wide range of plasma conditions.

To drive a high density plasma, a considerable amount of rf current (~ 10 A) is required through the excitation coil. To obtain such a large rf current through the coil, several kV of rf voltage is applied to the coil input. Placing a 1

Reproduced with permission of the copyright owner. Further reproduction prohibited without permission.

– 10 kV rf potential on the coil causes parasitic capacitive coupling through the dielectric window from the coil to the plasma.[13,18-21,24] This is in addition to the inductive coupling. The rf electric field perpendicular to the dielectric window plane, which is created by the capacitive coupling, is of practical importance because it makes start-up ignition of the ICP source easier. That is, the capacitive coupling is dominant during plasma ignition and then plays a smaller role once the inductive coupling is achieved.

The capacitive coupling creates a second power transfer pathway from the excitation coil to the plasma. This capacitive power transfer was entirely neglected in the prior-art inductive coupling model developed by Piejak et al.[16] Experimentally, it is well known that the capacitive coupling causes a mode jump in the plasma density due to the change in power transfer mechanism from the capacitive-coupling dominant at low plasma density to inductive-coupling dominant at high plasma density.[18] DC self bias on the dielectric window due to the capacitive coupling also causes unwanted dielectric window sputtering.[19,20] The resulting sputtered material contaminates the plasma and the substrate to be etched.[22,23] Furthermore, erosion of the dielectric requires frequent and costly window replacement. To better understand these problems, the parasitic capacitive coupling from the excitation coil to the plasma must be studied.

Capacitive power transfer in an ICP has been investigated previously by Suzuki et al.[18] This work focused on the density mode jump caused by the change in the power transfer mechanism from capacitive-dominant to inductive-

Reproduced with permission of the copyright owner. Further reproduction prohibited without permission.

dominant. This dissertation has a different goal which is to understand the rf plasma potential fluctuation, V_{prf} (V), caused by the capacitive coupling, where the plasma potential, Φ_p (V), is the potential of the plasma with respect to the grounded chamber wall having both DC and rf components.[24]

1.2 Research Approach

As previously noted, a simplified power transfer mechanism in an ICP has already been described using the air core transformer model (inductive coupling model) by Piejak et al.[16] However, the inductive coupling model treats the ICP as a simple air core transformer circuit.

Herein, we first experimentally measure the plasma characteristics and relate the measured results to the inductive coupling model. We then verify the effectiveness of the inductive coupling model by measuring the input impedance of the excitation coil, including the plasma load, Z_{in} (Ω). This impedance is measured over varying plasma parameters such as absorbed plasma power, P_{abs} (W), ambient gas pressure p (Torr), and the distance between the coil and the plasma as set by a dielectric window with thickness, d_w (m). Changing d_w changes Z_{in}, as described in the inductive coupling model.

We next develop a new capacitive voltage divider circuit model (capacitive coupling model) to explain the parasitic capacitive coupling from the excitation coil to the plasma in an ICP system.[24] In the capacitive coupling model, the capacitive current pathway from the high potential coil to the plasma

Reproduced with permission of the copyright owner. Further reproduction prohibited without permission.

is considered as a combination of capacitors in series. The plasma resistance is neglected in the capacitive coupling model, since a high electron density plasma may be dealt with as a short circuit.[13] The capacitive coupling model is solved for the rf plasma potential, V_{prf}. Understanding the rf plasma potential variations is crucial to better understand and control the unwanted dielectric window sputtering.

The measured rf plasma potential is compared to the rf plasma potential calculated from the new capacitive coupling model. Two tools are employed to measure the rf plasma potential, a capacitive probe and a Retarding Potential Analyzer. Good agreement between the two measured results indicates that the capacitive probe is an accurate tool to measure the rf plasma potential. Good agreement between values of V_{prf} calculated from the capacitive coupling model and these measured suggests the validity of the capacitive coupling model.

From the new capacitive coupling model, one can better understand how the capacitive coupling is influenced by the inductive coupling. We purposely change both the inductive coupling and the capacitive coupling by changing the thickness of the dielectric window separating the excitation coil from the plasma. From the combined model of inductive and capacitive coupling, we study the quantitative interaction between the inductive and the capacitive coupling. This approach enables us to optimize the overall electrical characteristics of the ICP

Reproduced with permission of the copyright owner. Further reproduction prohibited without permission.

system through optimized inductive and capacitive coupling from the excitation coil to the plasma.

To summarize, this dissertation focuses on the interaction between inductive and capacitive coupling in ICP system and develops new theoretical models to account for the two coupling mechanisms. Furthermore, we experimentally prove the validity of the models. This work helps to better understand the inductive coupling and parasitic capacitive coupling mechanisms and to characterize electric parameters in an ICP system.

1.3 Outline of Dissertation

Chapter 2 describes the experimental setup and measurement tools used in our research. Chapter 3 discusses the inductive coupling in ICP designs. The air core transformer model (inductive coupling model) is introduced and verified through our experimental data on the input impedance of the excitation coil including the plasma load. Chapter 4 describes the capacitive coupling encountered in ICP designs. We develop the capacitive voltage divider circuit model (capacitive coupling model), and verify it through experiments. In chapter 5, the new combined model of inductive coupling and capacitive coupling is discussed. In chapter 6, this research is summarized and future work is suggested.

Reproduced with permission of the copyright owner. Further reproduction prohibited without permission.

Chapter 1 References

1. N. H. E. Weste, and K. Eshraghian, "Principles of CMOS VLSI Design," Addison Wesley (1994).
2. N. Layadi, J. I. Colonell, and J. T. Lee, Bell Labs Technical J. 155 (1999).
3. M. Armacost, P. D. Hoh, R. Wise, W. Yan, J. J. Brown, J. H. Keller, G. A. Kaplita, S. D. Halle, K. P. Muller, M. D. Naeem, S. Srinivasan, H. Y. Ng, M. Gutsche, A. Gutmann, and B. Spuler, IBM J. Res. Develop. **43**, 39 (1999).
4. C. J. Mogab, A. C. Adams, and D. L. Flamm, J. Appl. Phys. **49**, 3796 (1978).
5. J. W. Coborn, J. Appl. Phys. **50**, 5210 (1979).
6. D. L. Flamm, and V. M. Donnelly, Plasma Chem. Plasma Processing **1**, 317 (1981).
7. L. M. Ephrath, and E. J. Petrillo, J. Electrochem. Soc.: Solid-State Science and Technol., **129**, 2282 (1982).
8. A. J. van Roosmalen, W. G. M. van den Hoek, and H. Kalter, J. Appl. Phys. **58**, 653 (1985).
9. I. C. Plumb, and K. R. Ryan, Plasma Chem. Plasma Process. **6**, 205 (1986).
10. D. M. Manos, and D. L. Flamm, eds. (1989), Plasma Etching: An Introduction, Academic, New York.
11. V. A. Godyak, R. B. Piejak, and B. M. Alexandrovich, IEEE Trans. Plasma Sci. **19**, 660 (1991).
12. J. H. Keller, J. C. Forster, and M. S. Barnes, J. Vac. Sci. Technol. A **11**, 2487 (1993).
13. M. A. Lieberman, and A. J. Lichtenberg, "Principles of Plasma Discharges and Material Processing," John Wiley and Sons, New York (1994).
14. Y. Hikosaka, M. Nakamura, and H. Sugai, Jpn. J. Appl. Phys. Part1, **33**, 2157 (1994).
15. J. Hopwood, Plasma Sources Sci. Technol. **1**, 109 (1992).
16. R. B. Piejak, V. A. Godyak, and B. M. Alexandrovich, Plasma Sources Sci. Technol. **1**, 179 (1992).
17. H. Sugai, K. Nakamura, Y. Hikosaka, and M. Nalamura, J. Vac. Sci. Technol. A **13**, 887 (1995).
18. K. Suzuki, K. Nakamura, H. Ohkubo, and H. Sugai, Plasma Sources Sci. Technol. **7**, 13 (1998).
19. H. Sugai, K. Nakamura, and K. Suzuki, Jpn. J. Appl. Phys. Part1 **33**, 2189 (1994).
20. M. Schaepkens, N. R. Rueger, J. J. Beulens, X. Li, T. E. F. M. Standaert, P. J. Matsuo, and G. S. Oehrlein, J. Vac. Sci. Technol. A, **17**, 3272 (1999).

Reproduced with permission of the copyright owner. Further reproduction prohibited without permission.

21. T. Lho, N. Hershkowitz, G. H. Kim, W. Steer, and J. Miller, Plasma Sources Sci. Technol. **9**, 5 (2000).
22. Y. Hikosaka, M. Nakamura, and H. Sugai, Proc. 15th Symp. Dry Process, 97 (Tokyo, 1993).
23. Y. Horiike, Ext. Abstr. 4th Int. Symp. ULSI Science and Technology, 991 (Honolulu, 1993).
24. M. Watanabe, D. M. Shaw, G. J. Collins, and H. Sugai, J. Appl. Phys. **85**, 3428 (1999).
25. S. Samukawa, Jpn. J. Appl. Phys. **29**, 980 (1990).
26. S. Samukawa, Jpn. J. Appl. Phys. **33**, 2133 (1994).
27. T. Akimoto, E. Ikawa, T. Sango, K. Komachi, K. Katayama, and T. Ebata, Jpn. J. Appl. Phys. Part1, **33**, 7037 (1994).
28. H. Sugai, I. Ghanashev, and M. Nagatsu, Plasma Sources Sci. Technol. **7**, 192 (1998).
29. H. Kokura, S. Yoneda, K. Nakamura, N. Mitsuhira, M. Nakamura, and H. Sugai, Jpn. J. Appl. Phys. **38**, 5256 (1999).

Reproduced with permission of the copyright owner. Further reproduction prohibited without permission.

CHAPTER 2 EXPERIMENTAL SETUP

Herein, the experimental ICP source is described, the definition of rf power flow from the power supply to the plasma is presented (section 2.1), and the various measurement tools employed are discussed (section 2.2). The experimental data collected in the ICP source are compared to various theories, including the theory developed in this work.

2.1 Inductively Coupled Plasma Source

A schematic of the ICP source used in our experiment is shown in Fig. 2.1.[1] The plasma is excited in a well-grounded aluminum chamber 25 cm in diameter and 12 cm high. A turbomolecular pump is placed under the plasma chamber to obtain 2×10^{-6} Torr base minimum pressure. A 20 cm diameter, 4 turn copper spiral coil is placed on top of a dielectric window for the plasma excitation. The dielectric window is typically 1.9 cm thick. However, as discussed in Chapter 3 and 5, the thickness of the dielectric window is varied to 2.2 cm and 2.5 cm. The center of the excitation coil is connected to a rf power supply (driving frequency, f_{rf} = 13.56 MHz) through a "L" type matching network to achieve 50 Ω matching, and the other end is connected to the grounded plasma chamber. A rf current applied to the coil induces a rf electric field in the

Reproduced with permission of the copyright owner. Further reproduction prohibited without permission.

plasma chamber, which drives the plasma electron current. In our experiments, the plasma is sustained by rf power (62.5 W to 1000 W) from the power supply over the argon pressure range between 1 mTorr and 20 mTorr.

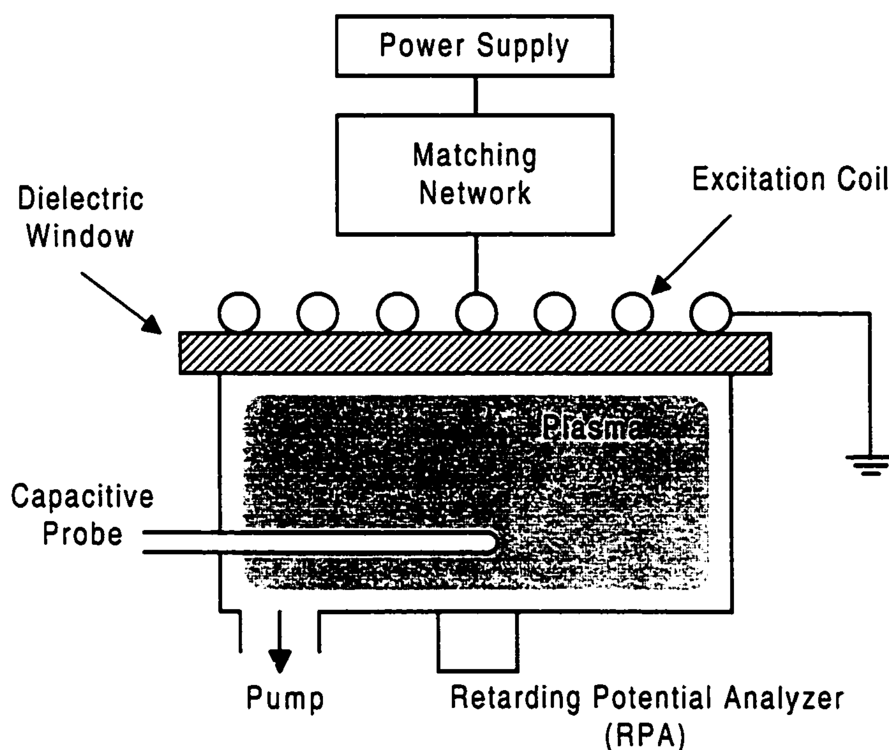

Figure 2.1 Schematic drawing of the experimental ICP source setup including the capacitive probe and the RPA.

Reproduced with permission of the copyright owner. Further reproduction prohibited without permission.

The rf coil impedance (Z_{coil} = 0.08 + j87.2 Ω) and the total rf input impedance of the coil including the ICP circuit (i.e. with plasma), $Z_{in} = R_{in} + jX_{in}$ [Ω], are measured at the coil input using a rf plasma impedance monitor (Advanced Energy Z-Scan). The accuracy of the impedance probe has been independently determined.[2] The rf impedance probe also measures rf voltage at the coil input, V_{coilrf} [V], rf current through the excitation coil, I_{coilrf} [A], and the rf power delivered to the plasma, P_{del} [W]. The measurement errors for V_{coilrf} and I_{coilrf} are determined to be within 3 % of actual values and the measurement error for P_{del} is within 10 % of actual values over the range of parameters in this work.[2] The measured Z_{in} and Z_{coil} are primarily used for the verification of the inductive coupling model developed by Piejak et al.[3] The measured V_{coilrf} is used for the calculation of the rf plasma potential in the capacitive coupling model. The measured P_{del} and I_{coilrf} are primarily used for the calculation of absorbed plasma power, P_{abs} [W], described below.

Since there are power losses in the matching network and the excitation coil, five variables, P_{gen}, P_{mn}, P_{del}, P_{coil} and P_{abs} [W], are used to represent the powers as shown in Fig. 2.2. P_{gen} represents the power generated at the rf power supply and applied to the matching network. P_{gen} is monitored by the rf power supply. P_{del} is the power delivered to the excitation coil as monitored by the impedance probe. P_{mn} is the power loss in the matching network and derived using P_{gen} and P_{del} from the following relation:

Reproduced with permission of the copyright owner. Further reproduction prohibited without permission.

$$P_{gen} = P_{del} + P_{mn} \quad (2.1)$$

P_{coil} is the Ohmic power loss in the coil and calculated from the measured coil resistance, R_{coil} (= 0.08 Ω), and the measured rms rf coil current, I_{coilrf} [A_{rms}], as:

$$P_{coil} = I_{coilrf}^2 R_{coil} \quad (2.2)$$

Note that the coil resistance, R_{coil}, is measured at f_{rf} = 13.56 MHz, which is much larger than the DC coil resistance due to the skin effect. P_{abs} is the power absorbed in the plasma and defined as:

$$P_{del} = P_{abs} + P_{coil} \quad (2.3)$$

In our experiments, P_{del} and P_{abs} are used primarily in order to focus on the plasma-excitation coil interaction. In short, matching network power loss is excluded. P_{abs} based on the measured P_{del} and I_{coilrf} is used to check that the plasma electron density is unchanged with changing several plasma parameters, because the plasma electron density is approximately proportional to P_{abs} in our experimental condition as discussed in Section 3.1.

Reproduced with permission of the copyright owner. Further reproduction prohibited without permission.

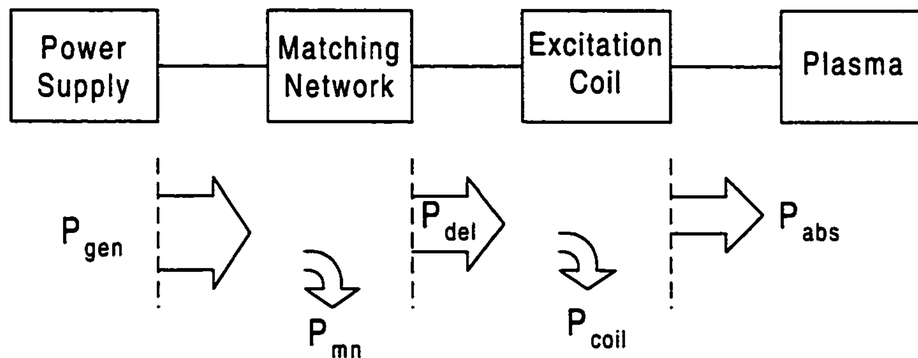

Figure 2.2 Five variables, P_{gen}, P_{mn}, P_{del}, P_{coil}, and P_{abs} to represent various powers. There are Ohmic losses in the matching network and the excitation coil represented by P_{mn} and P_{coil}, respectively.

In Chapters 3 and 5, three different dielectric window thicknesses, d_w [m], (d_w = 1.9 cm, 2.2 cm, 2.5 cm) are employed, as shown in Fig. 2.3, in order to determine the magnetic coupling coefficient, $k(d_w)$ between the excitation coil and the plasma, and the dielectric window capacitance, $C_w(d_w)$ [F]. In Chapter 4, only the 1.9 cm thick dielectric window is used. The 1.9 cm thick and the 2.2 cm thick dielectric windows are made entirely of quartz (relative permittivity $\varepsilon_r \sim 4$, relative permeability $\mu_r \sim 1$). As shown in Fig. 2.3, the 2.5 cm thick dielectric window is made of two quartz plates with 1.9 cm and 0.3 cm thick, respectively. There is a 0.3 cm wide air gap ($\varepsilon_r \sim 1$, $\mu_r \sim 1$) between the two quartz plates. Note that permittivity of air is different from that of quartz, so that both thickness and material composition of the dielectric window influence the dielectric window capacitance, C_w. However, the magnetic coupling coefficient k depends solely

Reproduced with permission of the copyright owner. Further reproduction prohibited without permission.

on the thickness of the dielectric window due to same permeability of air and quartz.

(i) d_w = 1.9

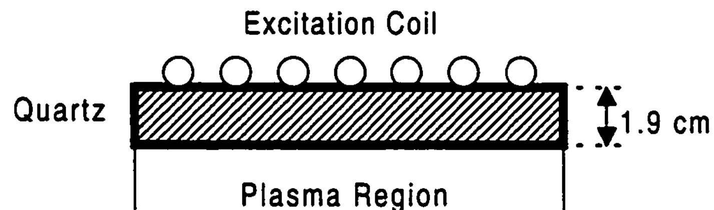

(ii) d_w = 2.2

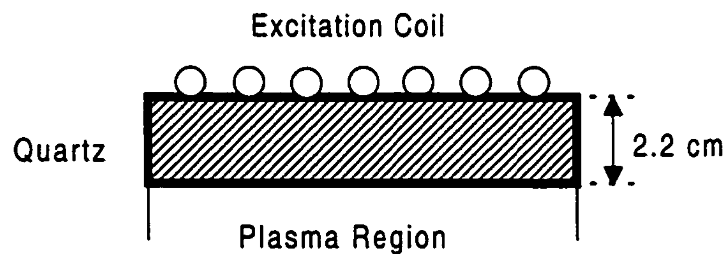

(iii) d_w = 2.5

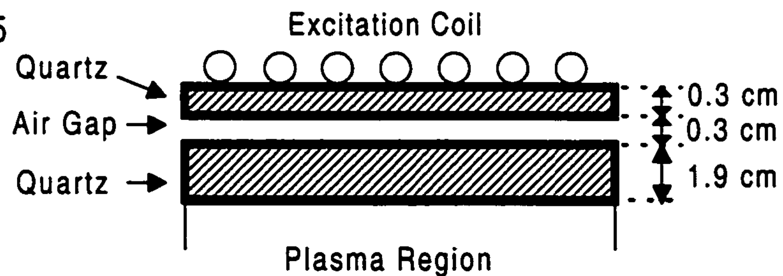

Figure 2.3 Three dielectric windows between the excitation coil and the plasma: (i) quartz window with d_w = 1.9 cm, (ii) quartz window with d_w = 2.2 cm, and (iii) quartz-air hybrid window with d_w = 2.5 cm. Note that quartz has $\varepsilon_r = 4$, $\mu_r = 1$, and air has $\varepsilon_r = \mu_r = 1$.

Reproduced with permission of the copyright owner. Further reproduction prohibited without permission.

2.2 Measurement Tools

Several diagnostic tools (Langmuir probe, B-dot probe and capacitive probe) used to measure the internal plasma parameters and fields are discussed in this section.

There are three fundamental parameters in the plasma of importance in this work, ambient gas pressure p [Torr], plasma electron density n_e [m^{-3}] and electron temperature T_e [eV]. The plasma impedance discussed in Chapter 3 is derived from plasma conductivity σ_p [Ω^{-1}-m^{-1}], which is a function of p and n_e, and plasma current geometry. The rf sheath capacitance discussed in Chapter 4 depends on n_e and T_e. Therefore, accurate measurements of these internal plasma parameters are crucial. The ambient gas pressure p can be accurately monitored by a commercial capacitance manometer pressure gauge. We designed a Langmuir probe to measure n_e and T_e.[4-6]

A standard B-dot probe is used to measure the rf magnetic flux induced by the rf current through the coil with no plasma in the plasma excitation region of the ICP chamber.[7] The measured magnetic flux is used to determine the relative change in the magnetic coupling coefficient k when varying the dielectric window thickness, d_w, as discussed in Chapter 3 and 5.

In Chapter 4, a capacitive probe is used to measure the rf plasma potential, V_{prf} [V], in the plasma to investigate the influence of the capacitive coupling. The measured V_{prf} is compared to V_{prf} calculated from the capacitive coupling model in order to verify the model.

Reproduced with permission of the copyright owner. Further reproduction prohibited without permission.

2.2.1 Langmuir probe

We designed a Langmuir probe used to measure the plasma electron density n_e and electron temperature T_e accurately. A metal probe is inserted in the plasma and positively or negatively biased to draw electron or ion current from the plasma. The probe current is measured while scanning the probe tip bias voltage, V_B [V]. This measured $I - V_B$ characteristics is used to determine n_e and T_e.[4]

Figure 2.4 shows the structure of a Langmuir probe and its operation circuit. The metal probe is positively or negatively biased and the electron and ion currents collected by the probe tip are measured. Figure 2.5 shows a typical $I - V_B$ Langmuir probe characteristic. When the Langmuir probe is negatively biased, the probe current is dominated by the positive ions incident on the probe tip. The current tends to saturate at the ion saturation current, I_{isat} [A]. This is because the ion flux incident into the probe tip is limited by the ion flux at the plasma-sheath boundary, which is primarily independent of the probe voltage. The probe current increases exponentially with increasing positive probe voltage. This is due to the increased electron current into the probe tip. At voltage higher than the plasma potential, $V_B > \Phi_p$ [V], the probe current tends to saturate at the electron saturation current, I_{esat} [A]. The saturation in the electron current is also due to the limited electron flux into the plasma-sheath

Reproduced with permission of the copyright owner. Further reproduction prohibited without permission.

boundary. When the probe current is zero, the probe potential is at the floating potential, $V_B = \Phi_f$ [V].

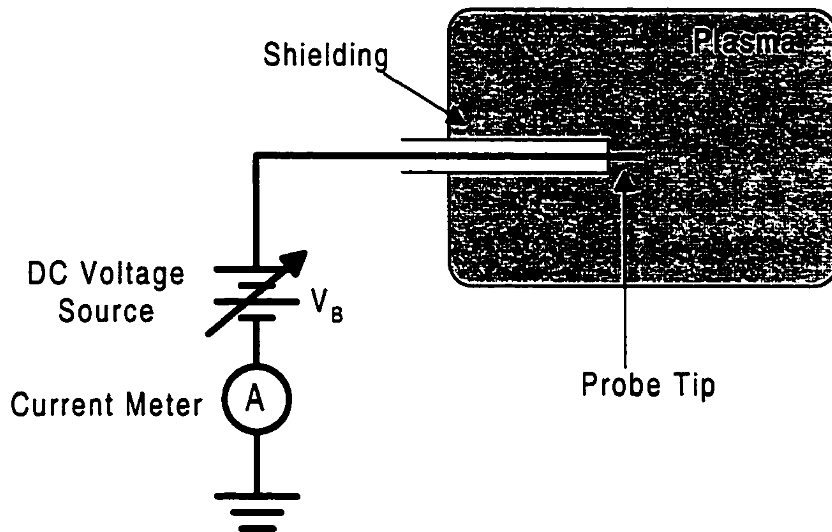

Figure 2.4 Schematic drawing of Langmuir probe and its operation circuit. the ion and electron currents are collected by the probe tip. The probe voltage, V_B, is scanned using a DC voltage source, and the probe current is measured.

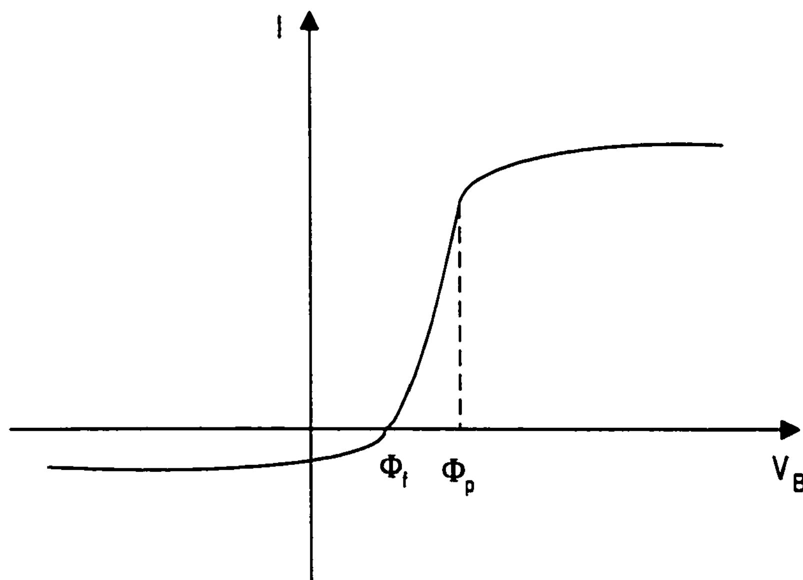

Figure 2.5 Typical Langmuir probe I – V_B characteristic. Φ_p and Φ_f are the plasma potential and the floating potential, respectively.

Reproduced with permission of the copyright owner. Further reproduction prohibited without permission.

The experimental $I - V_B$ characteristics from the planar Langmuir probe (Fig. 2.6(a)) shows clear saturation currents. This is because the plasma-sheath boundary area is approximately unchanged in the planar probe, even if the sheath width is changed by changing the probe voltage. However, the large probe current due to the large surface area may perturb the plasma.

The cylindrical Langmuir probe used herein is depicted in Fig. 2.6(b). The simple wire probe tip reduces the probe surface area, which results in small plasma perturbation. Figure 2.7 shows an example of $I - V_B$ characteristic measured by the cylindrical probe. The probe voltage is scanned from – 5 to 30 Volts and the probe current is measured at the plasma condition of P_{del} = 250 W and p = 10 mTorr. The cylindrical probe characteristics show broad ion and electron saturation currents. This is because the change in the sheath width by scanning the probe voltage changes the plasma-sheath boundary area, A_{sh} [m^2]. This changes the saturation currents collected by the probe, I_{sat}, for a constant saturation current densities, J_{sat} [A/m^2], due to $I_{sat} = J_{sat}A_{sh}$. Orbital Motion Limited (OML) theory[4-6] purposely uses the slopes of the ion and electron saturation currents to derive the plasma density from the following equation:

$$I_{sat} = 2en_t a_t d_t \sqrt{\frac{2e\,|\,\Phi_p - V_B\,|}{m}} \qquad (2.4)$$

where e is electron charge (=1.6022 × 10^{-19} C), n_t [m^{-3}] is ion or electron density

Reproduced with permission of the copyright owner. Further reproduction prohibited without permission.

at the plasma-sheath boundary, a_t [m] is radius of the probe tip, d_t [m] is length of the probe tip and m is mass of ion or electron. From Eq. (2.4), the slope of I-V_B characteristic is related to n_1. We apply Eq. (2.4) to the electron saturation current and obtain the plasma electron density n_e.

It is well known that the difference between the plasma potential, Φ_p, and the floating potential, Φ_f, is related to the electron temperature from the following equation, when Maxwellian electron energy distribution is assumed:[4]

$$\Phi_p - \Phi_f = \frac{T_e}{2}\ln\left(\frac{M}{2\pi m}\right) + \frac{T_e}{2} \approx 5.2T_e \quad \text{(for Ar)} \tag{2.5}$$

where M is the ion mass (= 6.64×10^{-26} kg for argon ion) and m is the electron mass (=9.11×10^{-31} kg). The measured Φ_f is typically a few Volts with respect to the ground in our experimental condition. From Eq. (2.5) increasing the electron temperature T_e increases $\Phi_p - \Phi_f$. We obtain the electron temperature T_e from the measured Φ_p and Φ_f applied to Eq. (2.5).

In the measurement of rf plasmas, rf noise from the plasma often causes significant error. Our Langmuir probe incorporates a LC filters next to the probe tip resonant at 13. 56 MHz and the first and second harmonics.[4]

The Langmuir probe is placed at a location 8 cm below the dielectric window and in the center radial position, r = 0. Typical values are $n_e = 10^{11}$ cm^{-3} and T_e = 3.2 eV at 2 mTorr argon and P_{gen} = 250 W.

Reproduced with permission of the copyright owner. Further reproduction prohibited without permission.

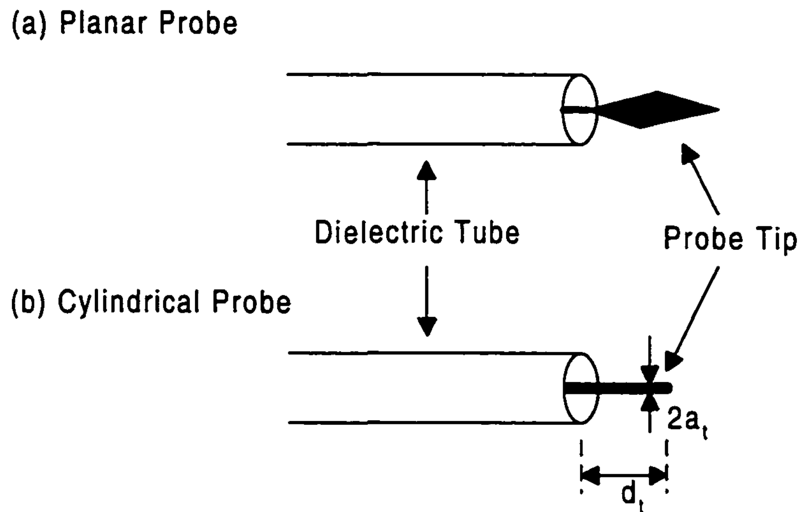

Figure 2.6 Designs of Langmuir probe tip: (a) planar probe tip, (b) cylindrical probe tip with radius, a_t, and length, d_t. The probes are surrounded by dielectric tubes to eliminate noise coupling from the plasma.

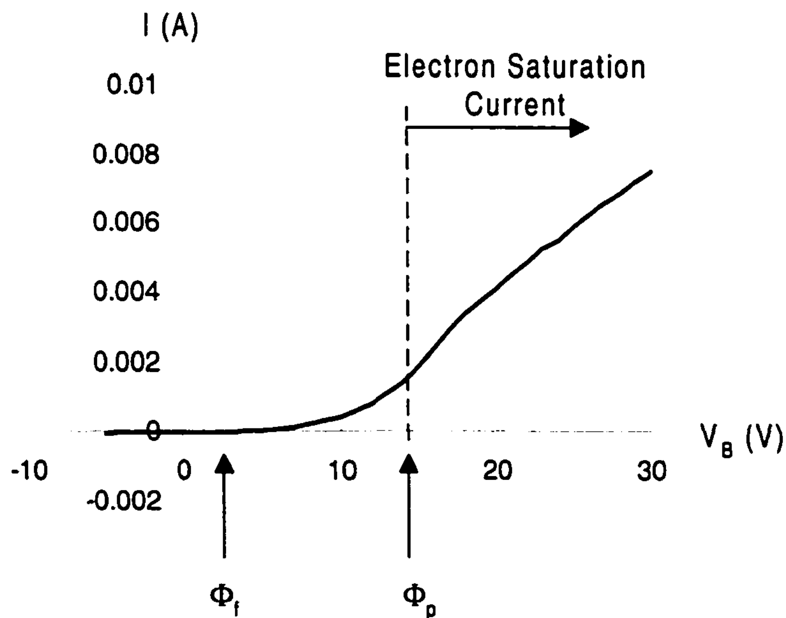

Figure 2.7 I – V_B characteristic measured by the cylindrical Langmuir probe, at ICP conditions of P_{del} = 250 W and p = 10 mTorr. Plasma electron density is calculated from the slope of the electron saturation current using Eq. (2.4).

Reproduced with permission of the copyright owner. Further reproduction prohibited without permission.

2.2.2 B-dot probe

The local magnetic flux in the plasma region is measured using a B-dot probe.[7] The B-dot probe consists of a one turn wire loop enclosing a small area (~ 10 mm^2) as shown in Fig. 2.8. Both ends of the wire are connected to the center line and the ground shield of a 50 Ω coaxial cable. A rf potential, V_{mrf} [V], is induced around the loop, which is related to the time variation of the magnetic flux through the loop, ϕ_{loop} [Wb], as follows:

$$V_{mrf} = \frac{d\phi_{loop}}{dt} = j\omega_{rf}\phi_{loop} \tag{2.6}$$

V_{mrf} is measured at the 50 Ω termination of a digital oscilloscope.

In this experiment, rf power at f_{rf} = 13.56 MHz is applied to the excitation coil ($\omega_{rf} = 2\pi f_{rf}$). Since the area of the probe tip is much smaller than the plasma chamber size, the measured V_{mrf} approximately represents the local magnetic flux at that location. The resolution of the local magnetic flux measurement is limited by the size of the B-dot probe (1.8 mm in diameter of the loop). The B-dot probe is placed 3 cm below the dielectric window and is moved parallel to the dielectric window surface (r-direction) to measure the spatial distribution of the local magnetic flux.

Reproduced with permission of the copyright owner. Further reproduction prohibited without permission.

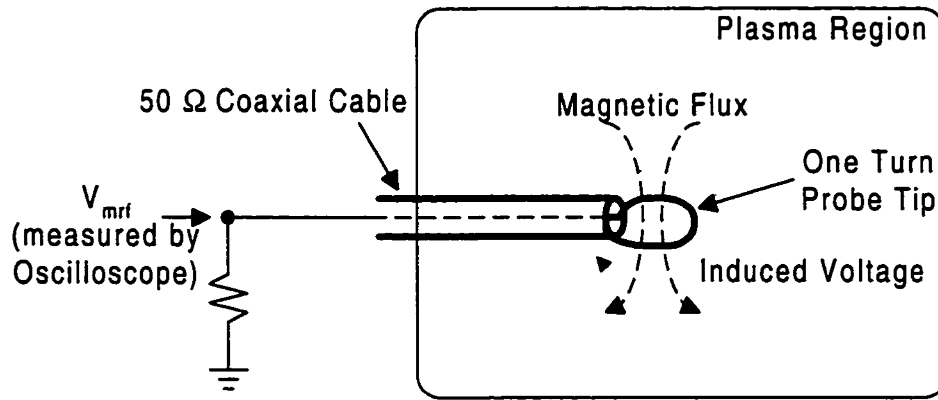

Figure 2.8 Geometrical configuration of B-dot probe. Time varying magnetic flux is coupled to the one turn probe tip, and a voltage is induced according to Faraday's law. The probe voltage is measured by an oscilloscope.

2.2.3 Capacitive plasma potential probe

The rf plasma potential, V_{prf}, is measured using a capacitive probe constructed by placing a length of semi-rigid, 50 Ω coaxial cable inside a Pyrex glass sleeve, as shown in Fig. 2.9.[8,9] The 10 mm long center conductor of the coaxial cable is capacitively coupled to the plasma through three capacitances:

(i) Sheath capacitance,

(ii) Glass sleeve capacitance,

(iii) Capacitance between the probe tip and the glass sleeve.

The grounded outside conductor of the coaxial cable shields unwanted rf noise from the plasma to the signal line. Any rf plasma potential induces a rf voltage

Reproduced with permission of the copyright owner. Further reproduction prohibited without permission.

signal across the probe tip through the three capacitances. The oscilloscope measures a rf voltage, V_{cprf} [V], at the 50 Ω termination, which is proportional to the rf plasma potential, V_{prf} [V], depending on the ratio of the three capacitances as shown in Fig. 2.10. We define the total of the three series capacitances as C_{cp} [F] and the 50 Ω termination impedance as R_{tm} [Ω], and the probe voltage, V_{cprf}. The relationship between the rf plasma potential, V_{prf}, and the probe voltage, V_{cprf}, is obtained for the following equations:

$$V_{cprf} = \left| \frac{j\omega_{rf} C_{cp} R_{tm}}{1 + j\omega_{rf} C_{cp} R_{tm}} \right| V_{prf} \tag{2.7}$$

$$V_{cprf} = \alpha V_{prf} \tag{2.8}$$

where

$$\alpha = \left| \frac{j\omega_{rf} C_{cp} R_{tm}}{1 + j\omega_{rf} C_{cp} R_{tm}} \right| \tag{2.9}$$

One can see that V_{cprf} is proportional to V_{prf} with a factor α, depending on ω_{rf} (= $2\pi f_{rf}$).

The capacitive probe is experimentally calibrated in the following way. The outside of the capacitive probe is covered with aluminum foil and a known rf voltage is applied to the foil. Then, the rf aluminum foil voltage and the rf probe voltage are measured. The ratio between the two voltages provides the calibration factor α (= 1.26×10^{-3}). Based on the calibration factor, we estimate

Reproduced with permission of the copyright owner. Further reproduction prohibited without permission.

the probe capacitance, $C_{cp} \approx 4$ pF. When the capacitive probe is inserted into the plasma, the sheath capacitance forms. However, the sheath width in the plasma is estimated to be much less (10 – 100 μm) than the glass sleeve thickness. Therefore, the sheath capacitance is neglected in the capacitive probe calibration described above.

The capacitive probe is typically placed at a location 8 cm below the quartz dielectric window and in the center radial position, r = 0. In order to measure the spatial distribution of the rf plasma potential, the capacitive probe can be moved in the chamber in the r-z plane.

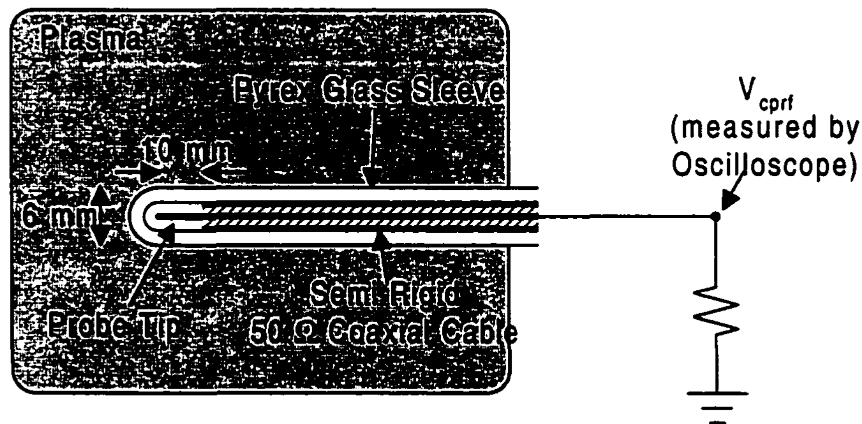

Figure 2.9 Geometrical configuration of capacitive probe. The rf plasma potential is capacitively coupled to the probe. The probe voltage is measured by an oscilloscope.

Reproduced with permission of the copyright owner. Further reproduction prohibited without permission.

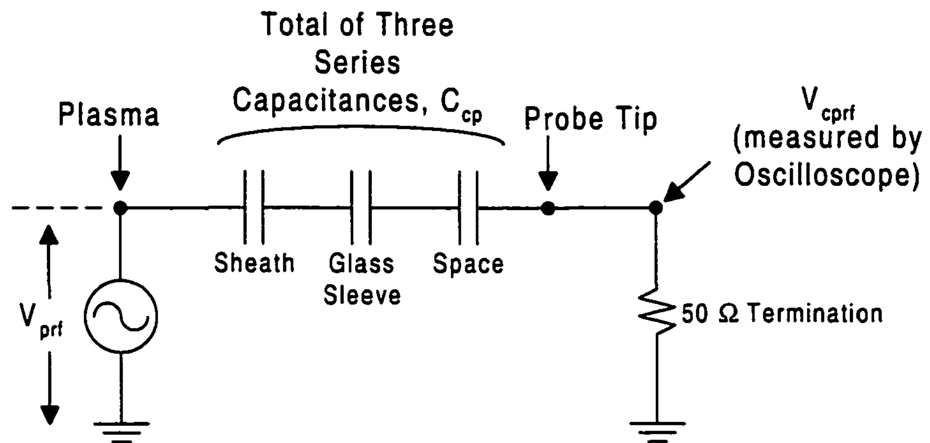

Figure 2.10 Equivalent circuit of the capacitive probe. The rf plasma potential is capacitively coupled to the probe tip through the three series capacitances, representing the rf sheath, the glass sleeve and the space between the probe tip and the glass sleeve.

Reproduced with permission of the copyright owner. Further reproduction prohibited without permission.

Chapter 2 References

1. M. Watanabe, D. M. Shaw, G. J. Collins, and H. Sugai, J. Appl. Phys. **85**, 3428 (1999).
2. H. Uchiyama, CSU M.S. Thesis "Comparison of the accuracy of three rf plasma impedance sensors on a planar inductively coupled plasma source at 13.56 MHz," (2000).
3. R. B. Piejak, V. A. Godyak, and B. M. Alexandrovich, Plasma Sources Sci. Technol. **1**, 179 (1992).
4. M. A. Lieberman, and A. J. Lichtenberg, "Principles of Plasma Discharges and Material Processing," John Wiley and Sons, New York (1994).
5. V. A. Godyak, R. B. Piejak, and B. M. Alexandrovich, J. Appl. Phys. **73**, 3657 (1993).
6. I. D. Sudit, and R. C. Woods, J. Appl. Phys. **76**, 4488 (1994).
7. J. Hopwood, C. R. Guarnieri, S. J. Whitehair, and J. J. Cuomo, J. Vac. Sci. Technol. A **11**, 147 (1993).
8. N. Benjamin, Rev. Sci. Instrum. **53**, 1541 (1982).
9. M. Yatsuzuka, K. Morishita, K. Satoh, and S. Nobuhara, Jpn. J. Appl. Phys., Part 1 **24**, 1724 (1985).

Reproduced with permission of the copyright owner. Further reproduction prohibited without permission.

CHAPTER 3 INDUCTIVE COUPLING IN ICP

Herein, we describe the previously developed ICP theory[1] and the expected variation of the electrical input impedance of the ICP, including both the excitation coil and the plasma (section 3.1). Our experimental data is compared to the theory in section 3.2.

3.1 Theoretical Description – Air Core Transformer Model

In an ICP system, rf current passing through the excitation coil produces a rf magnetic flux in the plasma region according to Ampere's law, as shown in Fig. 3.1. This rf magnetic flux induces a rf electric field in the plasma region via Faraday's law. The rf power is transferred to the plasma through electron heating caused by this rf electric field. As mentioned in Chapter 1, the ICP power transfer mechanism is analogous to an air core transformer as described in a model developed by Piejak et al., as shown in Fig. 3.2.[1] The inductive coupling model treats the plasma as the secondary circuit of the transformer. Therefore, we can simply apply fundamental electric circuit theory to study the ICP.

Reproduced with permission of the copyright owner. Further reproduction prohibited without permission.

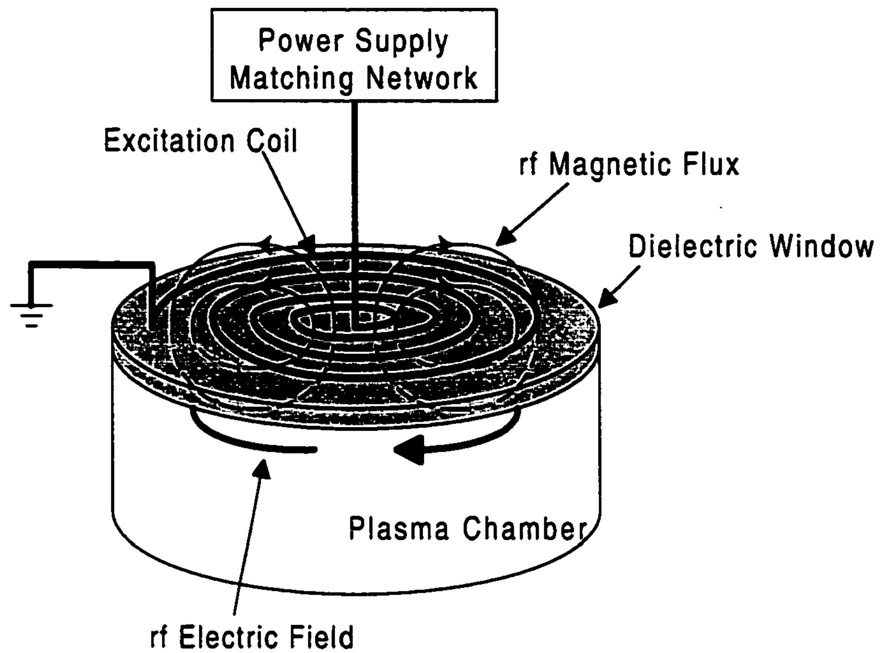

Figure 3.1 ICP power transfer mechanism. Applied rf current into the spiral excitation coil creates a rf magnetic flux according to Ampere's law, which induces a rf electric field in the plasma region according to Faraday's law.

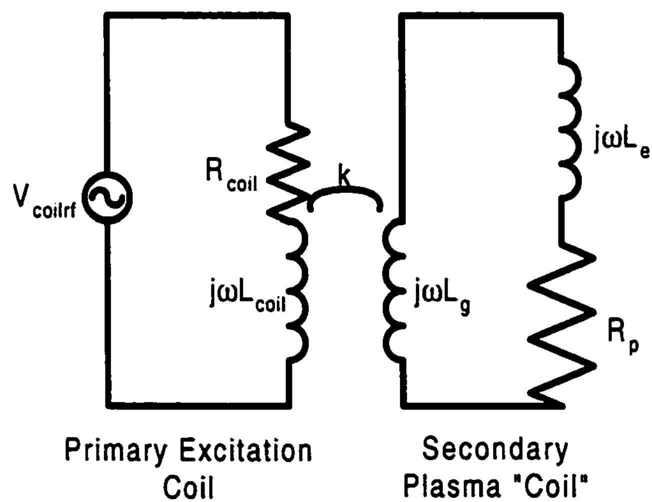

Figure 3.2 Air core transformer model of ICP developed by Piejak et al. The plasma is treated as the secondary circuit of an air core transformer, which is coupled to the promary excitation coil by magnetic coupling coefficient k.

Reproduced with permission of the copyright owner. Further reproduction prohibited without permission.

The excitation coil is considered the primary winding of the air core transformer with electrical impedance, Z_{coil} [Ω], as follows:

$$Z_{coil} = R_{coil} + j\omega_{rf}L_{coil} = R_{coil} + jX_{coil} \quad (3.1)$$

where R_{coil} [Ω] is the coil resistance representing Ohmic power loss and L_{coil} [H] is the coil inductance. Z_{coil} is experimentally measured using the plasma impedance monitor in our case (Z_{coil} = 0.08 + j87.2 Ω). Although the excitation coil is made of high conductivity metal such as copper, the coil resistance is relatively high due to skin effect, which forces most of the rf current to be carried in the outer 18 μm of the conductor.[2] The plasma is treated as a single turn coil with electrical impedance Z_p [Ω], which represents the secondary circuit of the transformer as follows:

$$Z_p = R_p + j\omega_{rf}(L_g + L_e) = R_p + jX_p \quad (3.2)$$

where R_p [Ω] is the plasma resistance into which the inductive power is transferred, L_e [H] is the electron inertia inductance, and L_g [H] is the geometric inductance of the ICP current path.

Assuming the plasma as a torroidal conductor having radius, a_p [m], and ring radius, r_p [m], as shown in Fig. 3.3, we can estimate R_p, L_e and L_g. Plasma has a complex plasma conductivity, σ_p [Ω^{-1}-m^{-1}]:[3]

Reproduced with permission of the copyright owner. Further reproduction prohibited without permission.

$$\sigma_p = \frac{e^2 n_e}{m(\nu_m + j\omega_{rf})} \qquad (3.3)$$

where m is the electron mass (= 9.11 × 10^{-31} kg) and ν_m [Hz] is momentum transfer collision frequency between electrons and ambient gas atoms. The real part of $1/\sigma_p$ attributes to the plasma resistance and the imaginary part attributes to the electron inertia inductance. The plasma resistance, R_p, and the electron inertia inductance, L_e, can be expressed as:

$$R_p = \mathrm{Re}\left(\frac{2\pi r_p}{\pi a_p^2 \sigma_p}\right)$$

$$= \nu_m \frac{2 r_p m}{a_p^2 e^2 n_e} \qquad (3.4)$$

$$j\omega_{rf} L_e = \mathrm{Im}\left(\frac{2\pi r_p}{\pi a_p^2 \sigma_p}\right)$$

$$= j\omega_{rf} \frac{2 r_p m}{a_p^2 e^2 n_e} \qquad (3.5)$$

$$L_e = \frac{2 r_p m}{a_p^2 e^2 n_e} \qquad (3.6)$$

R_p depends on the geometric terms, a_p and r_p, the plasma electron density n_e

Reproduced with permission of the copyright owner. Further reproduction prohibited without permission.

[m^{-3}] and the momentum transfer collision frequency ν_m. L_e depends on a_p, r_p and n_e. The electron density n_e is approximately proportional to the plasma absorbed power P_{abs} [W] from the following equation:[3]

$$P_{abs} = en_e u_B A_{pl} E_T \tag{3.7}$$

where u_B [m/s] is the Bohm velocity , A_{pl} [m^2] is the area of particle loss and E_T [eV] is the total energy loss per ion. ν_m is approximately proportional to the ambient gas pressure p [Torr]. The geometric inductance, L_g, is solely determined by the assumed geometry of the plasma electron current path:

$$L_g = \mu_0 r_p \left\{ \ln\left(\frac{8r_p}{a_p} \right) - 2 \right\} \tag{3.8}$$

where μ_0 is permeability for free space (= $4\pi \times 10^{-7}$ H/m). Exact analytical determination of the plasma current path geometry is quite difficult due to the diffuse and geometrically distributed nature of the plasma "coil". However, if the plasma "coil" geometry, a_p and r_p, the gas pressure p and the plasma absorbed power, P_{abs}, are unchanged, the three plasma impedance elements R_p, L_e and L_g are unchanged regardless of other plasma parameters.

Reproduced with permission of the copyright owner. Further reproduction prohibited without permission.

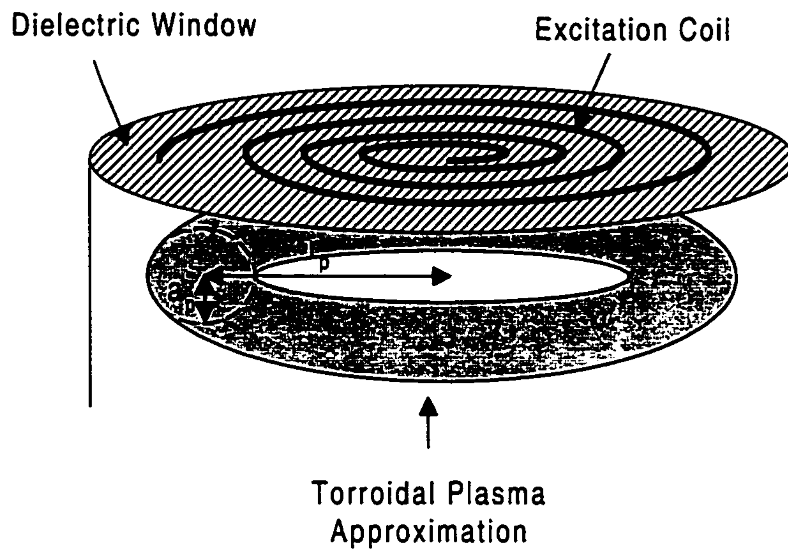

Figure 3.3 Torroidal plasma ring approximation. a_p is the plasma radius, and r_p is the ring radius.

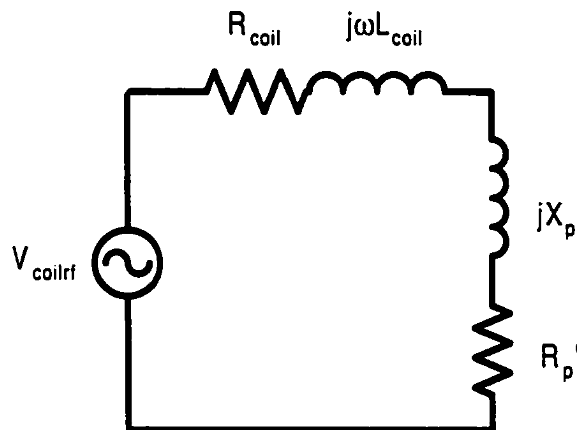

Figure 3.4 Equivalent circuit of the air core transformer (inductive coupling) model. The secondary plasma circuit is transferred to the primary circuit (= R_p' + jX_p'). The coil impedance (= R_{coil} + $j\omega L_{coil}$) remains the same.

Reproduced with permission of the copyright owner. Further reproduction prohibited without permission.

The plasma secondary "coil" is magnetically coupled to the primary excitation coil between L_g and L_{coil} through the magnetic coupling coefficient k. Figure 3.4 shows the equivalent circuit of the inductive coupling model of ICP as seen from the transformer primary input. The coil impedance in the equivalent circuit does not change. The plasma impedance values referred to the primary side are modified:

$$R_p' = \omega_{rf}^2 k^2 L_{coil} L_g \frac{R_p}{Z_p^2} \tag{3.9}$$

$$X_p' = -\omega_{rf}^2 k^2 L_{coil} L_g \frac{\omega_{rf}(L_g + L_e)}{Z_p^2} \tag{3.10}$$

where

$$Z_p^2 = R_p^2 + \omega_{rf}^2 (L_g + L_e)^2 \tag{3.11}$$

Note that the primed term is the secondary side value referred to the primary side of the circuit. The real part and imaginary part of the impedance at the excitation coil input, R_{in} and X_{in}, may be written as:

$$R_{in} = R_{coil} + R_p' \tag{3.12}$$

$$X_{in} = X_{coil} + X_p' \tag{3.13}$$

From the above equations, the inductive coupling model quantitatively describes Z_{in} of the ICP in terms of three sets of parameters:

Reproduced with permission of the copyright owner. Further reproduction prohibited without permission.

(i) The excitation coil geometry and its electrical impedance, Z_{coil}.

(ii) The plasma absorbed power P_{abs} and feedstock gas type and pressure p and plasma secondary "coil" geometry, which sets the plasma impedance Z_p.

(iii) The magnetic coupling between the excitation coil and the plasma described by the coupling coefficient k ($0 \leqq k \leqq 1$).

Referring to Eq. (3.12), R_p' [Ω] is determined experimentally by subtracting the known coil resistance, R_{coil}, from the total measured input resistance, R_{in}, in our study. Similarly, X_p' [Ω] is determined experimentally from Eq. (3.13). Note that X_p' is negative in value, because the plasma secondary circuit tends to cancel the magnetic flux induced by the primary circuit, which reduces the total inductance. We will discuss only the absolute value, $|X_p'|$, from this point on for simplicity.

From Eq. (3.9), R_p' is proportional to k^2 for a given plasma condition where Z_p is constant. This means that large inductive coupling represented by large k gives large R_p'. The rf power provided to the excitaion coil is consumed by Ohmic losses in the coil, P_{coil}, and the plasma, P_{abs}, with the ratio of $R_{coil} : R_p$'. The increase in R_p' increases P_{abs} for a constant total delivered power, P_{del}. Better inductive coupling is represented by larger k, $k \rightarrow 1$, which more efficiently transfers the delivered power to the plasma.

Reproduced with permission of the copyright owner. Further reproduction prohibited without permission.

If the inductive coupling is decreased, for example, by increasing the distance between the excitation coil and the plasma, R_p' is also decreased. This reduces power transfer efficiency to the plasma and results in lower plasma density for a given P_{del}, because the plasma density is proportional to P_{abs} as seen in Eq. (3.7). In order to keep the same P_{abs} with decreasing k, I_{coil} [A_{rms}] must be increased to satisfy the following equation:

$$P_{abs} = R_p' I_{coil}^2 \tag{3.14}$$

Under the condition where Z_{in} is constant with varying k, the rf coil voltage also increases according to the following equation:

$$V_{coil} = |Z_{in}|\, I_{coil} \tag{3.15}$$

To summarize, increasing the dielectric window thickness requires a higher rf coil voltage to sustain the same plasma density. Note that higher rf coil voltage causes larger capacitive coupling from the excitation coil to the plasma as will be discussed in Chapter 5.

In the inductive coupling model, the plasma is simplified as an air core transformer by neglecting the following effects seen in actual ICP's.

Reproduced with permission of the copyright owner. Further reproduction prohibited without permission.

(i) The plasma can not be simply represented by circuit elements such as resistance and inductance. This non-linear plasma impedance causes harmonics to the rf circuit.

(ii) Parasitic capacitive coupling through a few cm thick dielectric window might be significant, since the rf voltage at the excitation coil input often exceeds 1 kV.

Therefore, the validity of the inductive coupling model might be limited in practical ICP systems. It is desired to experimentally verify the effectiveness of the inductive coupling model. In section 3.2.2, the relationship between k and R_p' and between k and $|X_p'|$ are measured by changing k with a constant P_{abs}, p, and the plasma secondary "coil" geometry. By comparing the measured data to the theoretical data from the inductive coupling model, the effectiveness of the inductive coupling model is discussed.

3.2 Experiment and Discussion

Among the electrical parameters used in the inductive coupling model, R_{in}, X_{in}, R_{coil} and X_{coil} are measurable using the rf plasma impedance monitor described in Chapter 2. R_p' and X_p' are calculated from these measured data. The direct analysis of R_p' and X_p' is quite difficult. These terms are a complicated function of several unknown and unmeasurable plasma parameters such as k, L_g, L_e and R_p. Suzuki et al. have calculated k, L_g, L_e and R_p for a simple one turn excitation coil ICP.[4] However, their technique is inappropriate

Reproduced with permission of the copyright owner. Further reproduction prohibited without permission.

in more complicated excitation coil geometry such as the spiral coil used in our experiment.

3.2.1 Magnetic coupling coefficient k

As mentioned above, the accurate determination of both Z_p and k is quite complicated. Our approach is to measure the relative change in magnetic coupling coefficient k, and measure the effect of this change in k on the total input impedance ($Z_{in} = R_{in} + jX_{in}$). In this technique, absolute values of L_g, L_e or R_p are not necessary. We vary only k, while L_g, L_e and R_p remain constant. Therefore, the change in measured Z_{in} is due primarily to the change in k.

A change in the dielectric window thickness, d_w [m], changes the distance from the excitation coil to the plasma, which changes inductive coupling between the coil and the plasma. This is represented by magnetic coupling coefficient $k(d_w)$ as a function of the dielectric window thickness d_w. We assume that at a given P_{abs} and p, the effective plasma secondary "coil" will have the same impedance Z_p regardless of k, which varies as the window thickness varies.

The measured magnetic coupling coefficient k depends on the fractional coupling of magnetic flux between the primary excitation coil and the secondary plasma "coil". Suppose for illustration purpose there are two coils, c_1 and c_2 as shown in Fig. 3.5. By applying a current I_1 [A] on c_1, some amount of magnetic flux, ϕ_2 [Wb], transverses c_2. This relation is expressed as:

Reproduced with permission of the copyright owner. Further reproduction prohibited without permission.

$$\phi_2 = M_{12} \cdot I_1 \quad (3.16)$$

$$= k\sqrt{L_1 L_2} \cdot I_1 \quad (3.17)$$

where M_{12} [H] is mutual inductance between c_1 and c_2. The mutual inductance M_{12} may be written in terms of k and self inductance L_1 [H] for c_1 and L_2 [H] for c_2 as:

$$M_{12} = k\sqrt{L_1 L_2} \quad (3.18)$$

One can see from Eq. (3.17) that the magnetic flux on c_2, ϕ_2, is proportional to k for a given I_1.

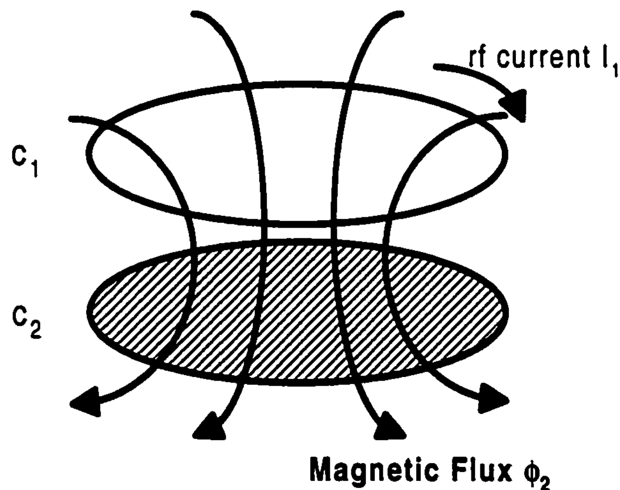

Figure 3.5 Schematic drawing of two coils, c_1 and c_2 to illustrate the magnetic coupling coefficient k between the two coils. k is defined by the portion of the magnetic flux f_2 captured by c_2 when applying rf current I_1 to c_1.

Reproduced with permission of the copyright owner. Further reproduction prohibited without permission.

In the case of an ICP, the excitation coil and the plasma secondary "coil" are considered to be c_1 and c_2, respectively, and the relation derived in Eq. (3.16) – (3.18) may be expressed as:

$$\phi_p = k\sqrt{L_{coil}L_g} \cdot I_{coil} \tag{3.19}$$

where ϕ_p [Wb] is the rf magnetic flux induced by the excitation coil of inductance L_{coil}, which couples through the distributed plasma secondary "coil" of inductance L_g. By measuring Φ_p for constant L_{coil}, L_g and I_{coil}, while varying the dielectric window thickness, we can obtain the relative change in the magnetic coupling coefficient, $k_r(d_w)$, for various dielectric window thicknesses, d_w. Using $k_r(d_w)$ obtained from this method, we will analyze the experimental Z_{in} measured using the plasma impedance monitor to verify the accuracy of the inductive coupling model.

In this experiment, we assume the magnetic flux ϕ_p to be proportional to the line integral normal to the measured magnetic flux:

$$\phi_p \propto \int \dot{B}_z dr \tag{3.20}$$

where $\dot{B}_z$ is the time varying magnetic flux density normal to the plasma "coil" plane. The spatial distribution of $\dot{B}_z$ is measured 3 cm below the dielectric

Reproduced with permission of the copyright owner. Further reproduction prohibited without permission.

window in the plasma region with the plasma OFF, as sketched in Fig. 3.6. This measurement is repeated for the three dielectric window thickness d_w (d_w = 1.9, 2.2 and 2.5 cm) with a fixed I_{coil}, which results in three $\dot{B}_z(d_w)$ values. By assuming L_{coil}, L_g and I_{coil} are fixed, the relative changes in the magnetic coupling coefficient, which we term $k_r(d_w)$ for d_w = 1.9, 2.2 and 2.5 cm, are derived from Eq. (3.19) and (3.20).

Figure 3.7 shows the k_r data calculated from $\dot{B}_z(d_w)$ measurements for the three different dielectric window thicknesses. Note that $k_r(d_w)$ for d_w = 2.2 cm and d_w = 2.5 cm are normalized to that for the d = 1.9 cm dielectric window ($k_r(1.9)$ = 1) to achieve a clearer comparison between conditions. The measured result shows that k_r decreases monotonically with increasing d_w. This is because the magnetic flux in the plasma region decreases as the excitation coil moves farther away. The measured $k_r(d_w)$ will be used for the analysis of Z_{in} in the next section.

Reproduced with permission of the copyright owner. Further reproduction prohibited without permission.

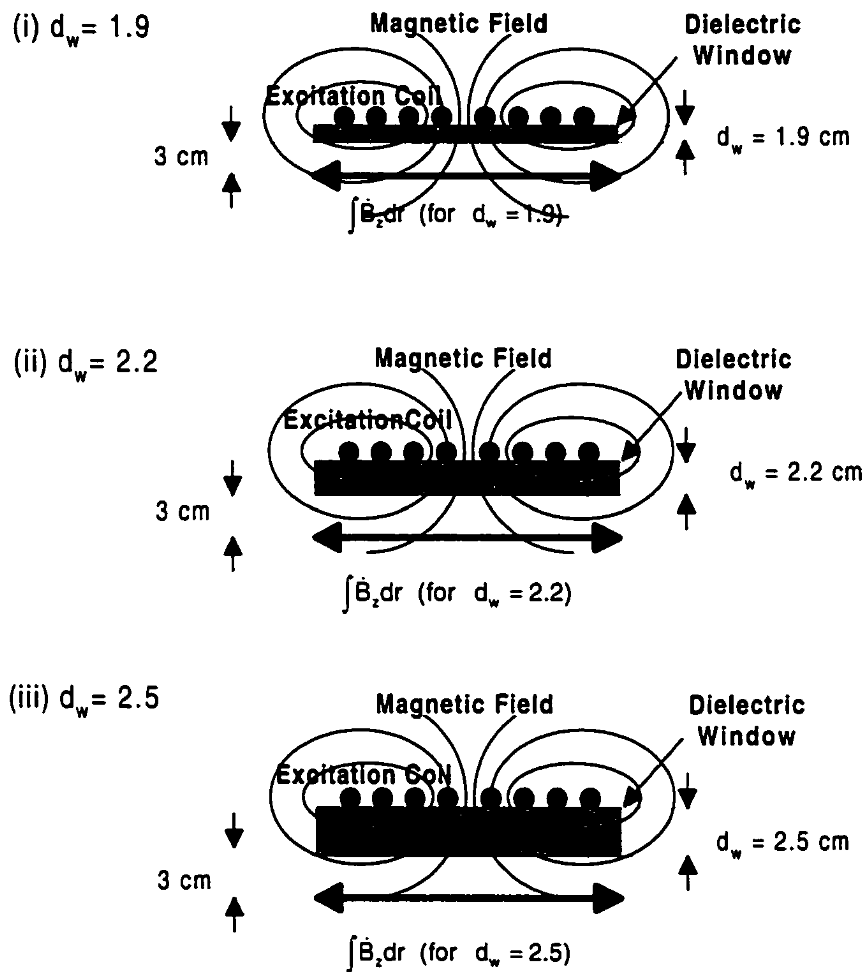

Figure 3.6 Schematic drawing of the spatial integration of the local magnetic flux path for the three dielectric window thicknesses: (i) d_w = 1.9, (ii) d_w = 2.2, and (iii) d_w = 2.5, employed to calculate the magnetic flux fp induced in the plasma region by the rf coil current. Note that the scale in the drawing is not accurate.

Reproduced with permission of the copyright owner. Further reproduction prohibited without permission.

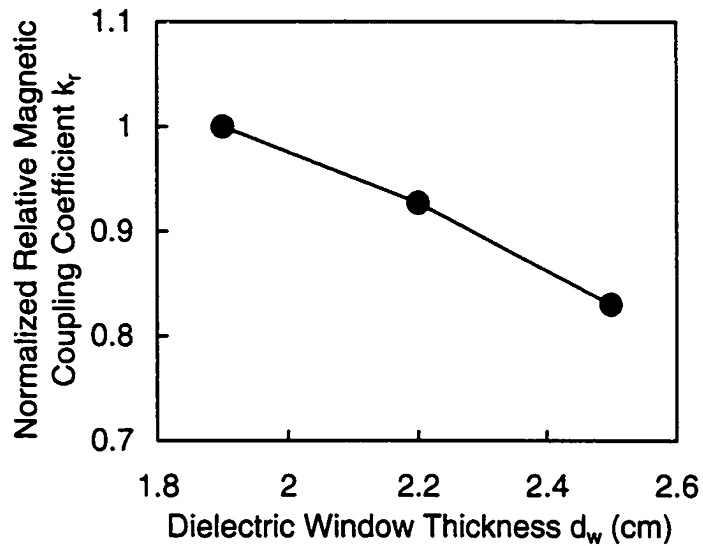

Figure 3.7 Normalized relative magnetic coupling coefficient k_r for d_w = 1.9, 2.2, 2.5 cm measured by the B-dot probe. k_r monotonically decreases as d_w increases.

3.2.2 rf input impedance: Z_{in}

Figures 3.8(a) - (d) and 3.9(a) - (d) show the measured and theoretical R_p' and $|X_p'|$ versus P_{abs} for the three different dielectric window designs in p = 1, 2, 5, 20 mTorr of argon gas.

Note that at a given P_{abs} and p, the plasma condition is assumed to be unchanged regardless of differing dielectric window thickness. This is also experimentally verified from the measurement of n_e and T_e for a given P_{abs} and p with varying the dielectric window thickness. Therefore, the experiment is

Reproduced with permission of the copyright owner. Further reproduction prohibited without permission.

conducted at constant R_p, L_g and L_e, while the three different dielectric window thicknesses are employed. In other words, $k_r(d_w)$ is varied, while R_p, L_g and L_e remain constant.

One can see from Fig. 3.8 that R_p' increases with increasing P_{abs} in the low power range. For the argon pressure of 5 and 20 mTorr, R_p' has a broad peak and decreases with increasing P_{abs}. $|X_p'|$ increases with increasing P_{abs} for all pressure range in this experiment as seen in Fig. 3.9. The theoretical explanation of the R_p' - P_{abs} and $|X_p'|$ - P_{abs} characteristics is outside the focus of this work and is described elsewhere.[5] At a given plasma condition, both measured R_p' and $|X_p'|$ decrease with increasing d_w. This is qualitatively explained from the fact that the magnetic coupling between the excitation coil and the plasma is reduced with increasing distance between the two. Lower magnetic coupling results in smaller plasma impedance transferred to the primary circuit Z_p' due to less interaction between the secondary circuit and the primary.

From Eq. (3.9) and (3.10), R_p' and $|X_p'|$ are proportional to $k_r(d_w)^2$ for a given plasma condition, where $k_r(1.9) = 1$ from the definition of k_r, and $k_r(2.2) = 0.85$ and $k_r(2.5) = 0.7$ from Fig. 3.7. Therefore, for constant R_p, L_g and L_e, the resistance and reactance transferred to the primary circuit R_p' and $|X_p'|$ for d_w = 2.2 cm will be:

$$R_p'(2.2) = 0.85^2 \times R_p'(1.9) \qquad (3.21)$$

Reproduced with permission of the copyright owner. Further reproduction prohibited without permission.

$$|X_p'(2.2)| = 0.85^2 \times |X_p'(1.9)| \tag{3.22}$$

and those for d_w = 2.5 cm will be:

$$R_p'(2.5) = 0.7^2 \times R_p'(1.9) \tag{3.23}$$

$$|X_p'(2.5)| = 0.7^2 \times |X_p'(1.9)| \tag{3.24}$$

These points are also plotted in Figs. 3.8 and 3.9 as theoretical values derived from the inductive circuit model. Both measured and theoretical R_p' and $|X_p'|$ values are close over the entire range of P_{abs} investigated. The agreement of the measured and theoretical results indicates that the inductive coupling model is effective to explain the power transfer mechanism in ICP's. However, the observed rf plasma potential variations in the ICP are not explained by this simple model. As discussed in Chapter 4, a new capacitive coupling model must be introduced.

Reproduced with permission of the copyright owner. Further reproduction prohibited without permission.

(a) 1 mTorr

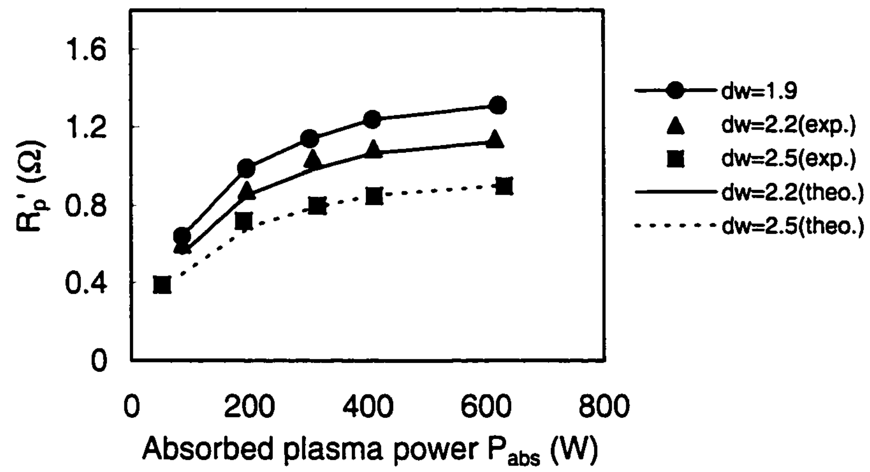

(b) 2 mTorr

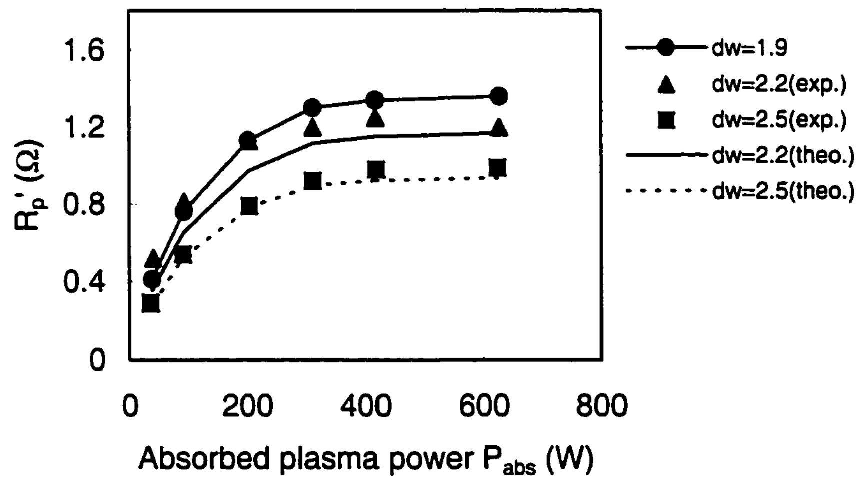

Reproduced with permission of the copyright owner. Further reproduction prohibited without permission.

(C) 5 mTorr

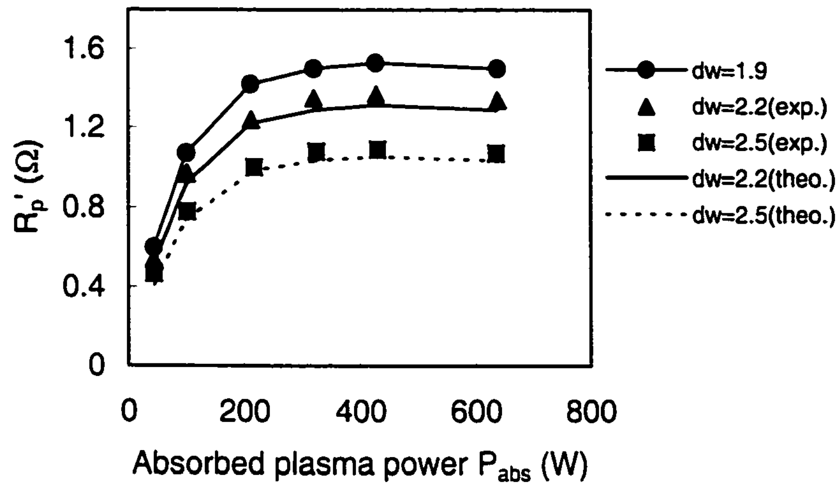

(d) 20 mTorr

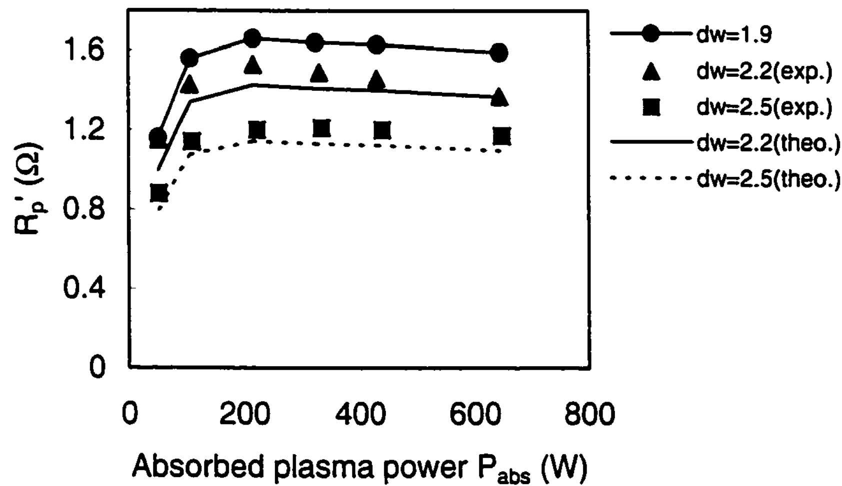

Figure 3.8 Measured plasma resistances transferred to the primary circuit R_p' versus absorbed plasma power P_{abs} for four argon pressures: (a) 1 mTorr, (b) 2 mTorr, (c) 5 mTorr, and (d) 20 mTorr. "exp." indicates the experimental values, and "theo." indicates the theoretical values for d_w = 2.2 and 2.5 cm.

Reproduced with permission of the copyright owner. Further reproduction prohibited without permission.

(a) 1 mTorr

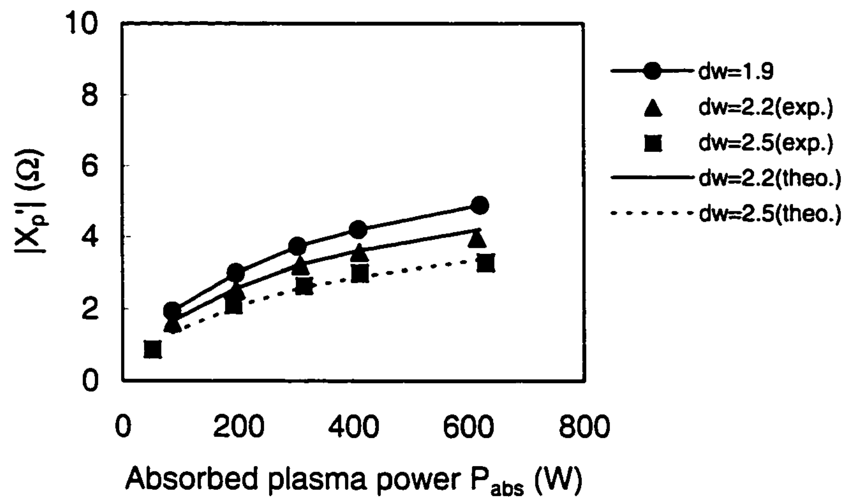

(b) 2 mTorr

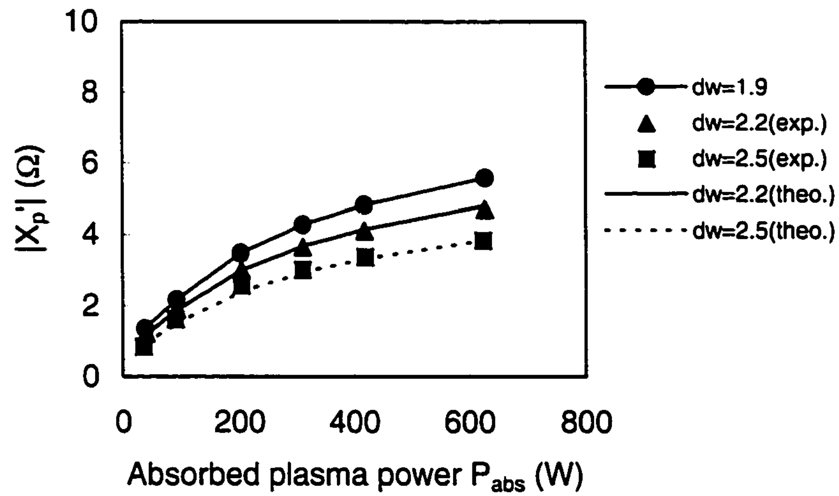

Reproduced with permission of the copyright owner. Further reproduction prohibited without permission.

(c) 5 mTorr

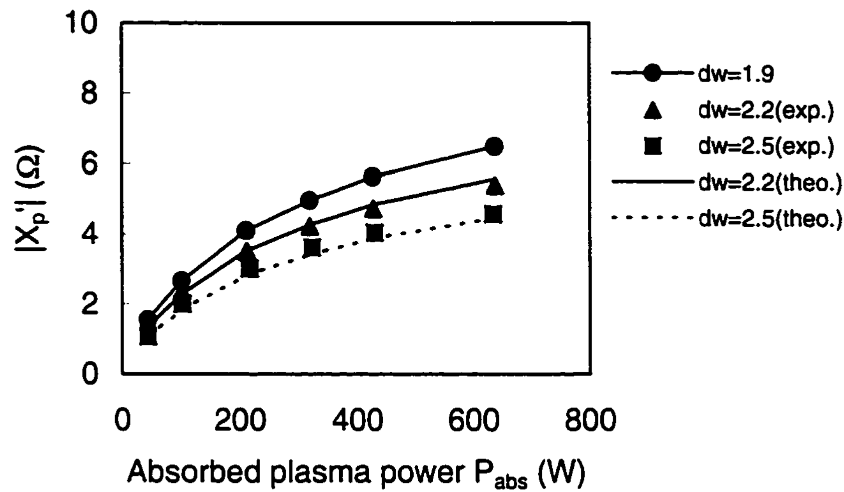

(d) 20 mTorr

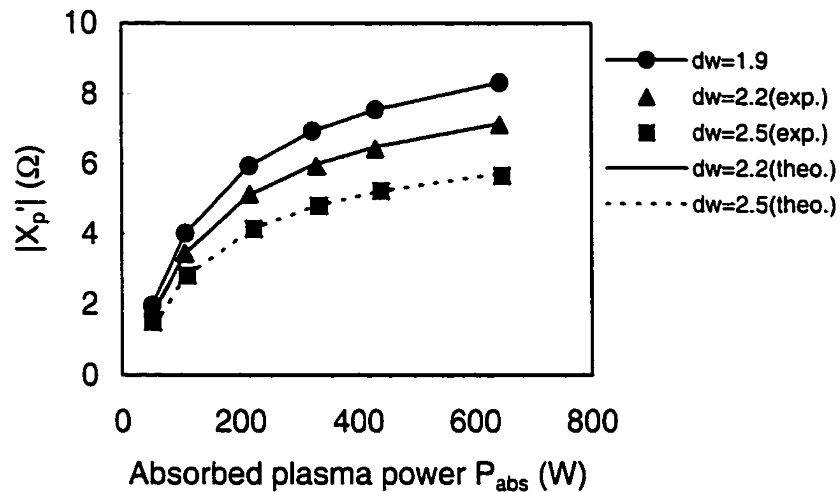

Figure 3.9 Measured plasma reactance transferred to the primary circuit $|X_p'|$ versus absorbed plasma power P_{abs} for four argon pressures: (a) 1 mTorr, (b) 2 mTorr, (c) 5 mTorr, and (d) 20 mTorr. Note that the absolute values are shown in the figure. "exp." indicates the experimental values, and "theo." indicates the theoretical values for d_w = 2.2 and 2.5 cm.

Reproduced with permission of the copyright owner. Further reproduction prohibited without permission.

Chapter 3 References

1. R. B. Piejak, V. A. Godyak, and B. M. Alexandrovich, Plasma Sources Sci. Technol. **1**, 179 (1992).
2. D. K. Cheng, "Field and Wave Electromagnetics," Addison-Wesley (1985).
3. M. A. Lieberman, and A. J. Lichtenberg, "Principles of Plasma Discharges and Material Processing," John Wiley and Sons, New York (1994).
4. K. Suzuki, K. Nakamura, H. Ohkubo, and H. Sugai, Plasma Sources Sci. Technol. **7**, 13 (1998).
5. D. M. Shaw, CSU M.S. Thesis "Characterization of a planar inductively coupled plasma system" (1999).

Reproduced with permission of the copyright owner. Further reproduction prohibited without permission.

CHAPTER 4 CAPACITIVE COUPLING IN ICP

Herein, the capacitive coupling theory is developed (section 4.1), and experimentally verified (section 4.2).

4.1 Theoretical Description of the ICP, Including Capacitive Coupling

To obtain a high density (> 10^{11} cm^{-3}) ICP, typically more than 10 A of current of 13.56 MHz must be applied to the excitation coil, whose diameter exceeds 20 cm in the experimental system used herein. Due to the inductance of the excitation coil, the rf voltage at the coil input often exceeds 1 kV, which opens parasitic capacitive current pathways from the high voltage excitation coil to the plasma.[1-6] The rf displacement current passes through the thin (a few cm thick) dielectric window.

For the rf capacitive current to flow from the excitation coil to the plasma, the rf current pathways may be represented by a series of capacitors.[1,5,6] The two primary capacitors are the dielectric window and the plasma sheath. The former is easy to model, but the latter is difficult because the dielectric window-to-plasma sheath and the plasma-to-wall surface sheath capacitances are hard to determine. The rf sheath properties are complicated and vary greatly with plasma conditions. Only a few theories have been developed to study the rf

Reproduced with permission of the copyright owner. Further reproduction prohibited without permission.

sheath.[1,7,8] We choose the rf sheath theory developed by Godyak et al.[7] to obtain the rf sheath capacitance as discussed in Section 4.1.1. In Section 4.1.2, we developed a new capacitive coupling model[6] based on Godyak's rf sheath theory, and verified it by comparison with experimental data.

As mentioned in Chapter 1, capacitive coupling causes the dielectric window sputtering.[2,3,8,10] The details of the sputtering mechanism are described in Section 4.1.3.

4.1.1 rf sheath theory

The sheath forms the interface between the bulk plasma and a surface. In our case, two surfaces are considered: the dielectric window on which the excitation coil is placed, and the grounded chamber wall. The sheath forms in order to maintain the same amount of positive and negative charge fluxes to the wall surface in steady state. Due mainly to much smaller electron mass (e. g. 73000 times smaller than Ar mass), electrons have much higher mean velocity. Therefore, a sheath potential is built up that repels excessive electrons incident from the bulk plasma to the wall surface. This electric field is self-adjusted by the plasma to equalize charge particle flow to the wall surface in steady state conditions.

DC sheath theory is well known[1] and the analysis of the sheath characteristics is relatively straightforward. However, if there is a significant rf component in the sheath potential, the analytical solution for the sheath

Reproduced with permission of the copyright owner. Further reproduction prohibited without permission.

characteristics becomes non-linear. This non-linearity between the rf sheath potential and the rf sheath current creates harmonics, which we must take into account. Godyak et al. developed a theory for the rf plasma sheath,[7] from which we can obtain the first order value of the sheath capacitance. However, this simplified rf sheath theory limits the applied rf driving frequency, ω_{rf} [rad/s], and the plasma ion and electron frequencies, ω_{pi} and ω_{pe} [rad/s], respectively, to:

$$\omega_{pi}^{2} << \omega_{rf}^{2} \tag{4.1}$$

$$\omega_{pe}^{2} >> \omega_{rf}^{2}\sqrt{1+\frac{\nu_{e}^{2}}{\omega_{rf}^{2}}} \tag{4.2}$$

where $\omega_{rf} = 2\pi \times (13.56 \times 10^{6})$ [rad/s] in our experiment, and ν_e [Hz] is effective momentum transfer collision frequency between electrons and atoms.[7] Mathematical constraints in Eqs. (4.1) and (4.2) have the physical meaning that the ions respond only to the time-averaged sheath potentials (DC sheath potential), while the electrons respond to the instantaneous sheath potential and carry the rf current. Our experimental conditions (10^{9} cm^{-3} < n_e < 10^{11} cm^{-3}, 1 mTorr < p < 20 mTorr) are well suitable to the above assumptions. Furthermore, for additional simplicity of the sheath model, the following four conditions are also assumed:

Reproduced with permission of the copyright owner. Further reproduction prohibited without permission.

(i) A symmetrical driven capacitively coupled plasma (CCP) is assumed. That is, opposing metallic electrodes have the same applied rf voltages with 180° out of phase. Therefore, the sheath characteristics on the two opposing electrodes are exactly the same.

(ii) The sheath is assumed collisionless. This assumption avoids employing more complicated collisional sheath theory. The pressure range in our experiment (1 mTorr $< p <$ 20 mTorr) is suitable for the collisionless case.

(iii) The rf displacement current is much larger than the ion conduction current within the rf sheath. This assumption allows us to neglect the ion and electron conduction current to the wall surface, which creates further harmonics in the rf current.

(iv) Electron temperature T_e is much higher than the ion temperature.

The assumption (i) eliminates most of the harmonics in the rf current, which enables the assumption of sinusoidal rf current through the sheath. However, our ICP system is heavily asymmetrical, which may create significant amount of higher harmonics. This is discussed later. The assumptions (ii) – (iv) are appropriate for our ICP.

Figure 4.1 shows the rf sheath structure developed by Godyak et al.[7] n_1 [m^{-3}] is the plasma density at the plasma-sheath boundary, where both plasma ion density n_i [m^{-3}] and time-averaged plasma electron density $<n_e>$ [m^{-3}] at the plasma-sheath boundary are equal to n_1. Distance from the surface is

Reproduced with permission of the copyright owner. Further reproduction prohibited without permission.

represented by x [m]. Ions crossing the plasma-sheath boundary at $x = s_1$ [m] are accelerated towards the electrode (or grounded wall) at $x = 0$ due to the DC component of the applied electric field. That is, the ion velocity, u_i [m/s], is increased towards the electrode. Since the ion flux $n_i u_i$ [m^{-2}-s^{-1}] is conserved and u_i increases as ions transit the sheath, n_i decreases towards the electrode. The ion particle and ion energy conservation equations are:

$$n_i u_i = n_1 u_B = (\text{const}) \tag{4.3}$$

$$u_i\left(\frac{du_i}{dx}\right)+\frac{e}{M}\left\langle\frac{dV}{dx}\right\rangle = 0 \tag{4.4}$$

Note that u_B [m/s] is the Bohm velocity, which is the initial ion velocity at the plasma-sheath boundary. M is ion mass (= 6.64×10^{-26} kg for argon ion) and $\langle dV/dx \rangle$ [V/m] is the electric field in the rf sheath averaged in time over a rf period.

s(t) [m] represents the location of the "electron sheath" edge. The electron sheath edge moves from the plasma-sheath boundary to the electrode in the rf cycle by filling the region at $s(t) < x < s_1$ with electrons. Therefore, the sheath contains only ions at $0 < x < s(t)$, and the sheath is composed of equal densities of ions and electrons at $s(t) < x < s_1$. This electron movement within the rf cycle creates the rf displacement current through the sheath, I_d [A]:

Reproduced with permission of the copyright owner. Further reproduction prohibited without permission.

$$I_d(t) = en_s\left(\frac{ds(t)}{dt}\right) \quad (4.5)$$

where n_s [m^{-3}] is the plasma electron density at $x = s$.

The instantaneous potential in the sheath can be found via Poisson's equation:

$$\frac{d^2V}{dx^2} = -\frac{e}{\varepsilon_0}n_i \qquad \text{at } 0 < x < s(t) \quad (4.6)$$

$$= 0 \qquad \text{at } s(t) < x < s_1 \quad (4.7)$$

The rf sheath current, I_{shrf} [A], is assumed to be only the displacement current from the above assumption (iii), and to be harmonic free:

$$I_{shrf} = I_d = I_0\cos(\omega t) \quad (4.8)$$

The sheath voltage is derived for a given rf sheath current. This sinusoidal rf sheath current assumption implies that all the harmonics appear in the rf sheath voltage. Since the instantaneous rf currents in both opposing electrode sheaths must be equal (current conservation), the appropriate behavior of the opposite sheath is obtained by shifting the phase of the voltage solution by 180°. Generally, a rf sheath has non-linear characteristics; in other words, the sinusoidal rf current approximation creates significant harmonics in the calculated rf sheath potential. However, the total rf potential drop between the

Reproduced with permission of the copyright owner. Further reproduction prohibited without permission.

two electrodes, which is equivalent to the sum of the two rf sheath potentials, will eliminate most of the second harmonic,[1,7] although some residual higher harmonics still exist. That is, although each sheath has non-linear characteristics, the rf voltage and current between the two electrodes has few non-linear characteristics. Therefore, the sinusoidal rf current assumption is quite reasonable.

In our experimental conditions, the dielectric window-to-plasma sheath and the plasma-to-chamber wall sheath are heavily asymmetrical. Therefore, total rf voltage across the two rf sheaths may still have significant harmonics, and the sinusoidal rf current assumption may be inadequate. In this case, the sinusoidal current assumption, which is used in our new capacitive coupling model discussed in Section 4.1.2, might create significant error in the theoretical calculation of rf sheath potential, V_{prf} [V], in an ICP system.

To solve the equations, the following boundary conditions at the plasma-sheath edge for both the potential and the electric field are used:

$$\Phi_1 = 0 \qquad \text{at } x = s_1 \tag{4.9}$$

$$E_1 = \frac{T_e}{\lambda_{D1}} \qquad \text{at } x = s_1 \tag{4.10}$$

Reproduced with permission of the copyright owner. Further reproduction prohibited without permission.

where Φ_1 [V] is the potential, E_1 [V/m] is the electric field, T_e [eV] is the electron temperature and λ_{D1} [m] is the Debye length at the plasma-sheath boundary defined as:

$$\lambda_{D1} = \sqrt{\frac{\varepsilon_0 T_e}{e n_1}} \tag{4.11}$$

Debye length is the distance scale over which significant charge densities can spontaneously exist. Low voltage sheaths are typically a few Debye lengths wide.

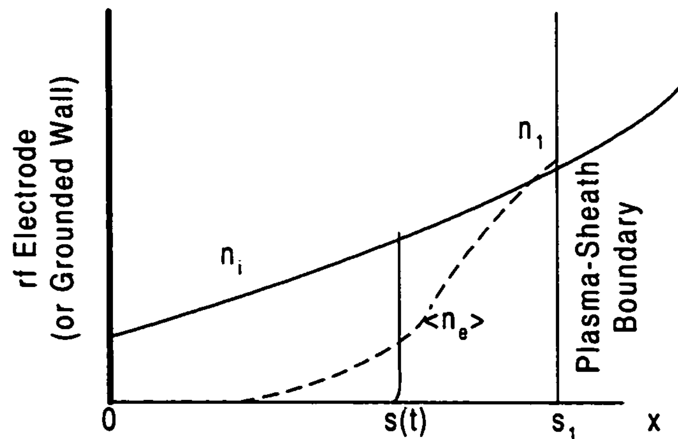

Figure 4.1 Structure of the rf sheath as modeled by Godyak et al. ni represents the spatial ion density and <ne> represents the time-averaged electron density distribution in the rf sheath. rf displacement current flows through the sheath as the "electron sheath" edge s(t) moves.

Reproduced with permission of the copyright owner. Further reproduction prohibited without permission.

In general, the capacitance between two parallel plates, neglecting any fringe field, is expressed as:

$$C = \varepsilon_r \varepsilon_0 \frac{A}{d} \tag{4.12}$$

where ε_r is the relative permittivity (the relative permittivity is assumed to be ε_r = 1), ε_o is the permittivity of free space (= 8.854 × 10^{-12} F/m), A [m^2] is the area of the parallel plates, and d [m] is the separation of the two plates. In the case of a parallel plate capacitor, ac current flows through the capacitor due to charging and discharging Q [C] on the two metallic plates. However, in the case of sheath capacitance, the sheath-plasma boundary approaches and recedes from the electrode, so the rf current flow is associated with charging and discharging Q on the electrode. Instead of moving the sheath-plasma boundary back and forth, we can apply an effective sheath width to treat the sheath as a parallel plate capacitor. The rf sheath capacitance, C_{sh} [F], may be derived from the following equation:

$$C_{sh} = \left| \frac{I_{shrf}}{\omega V_{shrf}} \right| = \varepsilon_0 \frac{A_0}{d_{sh}} \tag{4.13}$$

where V_{shrf} [V] is rf sheath potential, A_0 [m^2] is the area of electrode and d_{sh} [m] is the effective "capacitive sheath width". d_{sh} is the effective sheath width when

Reproduced with permission of the copyright owner. Further reproduction prohibited without permission.

the rf sheath is considered as a parallel plate capacitance, and is not the same as the exact sheath width. Note that d_{sh} is a strong function of the rf sheath potential as well as the plasma conditions such as plasma density and electron temperature. Therefore, we can not independently determine the sheath capacitance from the plasma conditions in order to derive the rf sheath potential, V_{shrf}. From the analytical solution by Godyak et al.,[7] a relationship between d_{sh} and V_{shrf} is derived:

$$d_{sh} = \lambda_{D1} \frac{V_{shrf}}{T_e \rho} \tag{4.14}$$

where ρ is the rf sheath oscillation parameter. ρ is found from Equation [60] in Reference 7 for $\rho < 1$, which is valid under most of our experimental conditions:

$$0.3398\rho^4 + 1.375\rho^3 + \delta\rho = \frac{V_{shrf}}{T_e} \tag{4.15}$$

where δ is the normalized sheath width with no rf current in the sheath (2.612 for argon, our feedstock gas). At several of our experimental conditions, ρ exceeds 1. In this case, a more complicated relationship shown in Equation [59] in Reference 7 should be used. Nevertheless, Eq. (4.15) is well suited for the capacitive coupling model we developed and allows us to simplify the set of simultaneous equations. The error in the calculated capacitance using

Reproduced with permission of the copyright owner. Further reproduction prohibited without permission.

Equation [60] instead of using Equation [59] is within 3 % under our experimental conditions.

4.1.2 Capacitive voltage divider circuit model

Herein, we develop the capacitive voltage divider circuit model (capacitive coupling model) to investigate the capacitive coupling from the excitation coil to the plasma in an ICP.[6] As mentioned in Chapter 1, the capacitive coupling causes the rf time variation in the plasma potential, Φ_p [V], as follows:

$$\Phi_p(t) = \Phi_{pDC} + V_{prf}\cos(\omega_{rf}t) \quad (4.16)$$

where Φ_{pDC} [V] is the DC component of the plasma potential and V_{prf} [V] is the rf plasma potential, which represents the rf time variation in Φ_p. V_{prf} is the primary interest in our capacitive coupling model.

This model is represented by three series capacitors which form a voltage divider circuit as shown in Fig. 4.2. One capacitor depicts the dielectric window, while two represent the rf sheath capacitances. The three capacitors are:

(1) The dielectric window capacitance, C_w.

(2) The dielectric window-to-bulk plasma sheath capacitance, $C_{w\text{-}p}$.

(3) The bulk plasma-to-chamber wall sheath capacitance, $C_{p\text{-}g}$.

Reproduced with permission of the copyright owner. Further reproduction prohibited without permission.

C_w and $C_{w\text{-}p}$ [F] are located in series between the metallic excitation coil and the highly conductive plasma. $C_{p\text{-}g}$ [F] is located between the plasma and the grounded metallic chamber wall.

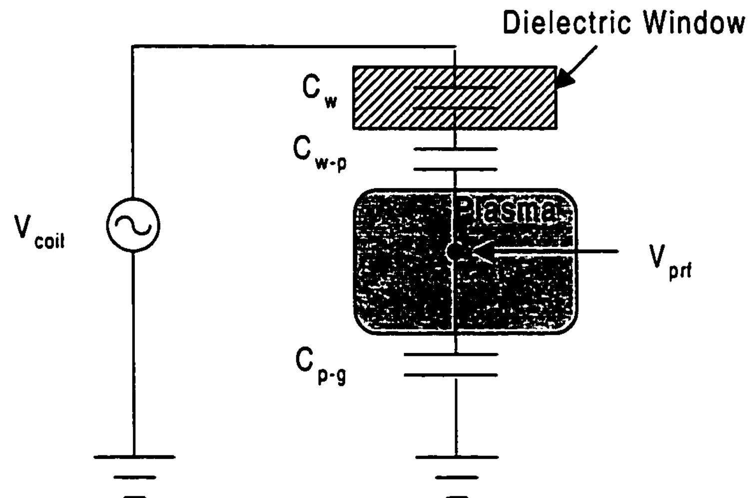

Figure 4.2 Preliminary voltage divider circuit to model capacitive coupling from the excitation coil to the plasma body, where three series capacitances, C_w, $C_{w\text{-}p}$, and $C_{p\text{-}g}$, are employed.

Reproduced with permission of the copyright owner. Further reproduction prohibited without permission.

Capacitive current flows from the excitation coil to the grounded chamber wall through these three series capacitors. If the total voltage applied to this circuit and each capacitance value are known, the voltage across each capacitor can be calculated from both Kirchoff's voltage and current equations. Actually, the rf sheath capacitance and the rf sheath potential can not be calculated independently due to the complexity of the rf sheath capacitance. That is, the rf sheath capacitance is a function of the rf sheath potential. Therefore, additional equations to describe the relationship between the rf sheath capacitance and the rf sheath potential are required. This relationship is derived from Godyak's rf sheath theory.[7]

As discussed in Section 4.1.1, Godyak's rf sheath theory provides the rf sheath thickness in a symmetrically driven rf plasma, where the two parallel plate electrodes are symmetrically placed. However, the rf sheath which we study is heavily asymmetric, which means that the dielectric window-to-bulk plasma sheath properties are quite different from the bulk plasma-to-chamber wall sheath properties. Therefore, a large amount of harmonics may exist in the rf current and voltage due to the incomplete compensation of the harmonics between the two asymmetric sheath characteristics. This may collapse the sinusoidal rf current assumption, which results in a significant error in the capacitive coupling model.

We experimentally studied the amount of the harmonics in rf sheath voltages by measuring the rf plasma potential, V_{prf}, where V_{prf} is equivalent to the

Reproduced with permission of the copyright owner. Further reproduction prohibited without permission.

voltage across the bulk plasma-to-chamber wall sheath. V_{prf} measurements are made using the capacitive probe. The measured harmonics in V_{prf} are typically less than 5 % of the fundamental component. Therefore, we applied the symmetrical rf sheaths assumption to our asymmetrical rf sheaths.

The capacitive coupling model treats the bulk plasma as an equipotential, highly conducting body, to a first approximation. We measured the actual spatial distribution of the rf plasma potential, V_{prf}, as discussed in section 4.2.1. The experimental results show that V_{prf} is quite uniform over the entire plasma region, which indicates that the equipotential plasma assumption we make is well justified.

This simple hybrid circuit model is employed in our study of the capacitive coupling. As a result of comparing the theoretical rf plasma potential to the experimental rf plasma potential measured by a capacitive probe as discussed in Section 4.2.5, we determined that our new capacitive coupling model gives quite reasonable results.

The rf capacitive voltage divider circuit model must satisfy both Kirchoff's voltage and current laws. Thus:

$$V_{coilrf} = V_{wrf} + V_{w\text{-}prf} + V_{p\text{-}grf} \tag{4.17}$$

where V_{coilrf} [V] is the excitation coil rf voltage with respect to ground, V_{wrf} [V] is the rf voltage drop across the dielectric window, $V_{w\text{-}prf}$ [V] is the voltage drop

Reproduced with permission of the copyright owner. Further reproduction prohibited without permission.

across the dielectric window-to-bulk plasma sheath, and $V_{p\text{-}grf}$ [V] is the voltage drop across the bulk plasma-to-chamber wall sheath. Furthermore, Kirchoff's current law for the capacitive circuit, in the absence of harmonic currents, requires:

$$C_w V_{wrf} = C_{w\text{-}p} V_{w\text{-}prf} = C_{p\text{-}g} V_{p\text{-}grf} \tag{4.18}$$

In contrast to simple opposing metallic plates, the ICP has a spiral coil facing a high density plasma. The dielectric window capacitance, C_w, is difficult to determine analytically due to the complicated geometry of the "spiral" excitation coil. Therefore, we instead developed a method to experimentally derive C_w as discussed in section 4.2.2. C_w is measured to be 13 pF, which agrees with crude theoretical estimates.

The rf sheath capacitance is derived from the rf sheath theory developed by Godyak et al., as introduced in section 4.1.1. In the capacitive coupling model, we use the surface area of the dielectric window A_w [m^2] to calculate $C_{w\text{-}p}$, and A_g [m^2] as the grounded chamber wall area for $C_{p\text{-}g}$. The capacitances $C_{w\text{-}p}$ and $C_{p\text{-}g}$ are given as:

$$C_{w-p} = \varepsilon_r \varepsilon_0 \frac{A_w}{d_{w-p}} \tag{4.19}$$

$$C_{p-g} = \varepsilon_r \varepsilon_0 \frac{A_g}{d_{p-g}} \tag{4.20}$$

Reproduced with permission of the copyright owner. Further reproduction prohibited without permission.

where $d_{w\text{-}p}$ and $d_{p\text{-}g}$ [m] are the "capacitive" sheath widths for the dielectric window-to-bulk plasma sheath and for the bulk plasma-to-chamber wall sheath, respectively. These are then found from Eq. (4.14) as:

$$d_{w-p} = \lambda_{D1} \frac{V_{w-prf}}{T_e \rho_{w-p}} \tag{4.21}$$

$$d_{p-g} = \lambda_{D1} \frac{V_{p-grf}}{T_e \rho_{p-g}} \tag{4.22}$$

where $\rho_{w\text{-}p}$ and $\rho_{p\text{-}g}$ are found from Eq. (4.15):

$$0.3398\rho_{w-p}^{\ 4} + 1.375\rho_{w-p}^{\ 3} + \delta\rho_{w-p} = \frac{V_{w-prf}}{T_e} \tag{4.23}$$

$$0.3398\rho_{p-g}^{\ 4} + 1.375\rho_{p-g}^{\ 3} + \delta\rho_{p-g} = \frac{V_{p-grf}}{T_e} \tag{4.24}$$

where δ is 2.612 for argon. By solving Eq. (4.17) – (4.24) simultaneously, we can obtain all rf voltage drops, rf currents and rf sheath capacitances.

There is still a major problem in the preliminary capacitive coupling model described in Fig. 4.2. In estimating the dielectric window capacitance, we set the excitation coil at one potential and measure the total capacitance of the dielectric window. However in the actual ICP case, the outside end of the coil is grounded, and rf voltage is applied to the center. The coil then has a rf potential distribution along its length from V_{coilrf} at the center to 0 V at the

Reproduced with permission of the copyright owner. Further reproduction prohibited without permission.

grounded outside terminal. To account for the rf voltage distribution along the excitation coil in the capacitive coupling model, the coil is divided into "n" parts, and each kth part has a different voltage V_{coilrf}^{k} [V] (k = 1, 2, ..., n) as shown in Fig. 4.3(a). The dielectric window capacitance C_w and the dielectric window-to-bulk plasma sheath capacitance C_{w-p} are each broken into "n" elements as well. These "n" pairs of series connected C_w^k and C_{w-p}^k [F] capacitors (k = 1, 2, ..., n) are connected in parallel to the bulk plasma.

When n = 1, the model is simply the preliminary capacitive coupling model as shown in Fig. 4.2. The rf coil voltage V_{coilrf} is applied to these three series capacitances C_w, C_{w-p}, and C_{p-g}. The rf plasma potential for n = 1, $V_{prf}(n=1)$ [V], which is equivalent to V_{p-grf}, is given by:

$$V_{prf}(n=1) = \frac{C_w C_{w-p}}{C_{w-p}C_{p-g} + C_w C_{p-g} + C_w C_{w-p}} \times V_{coilrf} \quad (4.25)$$

When n > 1, the voltage across the first branch V_{coilrf}^{1} is equal to V_{coilrf}, and across the kth branch V_{coilrf}^{k} (k = 1, 2, ..., n) is taken from the measured voltage distribution in Fig. 4.9 in Section 4.2.3. Across the nth branch V_{coilrf}^{n} is equal to 0 V, also as shown in Fig. 4.9. As seen in Fig. 4.3(b), V_{coilrf}^{k} (k = 1, 2, ..., n) is treated as "n" independent rf voltage sources. The equipotential plasma assumption allows us to treat the plasma as a highly conductive body, which

Reproduced with permission of the copyright owner. Further reproduction prohibited without permission.

neglects the plasma impedance, and "n" branches are connected at the common point in the plasma as shown in Fig. 4.3(b).

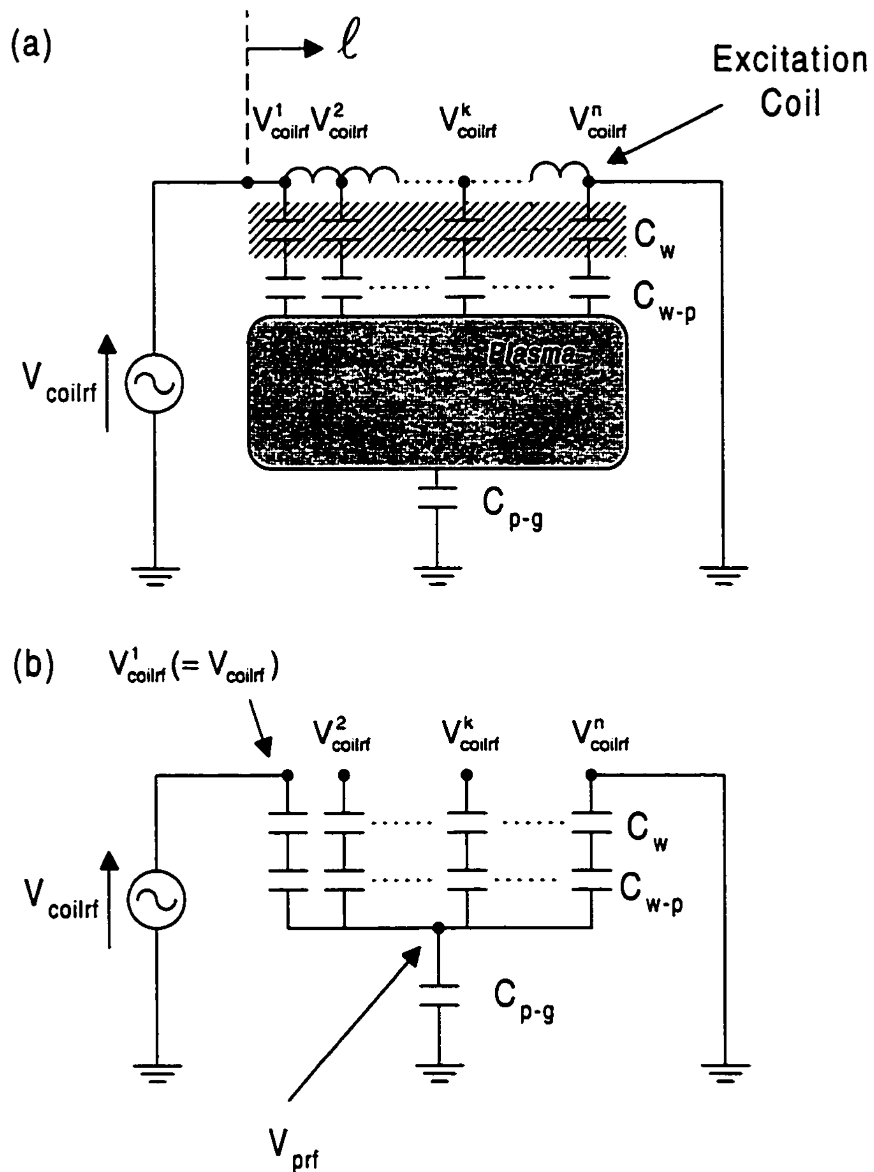

Figure 4.3 The spatially distributed capacitive coupling model: (a) basic model with the plasma fixed at an equipotential. Excitation coil, dielectric window and dielectric window-to-bulk plasma sheath capacitances are divided into "n" distributed parts, (b) Simplified circuit model used for the rf plasma potential calculation.

Reproduced with permission of the copyright owner. Further reproduction prohibited without permission.

The capacitances C_w^k and C_{w-p}^k of the kth branch are given as:

$$C_w^k = \frac{C_w}{n} \tag{4.26}$$

$$C_{w-p}^k = \varepsilon_r \varepsilon_0 \frac{A_w}{d_{w-p}^k} \frac{1}{n} \tag{4.27}$$

$$d_{w-p}^k = \lambda_{D1} \frac{V_{w-prf}^k}{T_e \rho_{w-p}^k} \tag{4.28}$$

$$0.3398 {\rho_{w-p}^k}^4 + 1.375 {\rho_{w-p}^k}^3 + \delta \rho_{w-p}^k = \frac{V_{w-prf}^k}{T_e} \tag{4.29}$$

for k = 1, 2, ... , n

Eq. (4.17) and (4.18) are also modified to satisfy both the Kirchoff voltage and current laws for all n branches:

$$V_{coilrf}^k = V_{wrf}^k + V_{w-prf}^k + V_{p-grf} \tag{4.30}$$

$$\sum_{k=1}^n C_w^k V_{wrf}^k = \sum_{k=1}^n C_{w-p}^k V_{w-prf}^k = C_{p-g} V_{p-grf} \tag{4.31}$$

for k = 1,2, ... , n

Finally, Eq. (4.20), (4.22), (4.24), (4.26) – (4.31) are solved simultaneously to find V_{prf}.

Reproduced with permission of the copyright owner. Further reproduction prohibited without permission.

Figure 4.4 shows the rf plasma potential, V_{prf}, calculated using the above theory as a function of the number of series elements "n" for a given plasma condition. One can see that the calculated V_{prf} rapidly converges with increasing "n". In this work, we use n = 5 in all theoretical calculations. The calculated V_{prf} for n = 1 is about 2.5 times as large as V_{prf} for the other "n". This is due to the invalid assumption that the rf voltage on the excitation coil is spatially constant.

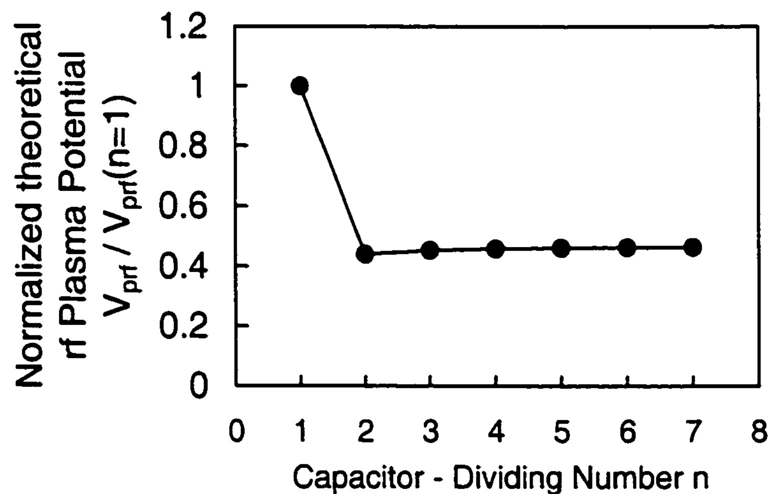

Figure 4.4 Theoretical rf plasma potential calculated using the capacitive coupling model for various integral numbers of lateral capacitors n. The calculated rf plasma potential is normalized to data for n = 1.

Reproduced with permission of the copyright owner. Further reproduction prohibited without permission.

4.1.3 Dielectric window sputtering caused by capacitive coupling

As mentioned in Chapter 1, the capacitive coupling in ICP sources causes unwanted dielectric window sputtering.[2,3,9,10] This sputtering requires frequent replacement of the expensive dielectric window and contaminates the plasma. In this section, we qualitatively describe the mechanism of the dielectric window sputtering caused by the capacitive coupling.

First of all, we study the case without rf potential on the dielectric window surface. At the initial condition when plasma is generated, the ion current incident to the dielectric window surface, I_i [A], is determined by the ion flux at the plasma-sheath boundary, Γ_i [m^{-2}-s^{-1}], as:

$$I_i = e\Gamma_i = en_1u_B \tag{4.32}$$

The electron current impinging on the dielectric window surface is much larger due to its smaller mass compared to the ion mass at pre-steady state conditions, which is before the sheath formation is completed. The dielectric window surface is negatively charged up with the surface potential, Φ_{ds} [V]. This potential difference between the plasma and the dielectric window surface, which is equivalent to the dielectric window-to-bulk plasma sheath voltage, $V_{w\text{-}p}$ [V] (= $\Phi_p - \Phi_{ds}$), repels low energy electrons, while high energy electrons ($E_e >$ $eV_{w\text{-}p}$ [eV]) can reach the dielectric window surface. Increasing $V_{w\text{-}p}$ decreases

Reproduced with permission of the copyright owner. Further reproduction prohibited without permission.

the electron current to the dielectric window surface.

$V_{w\text{-}p}$ is determined by the plasma itself to satisfy $\Gamma_i = \Gamma_e$ on the dielectric surface at the steady state, when the dielectric window surface potential becomes the floating potential ($\Phi_{ds} = \Phi_f$), so that the sheath voltage becomes $V_{w\text{-}p} = \Phi_p - \Phi_f$. The floating potential is typically a few Volts with respect to the ground in our plasma condition. As discussed in Section 2.2.1, $V_{w\text{-}p} = \Phi_p - \Phi_f = 5.2T_e$ is satisfied for Ar plasma gas. The sheath voltage accelerates the positive ions from the plasma to the dielectric window surface. The ion energy is typically 10 – 20 eV in this case. These low energy ions do not cause significant sputtering.

As discussed in section 4.1.2, the capacitive coupling creates the capacitive current pathway through the three capacitances (C_w, $C_{w\text{-}p}$ and $C_{p\text{-}g}$). Each capacitance has a voltage drop, V_{wrf}, $V_{w\text{-}prf}$ and $V_{p\text{-}grf}$, depending on the ratio of $1/C_w$, $1/C_{w\text{-}p}$ and $1/C_{p\text{-}g}$. $V_{p\text{-}grf}$ represents the rf plasma potential, V_{prf}, as discussed in section 4.1.2. The dielectric window-to-bulk plasma sheath rf voltage, $V_{w\text{-}prf}$, represents the rf potential on the dielectric window surface. V_{prf} is typically from 2 to 10 V in our plasma condition. $V_{w\text{-}prf}$ spatially varies due to the spatial distribution of the rf coil voltage. We discuss the $V_{w\text{-}prf}$ below the center of the spiral excitation coil, where high rf voltage is applied. At this location, $V_{w\text{-}prf}$ often exceeds 100 V. This condition, $V_{prf} << V_{w\text{-}prf}$, allows us to assume $V_{prf} = 0$ for simplicity. Note that in our plasma condition, electrons can respond instantaneously to the rf field variation in the sheath between the plasma and the

Reproduced with permission of the copyright owner. Further reproduction prohibited without permission.

wall surface in high density plasma due to $\omega_{pe} >> \omega_{rf}$, while ions can not due to $\omega_{pi} << \omega_{rf}$. Therefore, ions respond only to the average of DC electric field.

Suppose $V_{w\text{-}prf}$ is applied on the dielectric window surface. At the pre-steady state condition, the potential on the dielectric window surface, Φ_{ds}, is the summation of the DC floating potential, Φ_f, and the rf window surface potential, $V_{w\text{-}prf}$, as follows:

$$\Phi_{ds}(t) = \Phi_f + V_{w\text{-}prf}\cos(\omega_{rf}t) \tag{4.33}$$

Figure 4.5(a) and (b) shows the dielectric window surface potential, Φ_{ds}, and the ion and electron currents incident to the dielectric window surface, I_i and I_e [A], respectively, over a rf period. The ions respond only to the DC electric field. Therefore, I_i has a constant value. I_i is solely determined by the plasma-sheath boundary condition, which is $I_i = e\Gamma_i = en_1u_B =$ (const) regardless of the dielectric window-to-bulk plasma sheath voltage, $V_{w\text{-}p}$ (= $\Phi_p - \Phi_{ds}$). In this case, the ions are accelerated by the time averaged sheath voltage, $\langle V_{w\text{-}p} \rangle$ (= $\Phi_p - \Phi_f$). Since electrons can respond to the instantaneous electric field, the electron current, I_e, varies over a rf period. Note that the instantaneous electron current increases exponentially with decreasing sheath voltage, $V_{w\text{-}p}$, due to Maxwellian electron energy distribution. Therefore, when $V_{w\text{-}p}$ reaches its minimum, a large electron current flows onto the dielectric window surface. And this I_e is much

Reproduced with permission of the copyright owner. Further reproduction prohibited without permission.

larger than I_i due to the much smaller electron mass compared to the ion mass. The larger net electron current compared to the ion current ($I_e >> I_i$) further builds the negative potential on the dielectric window surface, which tends to reduce the electron current until the steady state condition, when $I_e = I_i$ is satisfied.

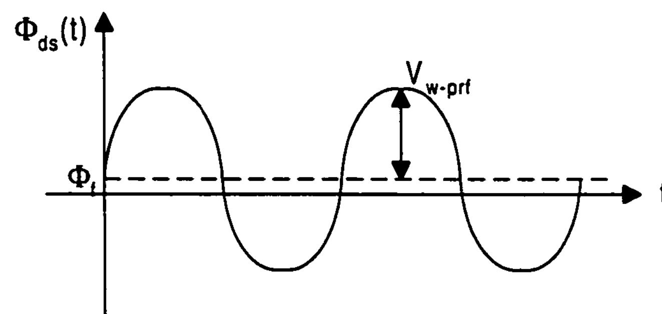

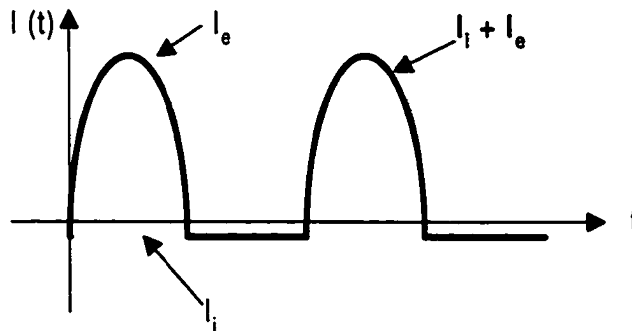

Figure 4.5 Dielectric window surface potential and current at pre-steady state conditions. (a) potential $\Phi_{ds}(t)$, (b) current I(t). Note that when Φ_{ds} is higher than the floating potential Φ_f, large amount of electron current I_e flows, while ion current I_i remains constant.

Reproduced with permission of the copyright owner. Further reproduction prohibited without permission.

At the steady state, the DC component of the dielectric window surface potential is no longer the DC floating potential, Φ_f, due to the further negative charge buildup and becomes the negative DC self bias, Φ_{self} [V], while V_{w-prf} is constant, as shown in Fig. 4.6(a). Therefore, the dielectric window surface potential, Φ_{ds}, is:

$$\Phi_{ds}(t) = \Phi_{self} + V_{w-prf}\cos(\omega_{rf}t) \tag{4.34}$$

As seen in Fig. 4.6(b), the net ion and electron currents over a rf period are the same. The ion current is approximately unchanged because the ion current is independent of the sheath voltage, V_{w-p}. The electron current is reduced to satisfy $I_e = I_i$. The exponential relationship between I_e and V_{w-p} gives a large electron current spike for the short moment when V_{w-p} is smaller than $\Phi_p - \Phi_f$. Therefore, min.(V_{w-p}) is typically close to $\Phi_p - \Phi_f$.

$$\begin{aligned} \text{min.}(V_{w-p}) &= \text{min.}\ (\Phi_p - \Phi_{ds}(t)) \\ &= \text{min.}\ (\Phi_p - (\Phi_{self} + V_{w-prf}\cos(\omega_{rf}t))). \\ &= \Phi_p - \Phi_{self} - V_{w-prf} && (4.35) \\ &\approx \Phi_p - \Phi_f && (4.36) \end{aligned}$$

therefore,

$$\Phi_{self} \approx \Phi_f - V_{w-prf} \tag{4.37}$$

Reproduced with permission of the copyright owner. Further reproduction prohibited without permission.

As $V_{w\text{-}prf}$ increases due to the increased capacitive coupling, the DC self bias, Φ_{self}, decreases and becomes negative. $V_{w\text{-}p}$ is approximately:

$$V_{w\text{-}p} = \Phi_p - \Phi_{ds}$$
$$\approx \Phi_p - \{(\Phi_f - V_{w\text{-}prf}) + V_{w\text{-}prf}\cos(\omega_{rf}t)\} \qquad (4.38)$$

Since ions can respond only to the DC component of $V_{w\text{-}p}$, the ions are accelerated to the energy E_i:

$$E_i = e\langle V_{w\text{-}p}\rangle = e(\Phi_p - \Phi_{self}) \approx e(\Phi_p - \Phi_f + V_{w\text{-}prf}) \qquad (4.39)$$

As $V_{w\text{-}prf}$ increases due to the capacitive coupling, the DC self bias, Φ_{self}, linearly becomes more negative, which results in increased ion energy, E_i [eV], impinging on the dielectric window surface. Large E_i creates significant dielectric window sputtering, since the sputter ratio monotonically increases with increasing the ion energy in our experimental conditions.[11] In order to avoid this problem, we must reduce $V_{w\text{-}prf}$ caused by capacitive coupling.

Reproduced with permission of the copyright owner. Further reproduction prohibited without permission.

(a) Dielectric window surface potential

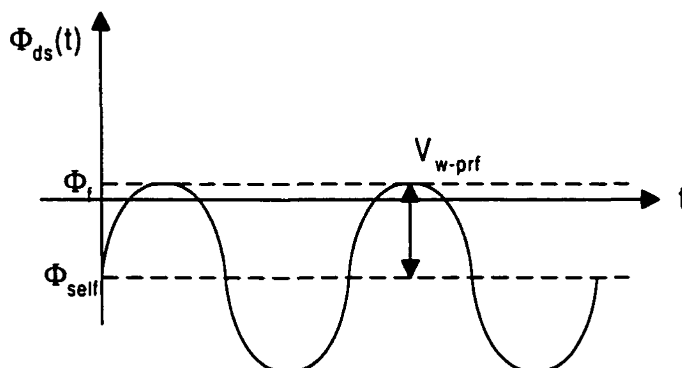

(b) Dielectric window surface current

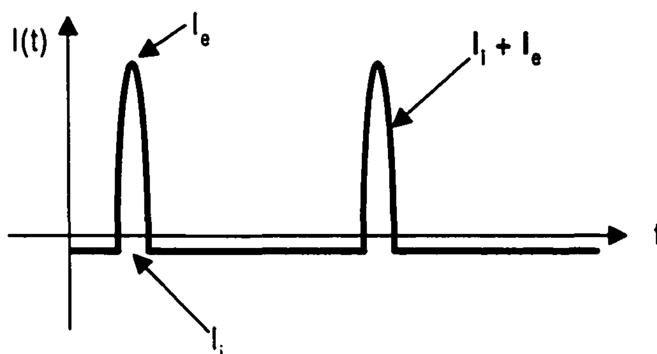

Figure 4.6 Dielectric window surface potential and current at steady state conditions. (a) potential $\Phi_{ds}(t)$, (b) current I(t). Note that the time-averaged potential $<\Phi_{ds}>$ becomes DC self bias Φ_{self}, where the time-averaged electron current $<I_e>$ is equal to I_i.

Reproduced with permission of the copyright owner. Further reproduction prohibited without permission.

4.2 Experimental Results and Discussion

4.2.1 Equipotential verification by rf plasma potential measurement

In order to simplify the capacitive coupling model, we assumed that the plasma is an equipotential body, which allows us to neglect the plasma resistance in the circuit model. The equipotential plasma body approximation is verified by measuring the spatial distributions of the rf plasma potential, V_{prf} [V].[6] Figure 4.7 shows the radial distributions of the rf plasma potential, $V_{prf}(r)$, at two distinct distances z below the dielectric window: z = 4.5 cm and z = 8 cm. One can see that in 20 mTorr argon, V_{prf} is less than 4 V while the coil voltage is very large, in the range of 1000 V, and V_{prf} is nearly uniform spatially, indicating that our equipotential bulk plasma assumption is indeed valid.

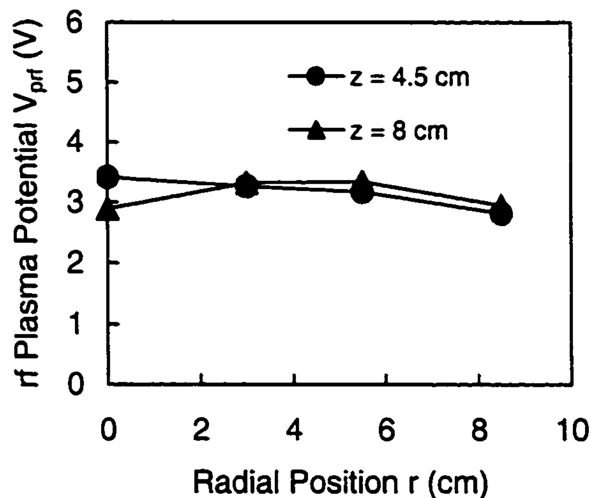

Figure 4.7 Radial spatial distribution of the measured rf plasma potential at two distances z below the dielectric window: z = 4.5 (circle) and 8 cm (triangle). The absorbed plasma power P_{abs} = 100 W, in p = 20 mTorr argon ambient. Note that the rf plasma potential is uniform at entire plasma region.

Reproduced with permission of the copyright owner. Further reproduction prohibited without permission.

4.2.2 Measurement of dielectric window capacitance

Three capacitances (C_w, C_{w-p} and C_{p-g} [F]) are employed in the capacitive coupling model. C_w is related to the dielectric window and excitation coil geometry. We experimentally measure C_w, because numerical calculation of the dielectric window capacitance C_w may cause a significant error due to the complicated geometry of the "spiral" excitation coil.[6]

An electrically grounded conducting sheet is placed under the dielectric window as shown in Fig. 4.8 to simulate the high density plasma. This forms a capacitor with the excitation coil and the grounded sheet as the two conductors, and the dielectric window as the capacitor dielectric. A known capacitor is then placed in series with the formed capacitor, and a low frequency (f ~ 100 – 1000 Hz) voltage signal is applied across the series capacitor circuit. The low frequency test signal is preferred for the measurement of the dielectric window capacitance to minimize the effect of the excitation coil inductance on the measurement, which is large at 13.56 MHz. In other words, the rf voltage may be spatially distributed along the coil at rf frequencies. The window capacitance is found from the ratio of the measured voltages across the two capacitors. The capacitance of the dielectric window, C_w is found by this means to be 13 pF.

Reproduced with permission of the copyright owner. Further reproduction prohibited without permission.

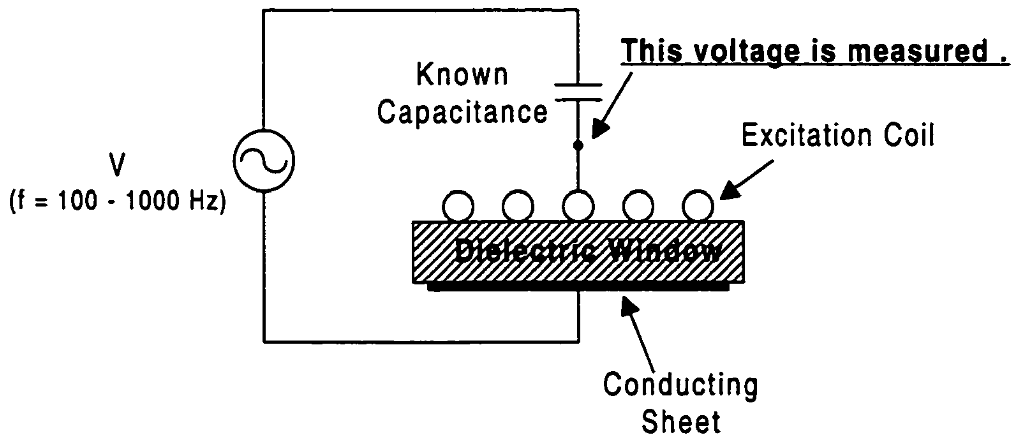

Figure 4.8 Schematic of the measurement technique of the dielectric window capacitance. The dielectric window is considered a capacitor with two electrodes (the excitation coil and the conducting sheet). The voltage measured between the two capacitances is used to calculate the dielectric window capacitance.

4.2.3 Measurement of the rf voltage distribution along excitation coil

The 13.56 MHz rf potential distribution along the excitation coil is measured using a high impedance voltage probe at various points along the coil, while an electrically grounded conducting sheet, which roughly simulates the inductively coupled plasma, is placed under the dielectric window.[6] Figure 4.9 shows the measured rf potential distribution along the excitation coil, where the horizontal axis, ℓ [m], is the linear distance from the center to the end of the coil.

The potential drop along the excitation coil is non-linear along its length, indicating that the distributed coil impedance varies with position along the coil. At the center of the coil, the magnetic flux produced by the rf current tends to

Reproduced with permission of the copyright owner. Further reproduction prohibited without permission.

cancel itself out due to the proximity of other turns, resulting in a reduced inductance. On the other hand, near the outside edge of the excitation coil, the magnetic flux does not cancel itself out as much, resulting in higher inductance locally near the outside of the coil. It is judged that this is the origin for the observed non-linear voltage drop across the coil. Even if a plasma exists under the dielectric window instead of the electrically grounded conducting sheet, the rf potential distribution still follows the relation in Fig. 4.9, because the changes in the rf coil impedance, when including the plasma impedance for various plasma conditions, is small enough to be neglected.

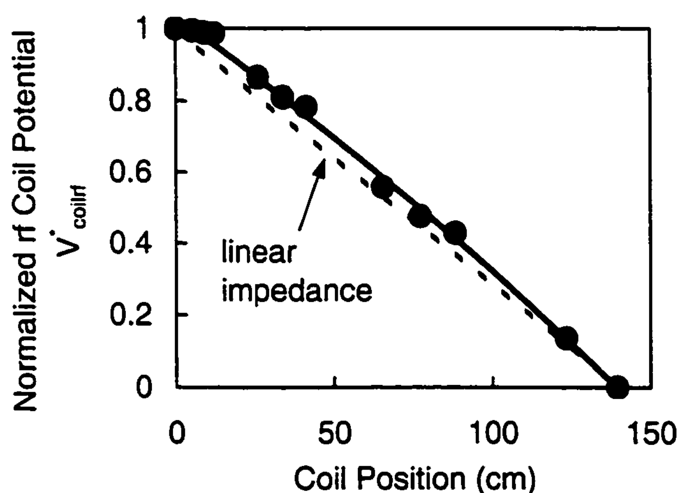

Figure 4.9 Normalized rf potential distribution measured along the excitation coil as a function of position along the coil length ℓ. The dotted line shows the linear impedance assumption along the excitation coil. The measured $V^*_{coilrf}(\ell)$ indicates non-linear impedance characteristic along the excitation coil.

Reproduced with permission of the copyright owner. Further reproduction prohibited without permission.

4.2.4 Capacitive probe and RPA methods

(a) Retarding potential analyzer (RPA)

The rf plasma potential as measured by the capacitive probe has been compared to the ion energy distribution impinging on the grounded chamber wall as an independent verification of the capacitive probe's accuracy.[6] A retarding potential analyzer (RPA) is used to measure the ion energy distribution.[12-15] The resolution of the RPA is estimated to be a few eV at our experimental conditions.[14]

The structure of the RPA is shown in Fig. 4.10. The differentially pumped RPA is separated from the main chamber by a grounded orifice 200 mm in diameter and 100 mm thick. The pressure in the RPA is typically less than 1×10^{-5} Torr. The RPA consists of two grids, the electron repeller grid and the ion energy discriminator grid, and Faraday cup ion collector. The electron repeller and ion energy discriminator grids are made of 304 stainless steel mesh (100 lines/cm, transmission T = [open area]/[total area] ~ 35 %). Dimensions of the RPA are 2.4 mm between the grounded orifice and the electron repeller grid, 9.5 mm between the electron repeller grid and the ion energy discriminator grid, and 0.8 mm between the ion energy discriminator grid and the opening in the Faraday cup ion collector. Both the electron repeller grid and the Faraday cup ion collector are negatively biased (~ - 40 V). The potential of the discriminator grid is swept from 0 to +60 V and current to the collector electrode is measured.

Reproduced with permission of the copyright owner. Further reproduction prohibited without permission.

The ion energy distribution is calculated from the derivative of the I_c - V_d plot, in standard fashion.[6]

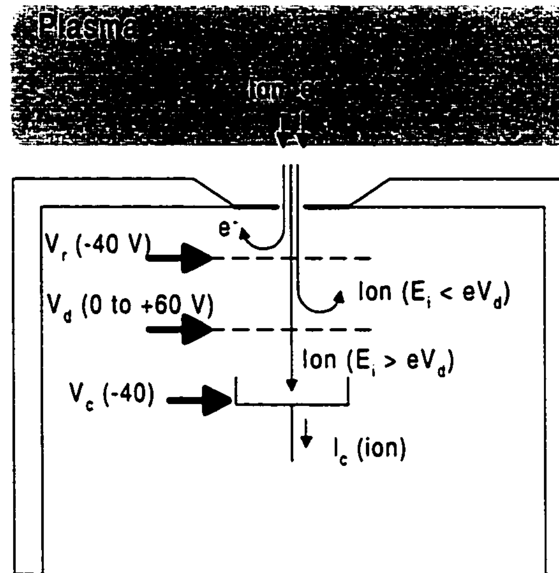

Figure 4.10 Schematic drawing of the RPA. Ions and electrons are both incident into the RPA. Electrons are repelled by V_r = -40 V. V_d is scanned from 0 to 60 V to discriminate ions, and I_c is measured to obtain I_c – V_d characteristics.

(b) Comparison of rf plasma potential

The width of the ion energy distribution (IED) impinging on a grounded wall or substrate diverges when the rf plasma potential exists.[15,16] We measure the width of IED, and calculate the rf plasma potential, V_{prf}, from the measured IED, the measured DC plasma potential, Φ_{pDC} [V], and the measured plasma parameters such as the plasma electron density at the plasma-sheath boundary

Reproduced with permission of the copyright owner. Further reproduction prohibited without permission.

n_1 [m^{-3}] and the electron temperature T_e [eV]. Accuracy of the capacitive probe is verified by comparing with V_{prf} calculated using the above method.

In the case of a collisionless sheath, an ion traversing the sheath gains an energy related to the difference between the instantaneous value of the plasma potential and the potential of the surface it impinges on. If the plasma potential has a rf component, then the ion energy distribution (IED) will have some energy spread, ΔE [eV]. This energy spread may be estimated as follows:[15,16]

$$\Delta E \approx 8V_{prf} \frac{\sqrt{2e\Phi_{pDC}/M}}{3d_{sh0}\omega_{rf}} \tag{4.40}$$

where d_{sh0} [m] is sheath width, M is the ion mass (= 6.64×10^{-26} kg for argon ion), Φ_{pDC} and V_{prf} are the DC and rf components of the plasma potential, respectively.

We use equation [61] in Reference 7 to calculate the sheath width d_{sh0}. Note that d_{sh0} is the real sheath width and different from the "capacitive" sheath width $d_{p\text{-}g}$:

$$d_{sh0} = \lambda_{D1}\left\{\delta + \rho + 2\rho^2 + \frac{5}{12}\rho^3\right\} \tag{4.41}$$

where ρ is rf sheath oscillation parameter and δ is 2.612 in argon feedstock gas. The Debye length λ_{D1} [m] is calculated from the measured n_1 and T_e. The DC

Reproduced with permission of the copyright owner. Further reproduction prohibited without permission.

plasma potential, Φ_{pDC}, in Eq. (4.40) is taken from knee of the experimental Langmuir probe I - V_B characteristic. The ion energy spread ΔE is taken from the measured ion energy distribution using the RPA placed as shown in Fig. 2.1. V_{prf} is calculated from Eq.(4.40) and (4.41).

Figure 4.11 shows a typical measured I_c - V_d plot (solid line) and the IED calculated from the first derivative, dI_c/dV_d (filled circle). The minimum energy and the maximum energy are arbitrarily defined as the energies greater than 5 % of the peak current. The energy spread ΔE is the difference between the minimum energy and maximum energy.

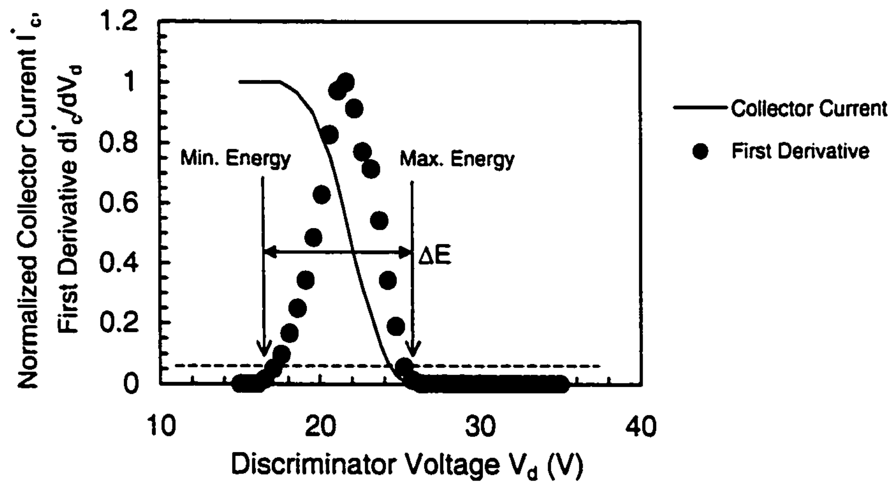

Figure 4.11 Normalized ion collector current I_c and first derivative versus discriminator voltage V_d as measured by the RPA for the ICP conditions of P_{del} = 125 W and p = 2 mTorr. ΔE is the energy spread of incident argon ions from the bulk plasma to the sheath.

Reproduced with permission of the copyright owner. Further reproduction prohibited without permission.

Figure 4.12 shows V_{prf} measured by both the capacitive probe (filled circle) and the RPA (filled triangle). One can see that these two independent results are in good agreement in spite of using two very different measurement techniques. This verifies our two measurement methods within expected errors.

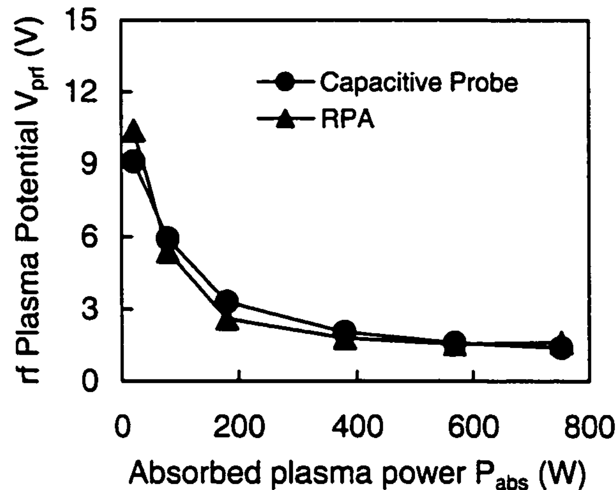

Figure 4.12 rf plasma potential as measured separately by both the capacitive probe and the RPA, in 2 mTorr argon. These two independent results are in good agreement.

4.2.5 Measured rf plasma potential results

To verify the validity of the capacitive coupling model, we measure the rf plasma potential, V_{prf}, which is equivalent to $V_{p\text{-}grf}$ [V] in the capacitive coupling model. As discussed in section 4.2.4, the accuracy of V_{prf} measured by the capacitive probe is verified with a separate method using a retarding potential analyzer.

Reproduced with permission of the copyright owner. Further reproduction prohibited without permission.

Figure 4.13(a) – (d) show the measured (circle) and theoretical (triangle) V_{prf} versus P_{abs} for four pressures in the 1 – 20 mTorr range of argon feedstock. The theoretical V_{prf} is calculated using the measured value of V_{coilrf} [V], n_e [m^{-3}], and T_e [eV] in the capacitive coupling model introduced in Section 4.1.2. Overall, the theoretical V_{prf} agrees well with the measured results. One can see that the decrease in V_{prf} with both increasing P_{abs} [W] and with increasing Ar gas pressure. These same trends occur for both the measured and the calculated V_{prf} .

Reproduced with permission of the copyright owner. Further reproduction prohibited without permission.

(a) 1 mTorr

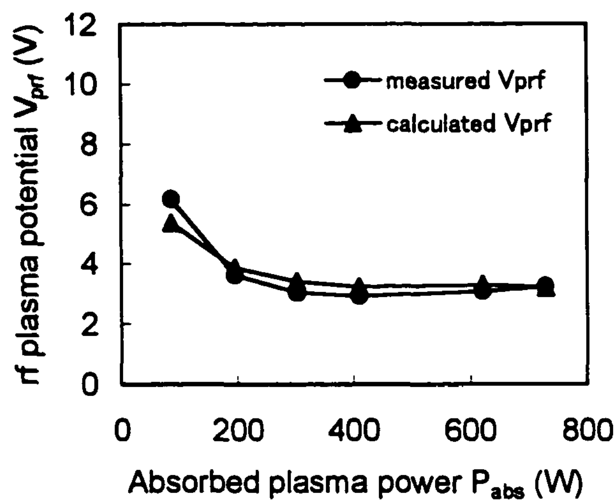

(b) 2 mTorr

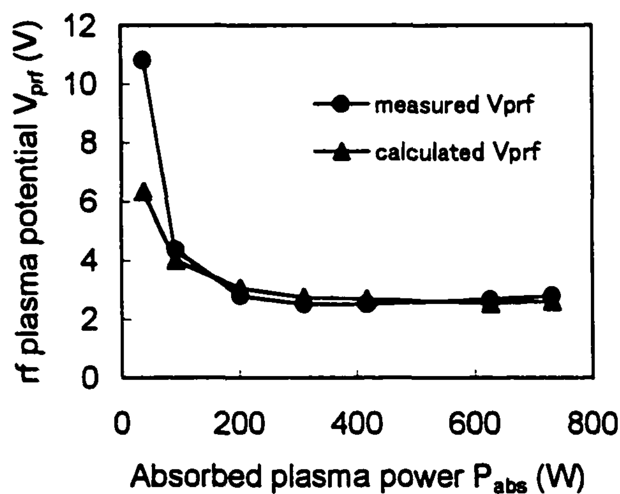

Reproduced with permission of the copyright owner. Further reproduction prohibited without permission.

(c) 5 mTorr

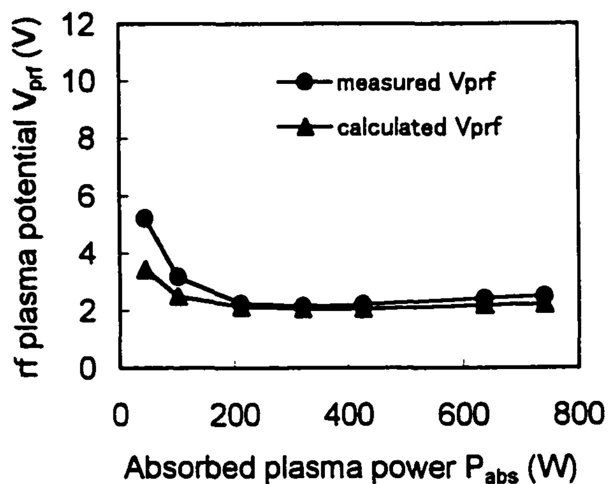

(d) 20 mTorr

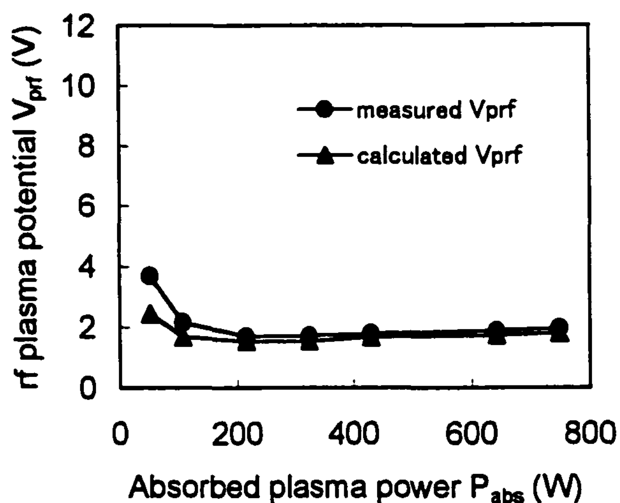

Figure 4.13 Both measured and calculated rf plasma potential as a function of P_{abs} in the argon pressures of (a) 1, (b) 2, (c) 5, and (d) 20 mTorr. The measured and calculated results are in good agreement.

Reproduced with permission of the copyright owner. Further reproduction prohibited without permission.

4.2.6 Trend of rf plasma potential

We can explain the V_{prf} – P_{abs} characteristics by using the capacitive coupling model. Here, for illustration we oversimplify the number of capacitor branches to n = 1, which leads to a wrong value of V_{prf} (~ 2.5 times larger than that with n = 5), but still maintains almost the same functional relationship between V_{prf} and P_{abs}.

For the 1.9 cm thick dielectric window, the dielectric window capacitance C_w is much less than the dielectric window-to-bulk plasma capacitance (C_{w-p}) or the bulk plasma-to-grounded wall capacitance (C_{p-g}), i.e. $C_w \ll C_{w-p}$ and $C_w \ll C_{p-g}$. Therefore V_{prf} may be approximated as:

$$V_{prf} \approx V_{coilrf} \frac{C_w}{C_{p-g}} \tag{4.42}$$

where C_w is constant (= 13 pF), so V_{prf} can be expressed as a function of V_{coilrf} and C_{p-g}. In our experimental conditions, V_{coilrf} increases from 1200 to 2800 V when the absorbed plasma power, P_{abs}, increases from 60 to 875 W at 2 mTorr argon pressure. From Eq. (4.22) and (4.24), d_{p-g} is expressed as:

$$d_{p-g} = \lambda_{D1}(0.3398\rho_{p-g}^3 + 1.375\rho_{p-g}^2 + \delta) \tag{4.43}$$

Reproduced with permission of the copyright owner. Further reproduction prohibited without permission.

$d_{p\text{-}g}$ is composed of two factors, the Debye length λ_{D1} [m] and the factor $(0.3398\rho^3 + 1.375\rho^2 + \delta)$. λ_{D1} varies from 0.194 to 0.032 mm when the absorbed plasma power increases from 60 to 875 W. On the other hand, the term $(0.3398\rho_{p\text{-}g}{}^3 + 1.375\rho_{p\text{-}g}{}^2 + \delta)$ varies only from 3.07 to 2.69. The "capacitive" sheath width $d_{p\text{-}g}$ is roughly proportional to the Debye length λ_{D1}, and therefore $C_{p\text{-}g}$ is roughly proportional to $1/\lambda_{D1}$. Therefore, V_{prf} can be simply expressed to the first order as:

$$V_{prf} \approx V_{coilrf} C_w \frac{d_{p\text{-}g}}{\varepsilon_r \varepsilon_0 A_g} \tag{4.44}$$

$$V_{prf} \propto V_{coilrf} C_w \lambda_{D1} \tag{4.45}$$

The rf plasma potential is, therefore, approximately a function of the applied rf coil voltage, V_{coilrf}, and the Debye length, λ_{D1}. λ_{D1} is solely a function of the plasma density at the plasma-sheath boundary n_1 (Eq. (4.11)). From Eq. (3.7), the plasma density is proportional to the absorbed plasma power, P_{abs}. The rf plasma potential is expressed as:

$$V_{prf} \propto V_{coilrf} \frac{C_w}{\sqrt{n_e}} \tag{4.46}$$

$$\propto V_{coilrf} \frac{C_w}{\sqrt{P_{abs}}} \tag{4.47}$$

Reproduced with permission of the copyright owner. Further reproduction prohibited without permission.

In our experimental conditions, V_{coilrf} increases only 2.3 times while $\sqrt{P_{abs}}$ changes 3.8 times, indicating that V_{prf} is more strongly influenced by P_{abs}. This is the main reason V_{prf} decreases with increasing P_{abs}.

Reproduced with permission of the copyright owner. Further reproduction prohibited without permission.

Chapter 4 References

1. M. A. Lieberman, and A. J. Lichtenberg, "Principles of Plasma Discharges and Material Processing," John Wiley and Sons, New York (1994).
2. H. Sugai, K. Nakamura, and K. Suzuki, Jpn. J. Appl. Phys. Part1, **33**, 2189 (1994).
3. M. Schaepkens, N. R. Rueger, J. J. Beulens, X. Li, T. E. F. M. Standaert, P. J. Matsuo, and G. S. Oehrlein, J. Vac. Sci. Technol. A, **17**, 3272 (1999).
4. T. Lho, N. Hershkowitz, G. H. Kim, W. Steer, and J. Miller, Plasma Sources Sci. Technol. **9**, 5 (2000).
5. K. Suzuki, K. Nakamura, H. Ohkubo, and H. Sugai, Plasma Sources Sci. Technol. **7**, 13 (1998).
6. M. Watanabe, D. M. Shaw, G. J. Collins, and H. Sugai, J. Appl. Phys. **85**, 3428 (1999).
7. V. A. Godyak, and N. Sternberg, Phys. Rev. A **42**, 2299 (1990).
8. J. Gierling, and K. U. Riemann, J. Appl. Phys. **83**, 3521 (1998).
9. Y. Hikosaka, M. Nakamura, and H. Sugai, Proc. 15th Symp. Dry Process, 97 (Tokyo, 1993).
10. Y. Horiike, Ext. Abstr. 4th Int. Symp. ULSI Science and Technology, 991 (Honolulu, 1993).
11. D. L. Smith, "Thin-Film Deposition," McGraw-Hill (1995).
12. J. R. Woodworth, M. E. Riley, P. A. Miller, G. A. Hebner, and T. W. Hamilton, J. Appl. Phys. **81**, 5950 (1997).
13. J. Mathew, R. A. Meger, R. F. Fernsler, and J. A. Gregor, Rev. Sci. Instrum. **67**, 2818 (1996).
14. B. E. Thompson, K. D. Allen, A. D. Richards, and H. H. Sawin, J. Appl. Phys. **59**, 1890 (1996).
15. J. Liu, G. L. Huppert, and H. H. Sawin, J. Appl. Phys. **68**, 3916 (1990).
16. Y. Okamoto, and H. Tamagawa, J. Phys. Soc. Jpn. **29**, 187 (1970).

Reproduced with permission of the copyright owner. Further reproduction prohibited without permission.

CHAPTER 5 COMBINED MODEL INCLUDING INDUCTIVE AND CAPACITIVE COUPLING

5.1 Combined Model

Figure 5.1 shows the air core transformer circuit model[1] (inductive coupling model) discussed in Chapter 3 combined with the new capacitive coupling circuit model,[2] which consists of three capacitors and one resistor, as discussed in Chapter 4. The series combination of the dielectric window capacitance C_w [F], the plasma resistance representing the capacitively coupled power dissipation, R_c [Ω], which is neglected in CHAPTER 4, and the two sheath capacitances C_{w-p} and C_{p-g} [F] are added in parallel to the inductive coupling model.

The two resistances R_p [Ω] (representing inductive power dissipation) and R_c (representing capacitive power dissipation) are primarily a function of plasma density n_e [m^{-3}]. Two different power transfer mechanisms cause plasma power delivery mode jumps from the capacitive-dominant mode to the inductive-dominant mode.[3] In the pre-ignition or the low plasma density region, most of the power transfer to the plasma is from capacitive coupling, and R_c dominates the power consumption. As plasma density increases by applying more delivered power, P_{del} [W], more power is dissipated inductively and R_p tends to be dominant.

Reproduced with permission of the copyright owner. Further reproduction prohibited without permission.

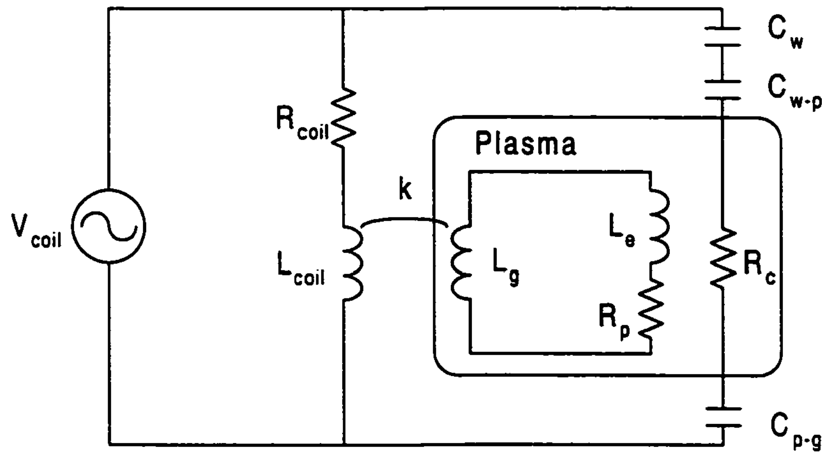

Figure 5.1 Schematic drawing of the combined inductive/capacitive coupling model. The plasma is coupled to the excitation coil both through the magnetic coupling coefficient k (inductive coupling) and through the three series capacitances (capacitive coupling).

Ideally, the inductive coupling does not influence the plasma potential. This is analogous to a standard electrical transformer, where the secondary circuit is electrically isolated from the primary circuit. Rather, the plasma potential is determined primarily by the plasma-wall surface relationship in order to satisfy the requirement that the net ion and electron currents to the wall surface must be equal. The capacitive coupling changes the plasma-wall surface relationship by adding rf current to the wall surface. In short, the main role of the capacitive coupling in the high plasma density region is not power

Reproduced with permission of the copyright owner. Further reproduction prohibited without permission.

transfer from the power supply, but to set the rf plasma potential, V_{prf} [V], and DC self bias, Φ_{self} [V], on the dielectric window.

5.2 Effect of Changing the Dielectric Window Thickness

To control both inductive and capacitive coupling from the excitation coil design point of view, one can change either the geometrical configuration of the coil or the distance between the coil and the plasma. The distance between the excitation coil and the plasma can be modified by changing the dielectric window thickness. We derive theoretically and measure experimentally the changes in electrical parameters in the ICP system such as the rf coil voltage, V_{coilrf} [V], and the rf plasma potential, V_{prf} [V], as the window thickness is changed. V_{prf} is directly influenced by the capacitive coupling, but also indirectly by the inductive coupling, because the full excitation coil-plasma interaction determines these electrical parameters. Therefore, a thorough investigation of V_{prf} by varying the dielectric window thickness helps to unravel the coupling pathways between the excitation coil and the plasma.

5.2.1 Procedure

Herein, the dielectric window thickness is changed while keeping constant ICP conditions (P_{abs} and gas pressure p). Then the corresponding change in the rf plasma potential, V_{prf}, is investigated. We assume in this analysis that in a given ICP system, at a specified P_{abs} [W] and gas pressure p

Reproduced with permission of the copyright owner. Further reproduction prohibited without permission.

[Torr], the effective plasma secondary "coil" will have the same impedance regardless of the magnetic coupling coefficient k between the excitation coil and the plasma "coil". This assumption allows us to vary only the magnetic coupling coefficient k and the dielectric window capacitance, C_w, as we vary the dielectric window thickness, d_w [m], while all the other plasma parameters such as R_p, L_g [H], L_e [H], n_e and T_e [eV] remain constant.

We apply the various dielectric window designs described in Chapter 3 to our combined model including inductive and capacitive coupling. The three dielectric window designs are:

(i) A simple 1.9 cm thick quartz window, $d_w = 1.9$.

(ii) A simple 2.2 cm thick quartz window, $d_w = 2.2$.

(iii) A hybrid 2.5 cm thick quartz and air combination window, $d_w = 2.5$.

We experimentally derive the magnetic coupling coefficient k as discussed in Chapter 3 and the dielectric window capacitance C_w in the same way discussed in section 4.2.2. Figure 5.2 shows the measured capacitance of the dielectric window, $C^*_w(d_w)$, and measured relative magnetic coupling coefficient $k_r(d_w)$ normalized to the data for $d_w = 1.9$ cm dielectric window ($k_r(1.9) = C^*_w(1.9) = 1$) for simplicity. $k_r(d_w)$ data in Fig. 5.2 is same as those in Fig. 3.7. The measured k is limited to relative values to insure simplicity of measurement. The dielectric window capacitance,$C^*_w(d_w)$, decreases with increasing thickness

Reproduced with permission of the copyright owner. Further reproduction prohibited without permission.

of the dielectric window, d_w. It decreases more rapidly from $d_w = 2.2$ to $d_w = 2.5$ than from $d_w = 1.9$ to $d_w = 2.2$. This variation occurs because the hybrid $d_w =$ 2.5 cm dielectric window includes a lower permittivity air gap layer between the two quartz plates. On the other hand, the measured k_r decreases monotonically with increasing d_w. Note that $k_r(2.2)$ is close to $C^*_w(2.2)$, while $C^*_w(2.5)$ is smaller than $k_r(2.5)$.

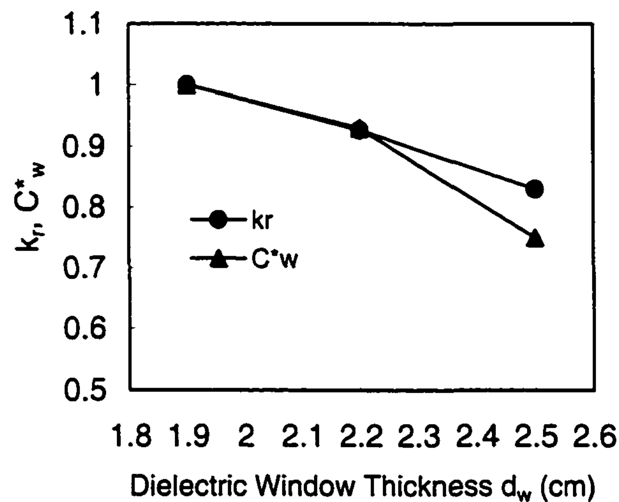

Figure 5.2 The measured relative magnetic coupling coefficient k_r and dielectric window capacitance C^*_w normalized to the data for $d_w = 1.9$ cm ($k_r(1.9) = C^*_w(1.9) = 1$). Note that $k_r(2.2)$ is close to $C^*_w(2.2)$, while $C^*_w(2.5)$ is smaller than $k_r(2.5)$.

To calculate V_{prf} using the combined model, we first vary $k_r(d_w)$ and calculate V_{coilrf} from the inductive coupling model for a given plasma condition. This iterative procedure is same technique discussed in detail in Chapter 3 to derive the theoretical R_p' and $|X_p'|$ [Ω], where experimental data of Z_{in} [Ω], V_{coilrf} and I_{coilrf} [A] for $d_w = 1.9$ and $k_r(d_w)$ data are the basis of the calculation. The

Reproduced with permission of the copyright owner. Further reproduction prohibited without permission.

calculated V_{coilrf} is used in the capacitive coupling model to derive V_{prf}, where $C_w(d_w)$ also varies with the dielectric window thickness d_w.

5.2.2 Measured and theoretical rf plasma potential

We both measure and calculate the rf plasma potential, V_{prf}, while changing the dielectric window thickness, d_w. Figure 5.3 (a) – (d) shows the theoretical V_{prf} versus P_{abs} for the three dielectric window thicknesses, d_w, in 1 – 20 mTorr of argon. From Fig. 5.3, one can see no major difference in V_{prf} between the chosen d_w = 1.9 cm and d_w = 2.2 cm dielectric window cases. $C_w(2.2)$ is smaller than $C_w(1.9)$. Therefore, one would expect to see a decrease in V_{prf}. However, increasing the dielectric window thickness reduces the inductive coupling from the excitation coil to the plasma, which results in increasing the coil voltage for a given plasma condition. Figure 5.4 (a) – (d) shows the measured V_{coilrf} for 1 – 20 mTorr of argon. One can see the increase in V_{coilrf} as d_w increases for all pressure range. The increase in V_{coilrf}, required by the reduction of the inductive coupling, offsets the decreased C_w.

V_{prf} decreases for d = 2.5 cm hybrid dielectric window case. This is because the decrease in C_w is more dominant than the increase in V_{coilrf} as d_w changes from 2.2 to 2.5. This behavior is seen over a wide pressure range from 1 to 20 mTorr.

Reproduced with permission of the copyright owner. Further reproduction prohibited without permission.

(a) 1 mTorr

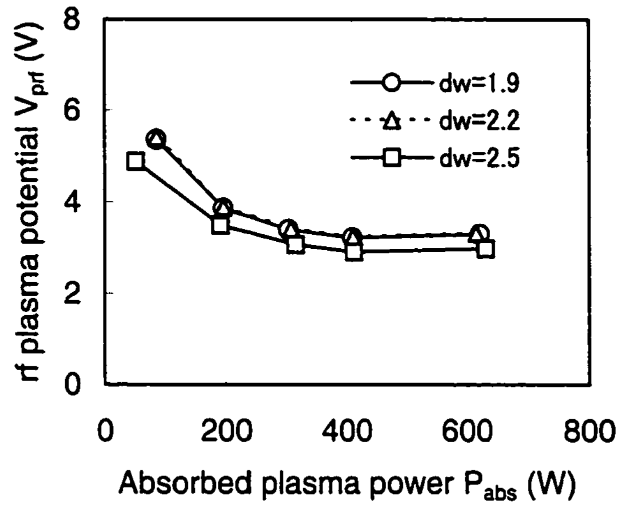

(b) 2 mTorr

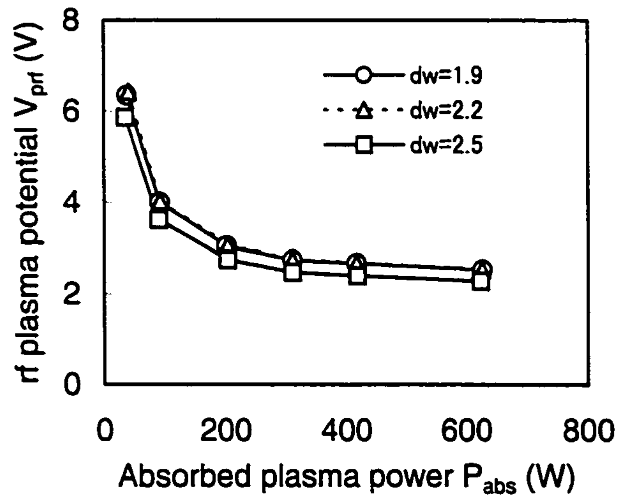

Reproduced with permission of the copyright owner. Further reproduction prohibited without permission.

(c) 5 mTorr

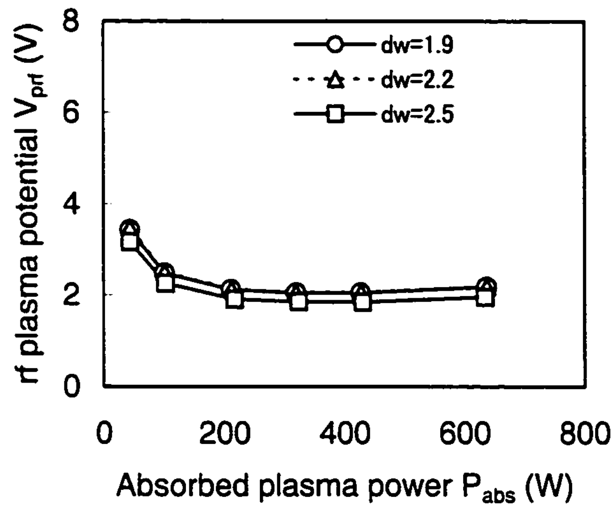

(d) 20 mTorr

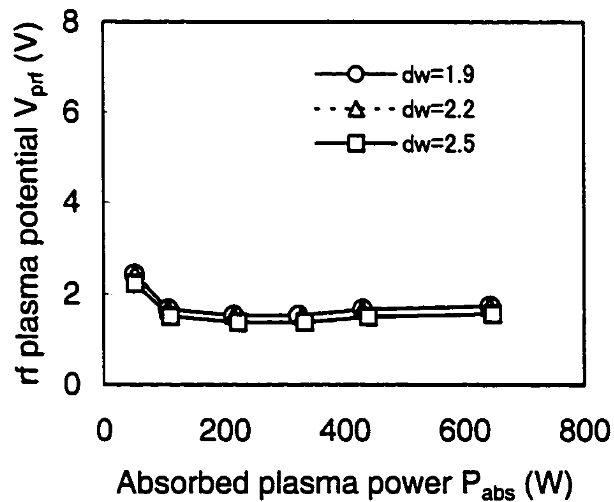

Figure 5.3 Theoretical rf plasma potential calculated using the combined inductive/capacitive coupling model for three dielectric window thicknesses d_w = 1.9, 2.2, 2.5 cm in argon pressures of : (a) 1, (b) 2, (c) 5, and (d) 20 mTorr.

Reproduced with permission of the copyright owner. Further reproduction prohibited without permission.

(a) 1 mTorr

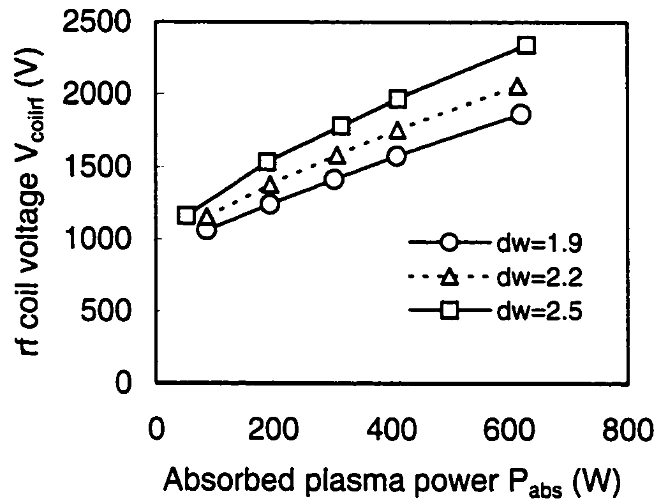

(b) 2 mTorr

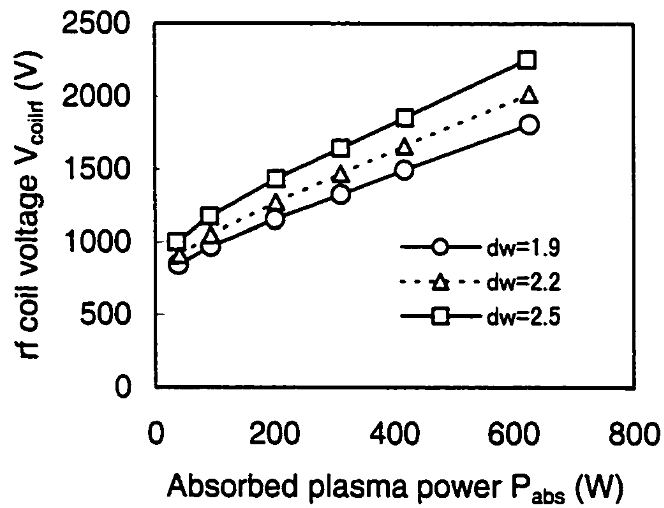

Reproduced with permission of the copyright owner. Further reproduction prohibited without permission.

(c) 5 mTorr

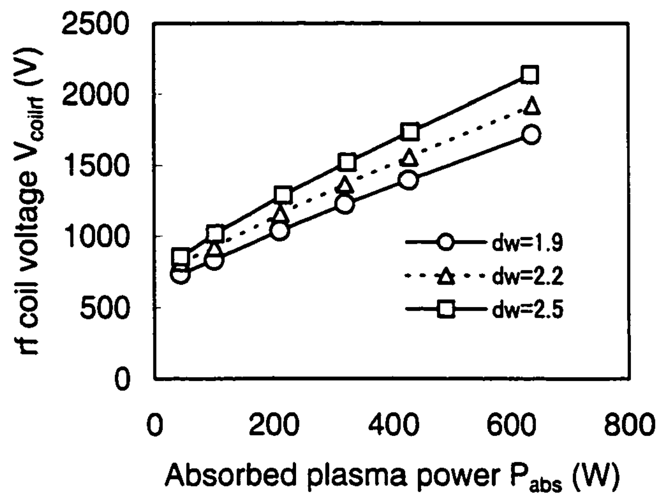

(d) 20 mTorr

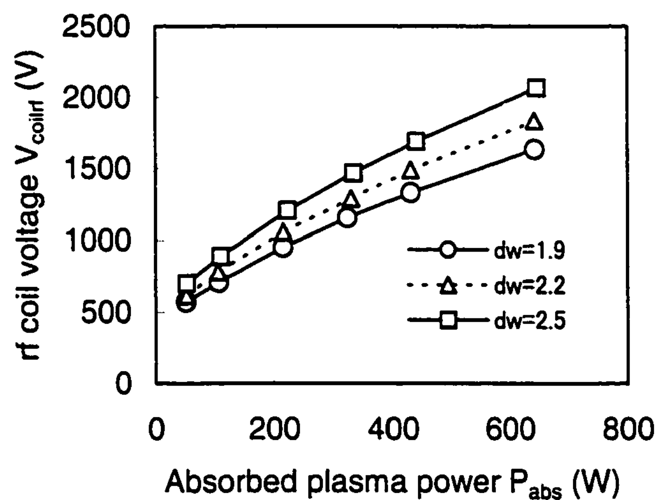

Figure 5.4 The rf coil voltage measured at the excitation coil input for three dielectric window thicknesses d_w = 1.9, 2.2, 2.5 cm in argon pressures of : (a) 1, (b) 2, (c) 5, and (d) 20 mTorr. Note that V_{coilrf} increases as d_w increases.

Reproduced with permission of the copyright owner. Further reproduction prohibited without permission.

Figure 5.5 (a) – (d) shows the measured V_{prf} versus P_{abs} for various dielectric window thicknesses, d_w, for 1 – 20 mTorr of argon. The measured V_{prf} follows the same tendency as the theoretical V_{prf}, especially in the low pressure range. That is, $V_{prf}(1.9)$ is close to $V_{prf}(2.2)$, and $V_{prf}(2.5)$ is about 20 % smaller than those two. Therefore, the new combined inductive/capacitive model explains very well the trend in rf plasma potential caused by whole excitation coil-plasma interaction through both inductive and capacitive coupling pathways. Although a good agreement is achieved in the theoretical and measured V_{prf}, there is some difference in the high pressure range. This is possibly due to the spatial gradient in the plasma density which the capacitive coupling model does not fully take into account. The plasma density at the plasma-sheath boundary strongly influences the sheath capacitance. The non-uniformity in the plasma density is more significant in high pressure.

Reproduced with permission of the copyright owner. Further reproduction prohibited without permission.

(a) 1 mTorr

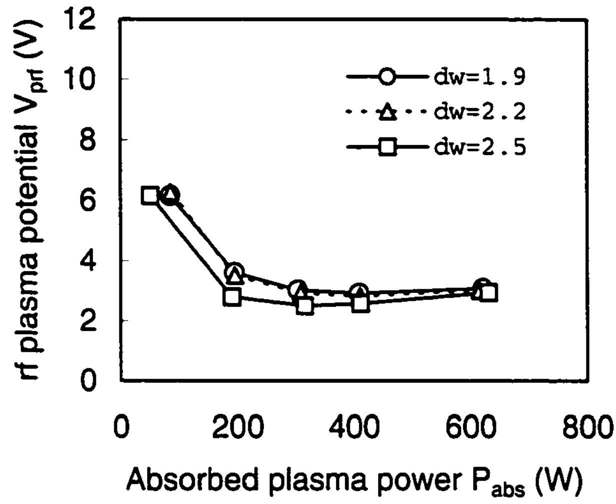

(b) 2 mTorr

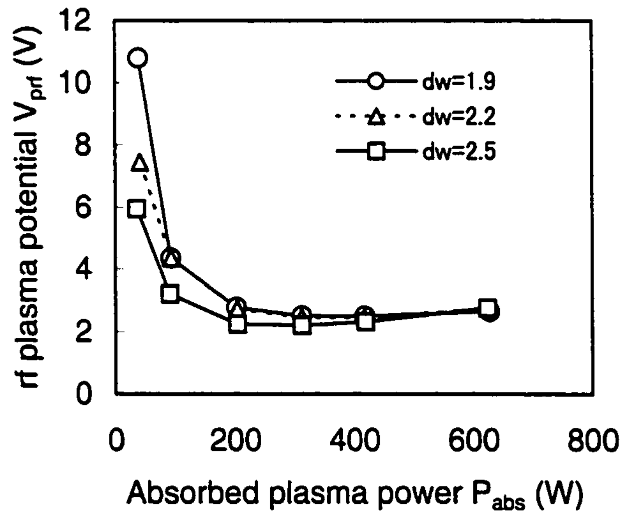

Reproduced with permission of the copyright owner. Further reproduction prohibited without permission.

(c) 5 mTorr

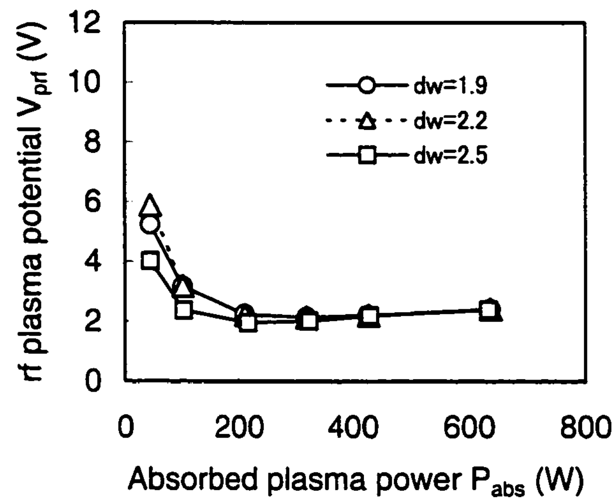

(d) 20 mTorr

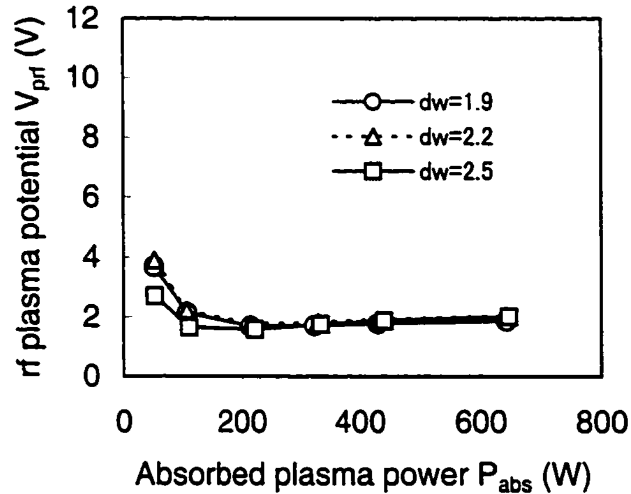

Figure 5.5 The measured rf plasma potential for three dielectric window thicknesses d_w = 1.9, 2.2, 2.5 cm in argon pressures of : (a) 1, (b) 2, (c) 5, and (d) 20 mTorr. Note that the data for d_w = 1.9 and 2.2 cm are close together, while the data for d_w = 2.5 cm is distinguishably smaller.

Reproduced with permission of the copyright owner. Further reproduction prohibited without permission.

5.2.3 Discussion

The effect of both inductive and capacitive coupling pathways on the rf plasma potential, V_{prf}, is both theoretically and experimentally derived in Section 5.2.2. Below, we simplify the combined model for the rf plasma potential calculation and obtain the fundamental relationship in coupling parameters which determine the rf plasma potential. This simplified relationship helps us to optimize the rf plasma potential from the excitation coil design point of view.

From the capacitive coupling model, the rf plasma potential, V_{prf}, is a function of the coil voltage V_{coilrf}, the dielectric window capacitance C_w, and absorbed plasma power P_{abs} as seen in Eq. (4.47), where $V_{prf} \propto V_{coilrf} C_w / \sqrt{P_{abs}}$.

V_{coilrf} is primarily determined by the inductive coupling. From Eq. (3.9), R_p' is proportional to k^2. Therefore, $R_p'(2.2) = k_r(2.2)^2 \times R_p'(1.9)$ and $R_p'(2.5) = k_r(2.5)^2 \times R_p'(1.9)$. The rf coil current for d_w = 2.2 and 2.5, $I_{coilrf}(d_w)$, is derived from the following equation:

$$I_{coilrf}(d_w) = \sqrt{\frac{P_{abs}}{R_p'(d_w)}} \tag{5.1}$$

$$\propto \sqrt{\frac{P_{abs}}{k_r(d_w)^2 R_p'(1.9)}}$$

$$\propto \frac{1}{k_r(d_w)} \sqrt{\frac{P_{abs}}{R_p'(1.9)}} \tag{5.2}$$

Reproduced with permission of the copyright owner. Further reproduction prohibited without permission.

For a constant total input impedance of the circuit, Z_{in} (= Z_{coil} + Z_p'), V_{coilrf} is proportional to I_{coilrf} as well from the following equation:

$$V_{coilrf}(d_w) = |Z_{in}| \cdot I_{coilrf}(d_w) \tag{5.3}$$

$$\propto \frac{|Z_{in}|}{k_r(d_w)}\sqrt{\frac{P_{abs}}{R_p'(1.9)}} \tag{5.4}$$

Applying Eq. (5.4) into Eq. (4.47), the rf plasma potential is:

$$V_{prf}(d_w) \propto \left(\frac{|Z_{in}|}{k_r(d_w)}\sqrt{\frac{P_{abs}}{R_p'(1.9)}}\right)\frac{C_w(d_w)}{\sqrt{P_{abs}}} \tag{5.5}$$

$$\propto \frac{|Z_{in}|C_w(d_w)}{k_r(d_w)\sqrt{R_p'(1.9)}} \tag{5.6}$$

Experimentally, Z_{coil} might change slightly with changing d_w due to the change in the parasitic inductive coupling between the excitation coil and the vacuum chamber, and Z_p' changes with varying k and plasma conditions as shown in Eq. (3.9) and (3.10). However, the change in Z_{in} with changing the plasma conditions and dielectric window thickness as measured by the rf plasma impedance monitor is less than 5 % in our experiment. Therefore, V_{prf} is approximated as:

Reproduced with permission of the copyright owner. Further reproduction prohibited without permission.

$$V_{prf}(d_w) \propto \frac{C_w(d_w)}{k_r(d_w)\sqrt{R_p'(1.9)}} \qquad (5.7)$$

P_{abs} is eliminated in Eq.(5.7), and V_{prf} is simply described by $C_w(d_w)$, $k_r(d_w)$ and $R_p'(1.9)$ using the combined inductive and capacitive coupling model.

As discussed in Section 5.2.2, $V_{prf}(2.2)$ is close to $V_{prf}(1.9)$. This is because $C_w(2.2) / k_r(2.2) = 13.34$ is close to $C_w(1.9) / k_r(1.9) = 13.30$ in Eq. (5.7), while $C_w(2.5) / k_r(2.5) = 12.02$ is smaller than these two cases. In order to reduce the rf plasma potential, we can either decrease the dielectric window capacitance, C_w, or increase the magnetic coupling coefficient k for a fixed plasma condition.

Thus, this new combined model increases understanding of the interaction between the excitation coil and the plasma through both inductive and capacitive coupling. This model helps engineers to design the excitation coil from coupling point of view and optimize electrical parameters such as rf plasma potential and power transfer efficiency.

Reproduced with permission of the copyright owner. Further reproduction prohibited without permission.

Chapter 5 References

1. R. B. Piejak, V. A. Godyak, and B. M. Alexandrovich, Plasma Sources Sci. Technol. **1**, 179 (1992).
2. M. Watanabe, D. M. Shaw, G. J. Collins, and H. Sugai, J. Appl. Phys. **85**, 3428 (1999).
3. K. Suzuki, K. Nakamura, H. Ohkubo, and H. Sugai, Plasma Sources Sci. Technol. **7**, 13 (1998).
4. M. A. Lieberman, and A. J. Lichtenberg, "Principles of Plasma Discharges and Material Processing," John Wiley and Sons, New York (1994).

Reproduced with permission of the copyright owner. Further reproduction prohibited without permission.

CHAPTER 6 SUMMARY AND FUTURE WORK

Both inductive and capacitive coupling pathways in an ICP system are studied in this dissertation to better elucidate the excitation coil-plasma interaction.

The inductive coupling model has been developed previously by Piejak et al. This model is useful to explain the inductive power transfer mechanism from the excitation coil to the plasma. However, the validity of the model has been unclear due to non-linear plasma impedance and parasitic effects such as parasitic capacitive coupling. From the inductive coupling model, the plasma impedance transferred to the primary circuit, Z_p' [Ω], should be proportional to k^2 for a given plasma condition. We experimentally verified this relationship between the measured Z_p' and k. Since it is difficult to obtain the absolute value of k, we developed a new method to obtain the relative change in k from local magnetic flux measurements in the plasma chamber area. Measured values of Z_p' and k agreed with values obtained from the inductive coupling model developed by Piejak et al.

Parasitic capacitive coupling from the high voltage excitation coil to the plasma causes process problems such as the dielectric window sputtering. We developed a capacitive coupling model in order to better understand these

Reproduced with permission of the copyright owner. Further reproduction prohibited without permission.

problems. The capacitive current pathway is represented by three capacitances, the dielectric window capacitance, the dielectric window-to-bulk plasma sheath capacitance and the bulk plasma-to-chamber wall sheath capacitance. We employed the rf sheath theory developed by Godyak et al. for the calculation of the sheath capacitance. The measured plasma electron density n_e [m^{-3}] and electron temperature T_e [eV] were used in the capacitive coupling model to calculate the rf plasma potential, V_{prf} [V]. V_{prf} was measured using a capacitive probe in order to compare with the theoretical data. The accuracy of the capacitive probe was independently verified by the comparison with V_{prf} measured by the ion energy distribution (IED) impinging on the ground wall surface. The theoretical V_{prf} derived from the capacitive coupling model agrees well with the measured V_{prf}, which proves the effectiveness of the capacitive coupling model.

Finally, we developed a combined model of inductive and capacitive coupling to understand the complete coupling pathways from the excitation coil to the plasma. The rf plasma potential is not only directly influenced by the capacitive coupling, but also indirectly influenced by the inductive coupling. We varied the thickness of the dielectric window in order to change both inductive and capacitive coupling from the excitation coil to the plasma and measured V_{prf}. The combined model well explains the relationship between the measured V_{prf} and the dielectric window thickness. The combined model is useful to optimize

Reproduced with permission of the copyright owner. Further reproduction prohibited without permission.

the electrical parameters in the ICP system in terms of the excitation coil-plasma interaction.

One of the suggestions for future work is to measure the sputter rate of the dielectric window and relate the sputter rate with the capacitive coupling by applying the coupling model developed herein. Furthermore, we can better design the dielectric window and excitation coil configuration to reduce the dielectric window sputtering. Our model should be compared to data of the dielectric window sputtering experiment.

Another suggestion is to study the relationship between the rf plasma potential and the dielectric window erosion in etch gas chemistries. Fluorocarbon-based gas is typically used for silicon dioxide etching. In general, the dielectric window is made of quartz, which is a crystalline silicon dioxide or alumina (Al_2O_3) ceramic. Therefore, the radicals, which are intended to etch the silicon dioxide film, also etch the dielectric window more rapidly. If there is a large DC self bias on the dielectric window surface, high energy ions as well as the radicals impinge on it, which enhances the etching of the window material. The contribution of the dielectric window erosion will be greater by the chemical etching process than the physical sputtering process. We can use our capacitive/inductive coupling model to find the solution for the minimization of dielectric window erosion.

Reproduced with permission of the copyright owner. Further reproduction prohibited without permission.

Appendix

Symbols and Physical Constants in the Dissertation

a_p radius of torroidal plasma current path [m].
a_t radius of cylindrical Langmuir probe tip [m].
A area of the two plates for parallel plate capacitance [m^2].
A_0 electrode area [m^2].
A_g surface area of grounded chamber wall [m^2].
A_{pl} area of particle loss [m^2].
A_{sh} plasma-sheath boundary area for cylindrical Langmuir probe tip [m^2].
A_w surface area of dielectric window [m^2].
B magnetic flux density [Wb/m^2].
$\dot{B}$ time varying magnetic flux density, dB/dt.
B_z magnetic flux density normal to plasma coil plane [Wb/m^2].
$\dot{B}_z$ time varying magnetic flux density, dB_z/dt.
c_1 coil to which rf current is applied.
c_2 coil to which magnetic flux is coupled.
C capacitance between two parallel plates [F].
C_{cp} total of three series capacitance of capacitive probe (4 pF).
$C_{p\text{-}g}$ bulk plasma-to-chamber wall sheath capacitance [F].
C_{sh} rf sheath capacitance [F].
C_w dielectric window capacitance [F].
C^{*}_{w} normalized dielectric window capacitance.
C^k_w dielectric window capacitance for k[th] branch [F].
$C_{w\text{-}p}$ dielectric window-to-bulk plasma sheath capacitance [F].
C^k_{w-p} dielectric window-to-bulk plasma sheath capacitance for k[th] branch [F].
d separation of the two plates for parallel plate capacitance [m].
$d_{p\text{-}g}$ capacitive sheath width for bulk plasma-to-chamber wall sheath [m].
d_{sh} effective capacitive sheath width [m].
d_{sh0} sheath width [m].
d_t length of cylindrical Langmuir probe tip [m].
d_w dielectric window thickness [m].
$d_{w\text{-}p}$ capacitive sheath width for dielectric window-to-bulk plasma sheath [m].

Reproduced with permission of the copyright owner. Further reproduction prohibited without permission.

d^k_{w-p} capacitive sheath width for dielectric window-to-bulk plasma sheath for k^{th} branch [m].
e electron charge (1.6022×10^{-19} C).
E_1 electric field at plasma-sheath boundaty [V/m].
E_e electron energy [eV].
E_i ion energy [eV].
E_T total energy loss per ion [eV].
ΔE energy spread in ion energy distribution [eV].
f_{rf} driving frequency (13.56 MHz).
I Langmuir probe current [A].
I_0 magnitude of rf displacement current through sheath [A].
I_1 current applied to c_1 [A].
I_c collector current [A].
I_{coilrf} rf current through excitation coil [A].
I_d rf displacement current through sheath [A].
I_e electron current incident to dielectric window surface [A].
I_{esat} electron saturation current for Langmuir probe $I - V_B$ characteristic [A].
I_i ion current incident to dielectric window surface [A].
I_{isat} ion saturation current for Langmuir probe $I - V_B$ characteristic [A].
I_{sat} saturation current for Langmuir probe $I - V_B$ characteristic [A].
I_{shrf} rf sheath current [A].
J_{sat} saturation current density for Langmuir probe $I - V_B$ characteristic [A/m^2].
k magnetic coupling coefficient.
k_r relative magnetic coupling coefficient normalized to the magnetic coupling coefficient for $d_w = 1.9$ cm.
ℓ linear distance from the center to the end of excitation coil [m].
L_1 self inductance of c_1 [H].
L_2 self inductance of c_2 [H].
L_{coil} excitation coil inductance [H].
L_e electron inertia inductance [H].
L_g geometric inductance of ICP current path [H].
m electron mass (9.11×10^{-31} kg).
M ion mass (6.64×10^{-26} kg for argon ion).
M_{12} mutual inductance between c_1 and c_2 [H].
n_1 ion or electron density at plasma-sheath boundary [m^{-3}].
n_e plasma electron density [m^{-3}].
n_i plasma ion density [m^{-3}].
n_s plasma electron density at $x = s$ [m^{-3}].
p argon gas pressure [Torr].
P_{abs} absorbed plasma power [W].
P_{coil} power loss in excitation coil [W].
P_{del} rf power delivered to excitation coil [W].
P_{gen} power generated at rf power supply [W].

Reproduced with permission of the copyright owner. Further reproduction prohibited without permission.

P_{mn} power loss in matching network [W].
Q electric charge [C].
r radial position [m].
r_p ring radius of torroidal plasma current path [m].
R_c plasma resistance for capacitive power dissipation [Ω].
R_{coil} excitation coil resistance [Ω].
R_{in} real part of the total rf input impedance of excitation coil including ICP circuit [Ω].
R_p plasma resistance [Ω].
R_p' plasma resistance referred to the primary side of air core transformer [Ω].
R_{tm} termination impedance of oscilloscope [Ω].
s location of electron sheath edge [m].
s_1 location of plasma-sheath boundary [m].
T transmission of electron repeller and ion energy discriminator grids for RPA (~ 35 %).
T_e electron temperature [eV].
u_B Bohm velocity [m/s].
u_i ion velocity [m/s].
V potential in sheath [V].
V_B probe voltage [V].
V_{coilrf} rf voltage at excitation coil input [V].
V^*_{coilrf} normalized rf potential distribution on the excitation coil [V].
V^k_{coilrf} rf voltage at excitation coil input for the kth branch [V].
V_{cprf} rf voltage on capacitive probe [V].
V_d discriminator voltage [V].
V_{mrf} rf potential induced around the loop of B-dot probe [V].
V_{prf} rf plasma potential [V].
$V_{p\text{-}grf}$ rf voltage drop across bulk plasma-to-chamber wall sheath [V].
V_r repeller voltage [V].
V_{shrf} rf sheath potential [V].
V_{wrf} rf voltage drop across dielectric window [V].
$V_{w\text{-}p}$ instantaneous voltage drop across dielectric window-to-bulk plasma sheath [V].
$V_{w\text{-}prf}$ rf voltage drop across dielectric window-to-bulk plasma sheath [V].
x distance from rf electrode (or grounded wall) [m].
X_{coil} rf coil reactance [Ω].
X_{in} imaginary part of the total rf input impedance of excitation coil including ICP circuit [Ω].
X_p plasma reactance [Ω].
X_p' plasma reactance referred to the primary side of air core transformer [Ω].
z z-position from the dielectric window surface [m].

Reproduced with permission of the copyright owner. Further reproduction prohibited without permission.

Z_{coil} rf coil impedance [Ω].
Z_{in} total rf input impedance of excitation coil including ICP circuit [Ω].
Z_p plasma impedance [Ω].
α rf plasma potential-capacitive probe voltage conversion factor (1.26×10^{-3}).
δ normalized sheath width with no rf current in sheath (2.612 for argon).
ε_0 permittivity of free space (8.854×10^{-12} F/m).
ε_r relative permittivity.
Γ_e electron flux at plasma-sheath boundary [m^{-2}-s^{-1}].
Γ_i ion flux at plasma-sheath boundary [m^{-2}-s^{-1}].
λ_D Debye length [m].
λ_{D1} Debye length at plasma-sheath boundary [m].
μ_0 permeability of free space ($4\pi \times 10^{-7}$ H/m).
μ_r relative permeability.
ν_e effective momentum transfer collision frequency between electrons and atoms [Hz].
ν_m momentum transfer collision frequency between electrons and atoms [Hz].
ρ rf sheath oscillation parameter.
$\rho_{p\text{-}g}$ rf sheath oscillation parameter for bulk plasma-to-chamber wall sheath capacitance.
$\rho_{w\text{-}p}$ rf sheath oscillation parameter for dielectric window-to-bulk plasma sheath capacitance.
ρ^k_{w-p} rf sheath oscillation parameter for k^{th} branch of dielectric window-to-bulk plasma sheath capacitance.
σ_p complex plasma conductivity [Ω^{-1}-m^{-1}].
ϕ_2 magnetic flux which transverses c_2 [Wb].
ϕ_{loop} magnetic flux through B-dot probe tip [Wb].
ϕ_p rf magnetic flux induced by rf current applied to excitation coil [Wb].
Φ_1 potential at plasma-sheath boundary [V].
Φ_{ds} instantaneous dielectric window surface potential [V].
Φ_f floating potential [V].
Φ_p instantaneous plasma potential [V].
Φ_{pDC} DC plasma potential [V].
Φ_{self} DC self bias [V].
ω_{pe} plasma electron frequency [rad/s].
ω_{pi} plasma ion frequency [rad/s].
ω_{rf} radian driving frequency [rad/s].

Reproduced with permission of the copyright owner. Further reproduction prohibited without permission.